6-7-2018

Nano-Materials Based Analytical Applications in Biomarker Discovery and Thin Film Sensors

Gayatri Phadke
University of Connecticut - Storrs, gayatri.phadke@uconn.edu

Nano-Materials Based Analytical Applications in Biomarker Discovery and Thin Film Sensors

Gayatri Sunil Phadke, PhD
University of Connecticut, [2018]

Nanoparticle enabled technology continues to attract heavy research interest and is increasingly used in many industries, including drug and medical device design. The research presented here focuses on applications of nano-materials in biomarker discovery and thin film sensors. In the first part, L-selectin (CD62L) protein is evaluated in bladder cancer patients as a possible biomarker for diagnosis and staging of the disease. The latter part employs inkjet printed nano-materials as QR codes for anti-counterfeiting applications. Additionally, an electrochemical sensor and a multi-well catalysis reactor are proposed, both incorporating inkjet printed nano-materials.

Bladder cancer, while predominantly diagnosed at an early stage, has < 6% five-year survival rate when metastasized. Current FDA approved biomarker tests alone are unreliable for diagnosis. L-selectin, previously implicated as a biomarker, is quantified in human serum of bladder cancer patients, using semi-automated in-house microfluidic system with a bead-based electrochemical immunoassay. Calibration and good recovery is established for the immunoarray. Comparison to ELISA test reveals systemic errors in ELISA at low and high concentrations of the protein. Correlation of CD62L concentration in serum of cancer-free controls and bladder cancer patient with varying stages of the disease yields preliminary positive correlation. All cancer patients have high soluble CD62L concentration compared to healthy

cancer-free controls. Additionally, both ELISA and the new immunoarray can successfully differentiate low-grade and high-grade bladder cancer tumors.

In the latter half of this thesis, zinc oxide nanoparticles are inkjet printed as a Quick Response code (QR code) on aluminum-coated integrated circuits. These optical phase tags provide improved anti-counterfeiting measures by adding a unique optical signature as an additional detection method. Compared to conventional barcodes and QR codes, zinc oxide material can be characterized with polarimetry and speckle pattern for analysis of material composition and surface roughness. These analytical tests are able to differentiate true and false class optical phase tags, even when minor non-compliance with the fabrication method is observed. Zinc oxide is doped with copper and nickel ions and 2D and 3D quilt patterns of these QR codes are also inkjet printed for heightened security features.

Nano-Materials Based Analytical Applications in Biomarker Discovery and Thin Film Sensors

Gayatri Sunil Phadke

B.Sc., St. Xavier's College, Mumbai, **[2009]**

M.Sc., King's College London, **[2010]**

A Dissertation

Submitted in Partial Fulfillment of the

Requirements for the Degree of

Doctor of Philosophy

at the

University of Connecticut

2018

APPROVAL PAGE

Doctor of Philosophy Dissertation

Nano-Materials Based Analytical Applications in Biomarker Discovery and Thin Film Sensors

Presented by

Gayatri Sunil Phadke, B.Sc., M.Sc.

Major Advisor

_____

Dr. James F. Rusling

Associate Advisor

_____

Dr. Dharamainder Choudhary

Associate Advisor

_____

Dr. Jing Zhao

University of Connecticut
2018

This dissertation is dedicated to

Drs. Marie Curie and Lise Meitner,
I could not ask for more inspiring people to share my birthday with;

Grand-aunt Dr. Ratna Phadke,
for being the first to get her doctorate in our family;

and

to all the amazing fellow PhD students I know and love,
I cherish every moment of laughter, tears, commiserations, and joy we shared.

2018

Acknowledgements

I would like to thank my advisor, Dr. James Rusling for all the support, conversations, and guidance during these past six years. I am a better science communicator thanks to your relentless advice. I would also like to thank Dr. Dharamainder Choudhary for answering the many biology questions and supporting me patiently throughout our collaboration. Thank you Dr. Jing Zhao for agreeing to be part of my committee and your advice through the years. I am equally grateful to Dr. Mark W. Peczuh for being a mentor, and a patient listener. Thank you Dr. Steven Suib for being a knowledgeable collaborator and for sitting in on my thesis viva. I would also like to acknowledge Dr. Edward Neth, for all the tech support and for being an awesome person to TA for, and Dr. Angeles-Boza, for agreeing to sit in on my general exam last minute.

Graduate school would not have been the same without the company of one Dr. Jennifer Satterwhite-Warden. Thank you for being there during the long, frustrating days as we worked together to finish the roller coaster of a project, and for being a steady friend. A special thank you to my collaborators Dr. Niluka Wasalathanthri and Adam Markman, our long chats over the past two years have been truly enjoyable. I am also grateful to members of the Rusling lab, many of whom have become close friends. Thank you Colleen, Brunah, Amit, Abby, Kiki, Spundana, Karteek, Dhanuka, Greg, Chandra, Chi, Ketki, Min, Islam, Mohammed, Di, Itti, Dana, Boya, Snehasis, Keshani, and rest of Rusling group. Special thanks to Emilie, Charlene, Adam, Daniel, and rest of chemistry staff, you made life in chemistry department easy for us all.

My time at UConn has been memorable thanks to the people whom I get to call friends. Julie and Kelli, I'll miss those basketball games. Lani, Karla, Athina, Aditya, Curt, and Thursday

night gang, chemistry would not be as much fun without you all. Dhurga, Prajakta, thank you for making Forster drive outstanding. Thanks to Barbara, Leanne, and Deborah for welcoming me into your home and family.

Some pretty special people kept me sane and got me through graduate school in one piece, many of who I met through GEU: Ameya, Cera, Casey, Holly, Monique, Ken, Kate, Madeline, Steven, Todd, Siavash, Adam, Sara, Ellie, Maria, Jessica, Krista, and many more I have missed here. You made my American experience unforgettable!

Special thank you to Holly, Abby, Kate, Ketki, Natasha, and Deepika for getting me through the past couple of arduous months. Raeesa, Sindhu, Ishan, you have been my constant supporters, and friends who have now become family. Thank you Raeesa and Uddhav for keeping me honest to the deadlines I set during the thesis-writing ordeal.

Lastly, to my crazy family, I love you and am grateful to have you with me through all the ups and downs. Gireeja, please still help me with photoshop even if I ask you a million questions. Aai (Sushama), Baba (Sunil), you may not have always understood what I do or why I do it, but it makes your support and encouragement all the more sweet.

Table of Contents

List of Figures

List of Schemes

List of Tables

Chapter 1

Introduction

1.1 Goals and Significance

Richard Feynman, Nobel Prize-winning physicist and author of the memorable "Surely You're Joking, Mr. Feynman!", proposed the concept of nanotechnology in 1959. Nanotechnology has since become ubiquitous in modern life, from drug design and renewable energy applications to cosmetics and other household items. Nanotechnology-enabled global revenue surpassed $1 trillion in 2013[1] and continues to grow at a rapid pace. Medical applications alone, including drug design, delivery, and diagnostics market, contribute to over 20% of this revenue.[2] The National Nanotechnology Initiative (USA) has received over $1.2 billion in federal funding and invests heavily in research initiaves.[3] Research output in nanotechnology is outpacing overall research output with over 400,000 publications between 2010-2014 alone.[4]

Nanotechnology has been harnessed in improving analytical platforms in a versatile manner, reducing the burden on resources by automating, miniaturizing, and simplifying components of the analytical device (see Figure 1.1).[5] Automation is achieved by incorporating strategies such as on-line sample preparation protocols,[6,7] synthesizing nano-materials for use with nano-volumes,[8,9] and lab-on-chip micro/ nanofluidic devices.[10,11] Utilization of pressure driven flows systems with nano-pumps have assisted miniaturization of analytical platforms.[12,13] Advances in synthesis of multifunctional nanomaterials, such as silica nanoparticles with magnetic cores, have allowed simplification of analytical protocols by combining multiple assay

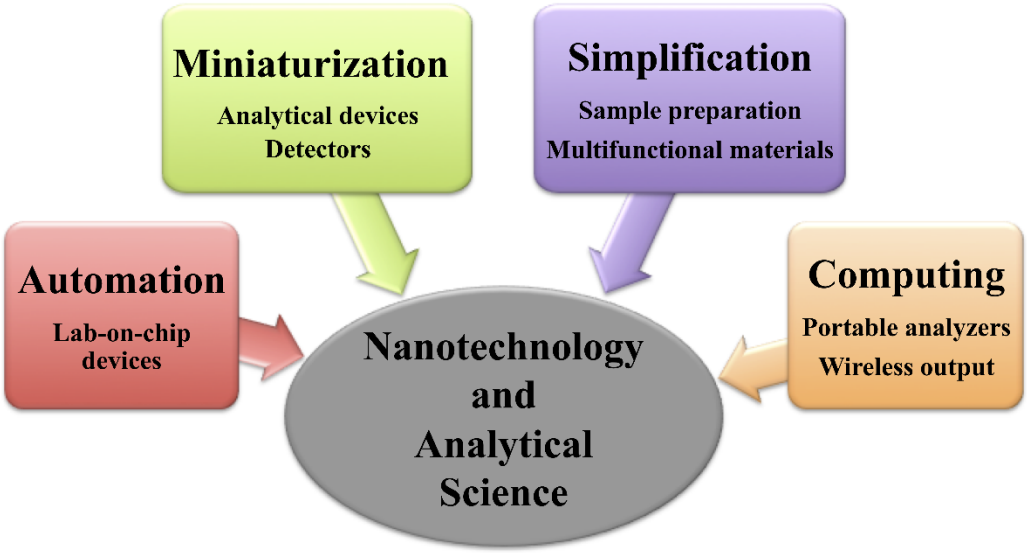

Figure 1.1: Analytical platforms can be automated, miniaturized, and simplified to construct low-cost, high throughout devices. Combining these devices with the advanced computing allows for portable, wireless analytical devices.[5]

steps. Combining these new systems with miniaturized detectors has led to construction of portable systems.[14,15] Integration of these devices with wireless technology or portable computing stations allows for point of care (POC) analytical platforms.[16,17]

Nanomaterials, in particular, have a unique advantage as their synthesis can be tailored to suit eventual application by tuning their properties, such as size, composition, surface modification, shape, and even assembly into larger structures, making them imminently suitable to different analytical chemistry platforms.[18] These are currently used in various aspects of analytical chemistry processes, from their study as test molecules (small biomolecules, proteins, DNA/ RNA)[5] to their utilization as analytical tools (optical tags, conductive inks)[15,16]. Some of

the heavily commercialized applications of nanomaterials are in sample pre-treatment,[19,20] chromatography,[8,21,22] and optical detection.[23,24] Advancements in multi-functional surface modification of nanoparticles and device fabrication techniques, such as inkjet printing, has boosted development of lab-on-chip analytical devices.[25] With miniaturization and portable analyzer components, several portable and POC devices have been developed for analysis of environmental pollutants, biological matrices, and food products.[26]

POC devices provide rapid analytical alternatives to bulky, highly technical, and often-costly analytical methodologies located at centralized laboratories.[17,27] POC platforms often do not require technical training; in fact, many are specifically geared towards home usage, such as glucose monitoring systems or home pregnancy tests. In case of time-sensitive samples, the cost could increase substantially when conducting analysis by conventional methods as compared to portable technology. Simplification of analytical methods and miniaturization of device to make such devices portable often results in reduced sample preparation steps, lower required sample volumes, and greener methodologies; rigorous testing prior to field application ensures high analytical compliance and accurate testing.

In this thesis, multiple aspects of sensor development incorporating nano-materials are explored. First, L-selectin protein is evaluated in serum samples from bladder cancer patients to establish a preliminary correlation between disease stage and protein concentration. Other works focus on inkjet printing nanoparticles to develop sensors with versatile applications. An optical tag is developed with Zinc oxide particles to aid in improved anti-counterfeiting measures. Preliminary studies are conducted into inkjet printing disposable electrode sensors with novel bronze conductive ink. Lastly, a design for multiplexed catalytic reactor, incorporating inkjet printed catalytic nanoparticles and 3D printed well plate reactor, is described. The thesis

highlights the versatility offered by integrating nano-materials in analytical methodologies, both as analytes of interest and as analytical tools for sensing methodology.

1.2 Discovery and Applications of Biomarkers

A National Health Institute (NIH) working group in 2001 defined a biomarker as, "*a characteristic that is objectively measured and evaluated as an indicator of normal biologic processes, pathogenic processes, or pharmacologic responses to a therapeutic intervention.*"[28] The definition encompasses biological molecules, such as metabolites, hormones, proteins, RNA, or DNA, found in blood, urine, and other body fluids or tissues that indicate the presence of a disease. Two of the most well know tests for biomarkers include the home pregnancy tests and the glucose check test.[17] In case of cancer, these markers differentiate an affected patient from one without the disease: Germline or somatic mutations, transcriptional changes, post-translational modifications, etc. are key causes of such changes.[29]

The American Cancer Society predicts roughly 1.7 million new cases of cancers and 609,000 deaths from cancer in the US, nearly 1670 deaths per day.[30] According to the World Health Organization, cancer is the second leading cause of death worldwide accounting for roughly 15% of all deaths.[31] Cancer patients have 50-90 % survival rate if it is caught at localized stage, compared to less than 30% when it is spread to lymph nodes or other organs, emphasizing the need for accurate early diagnostic tools.[30] As tumors are hard to detect at early stages due to invasive biopsies required for confirmation, biomarkers can fill an important gap in clinical tests available. Cancer biomarkers can be a combination of biochemical changes, including gene expression, proteomic alterations, and metabolomics signatures.[29] Biomarkers in circulating, secreted, or excreted body fluids (blood, sputum, urine) can be analyzed relatively

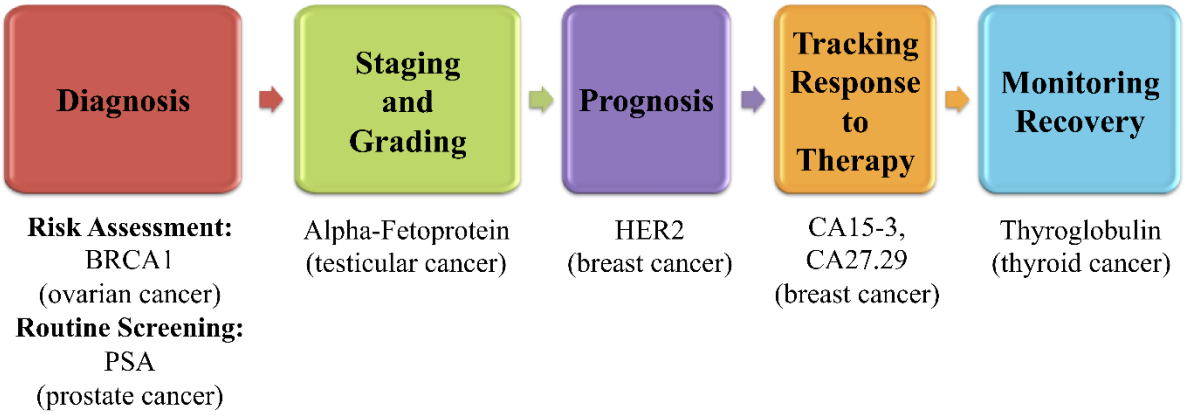

Figure 1.2: Cancer biomarkers can be incorporated into clinical use from diagnosis to monitoring recovery. Examples of FDA approved biomarkers presently in clinical use, ranging from risk assessment, routine screening, diagnosis, determination of stage and prognosis, tracking response to therapy, and monitoring, are provided to exemplify the importance of cancer biomarker discovery.[32]

non-invasively, however tissue markers require extensive biopsy or imaging for evaluation.

The potential diagnostic applications in oncology exist at every stage of the disease and resulting therapy, including genetic or environmental risk assessment, diagnosis of disease, staging/ grading of cancer, tracking response to treatment (Figure 1.2).[29] Establishing clinical relevance of a potential biomarker involves extensive evaluation and validation of analytical methodology, followed by assessment of clinical utility in a large patient sample pool (usually > 1000 samples) prior to establishing a routine clinical test. FDA has approved a few protein biomarkers for cancer diagnostics, such as HER2 for breast cancer and PSA for prostate cancer (Figure 1.2),[32,33] while more are still being evaluated for clinical utility. Often these proteins are

found at elevated concentration in blood (with some exceptions) and are useful in disease detection prior to onset or detection of tumors; e.g. prostate specific antigen (PSA) blood test is recommended for older men as part of routine annual check as an early screening for prostate cancer. Some proteins however may be associated with multiple cancers, such as Interleukin-6 (IL-6), necessitating the need for a panel of biomarker tests to establish clinical relevance.

1.3 Protein Detection Platforms

An array of analytical techniques is currently employed for protein detection. ELISA or enzyme linked immunosorbent assays are the gold standard for protein quantification and still heavily used for clinical testing. Analysis in ELISA relies on protein-antibody interactions, while other techniques such as flow cytometry, and bioimaging also employ similar interactions for analysis of different target biological media or organs. The main challenger to ELISA as a clinical analytical tool is liquid chromatography-mass spectrometry systems, a relatively new but rapidly expanding methodology. Our laboratory employs an electrochemical detection technique in a modified ELISA format, which aids more sensitive detection protocols. All of these techniques are briefly discussed here.

1.3.1 Antigen-Antibody Interactions

Antigens are foreign molecules that can induce an immune response in the human body. Some examples of external xenobiotic agents are pollutants, virus or bacteria particles, or even foreign protein matter. Antigens often present several epitopes on the surface of their body that are recognized by antibodies. Antibodies, also known as immunoglobulins (Ig, molecular weight ~ 150,000 Da), are produced by the immune system to combat any potential diseases on

exposure to antigens. Heavy and light peptide chains form the Y-shaped glycoprotein of an antibody, as seen in Figure 1.3, with a crystallizable or constant region (F_c) and an antigen-binding fragment (F_{ab}).[34] The F_c region binds to parts of the immune system, including lymphocytes. The F_{ab} region recognizes the target antigen, through antibody-antigen interaction by binding to specific epitopes of the antigen.

Antibodies are highly specific towards a certain antigen or even specific epitope of a given antigen. The antigen-antibody interactions are often through a combination of van der Waals forces, hydrogen bonds, hydrophobic, and electrostatic interactions, whereby the epitope fits into the binding pocket of the antibody.[35] The antibody-antigen interactions occur with high affinity and specificity, improving the scope of its application to ELISA. Specifically with

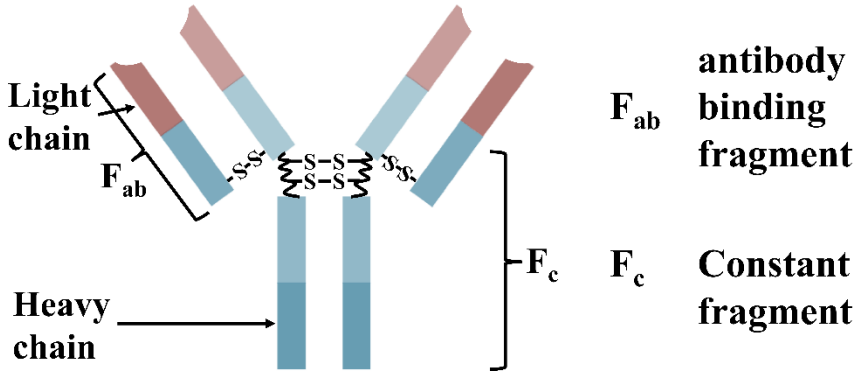

Figure 1.3: Structure of antibody or immunoglobulin protein. The light chain contains multiple binding sites that can recognize specific epitopes on antigens, thus providing selectivity to immunoassays.

protein biomarkers, antibodies are commercially produced for specific recognition of target protein. Antibodies are generally available in monoclonal and polyclonal forms. The former recognizes a single epitope on the target protein, whereas the latter contains binding sites for multiple epitopes. ELISA utilizes either a single or a pair of antibodies for capture and detection protocols. The high specificity in antibody-protein interactions makes ELISA methodology uniquely selective for protein quantification.

1.3.2 Enzyme-linked Immunosorbent Assay

A ubiquitous assay for clinical protein quantification, enzyme-linked immunosorbent assay (ELISA) is a solid-phase assay for detection of peptides, proteins, antigens, and even hormones. In ELISA, detection is achieved by specific capture of a target protein with complementary detection antibody tagged with an enzyme label, followed by spectroscopic detection using a substrate-enzyme reaction.[35] Commonly, horseradish peroxidase (HRP) or alkaline phosphatase (AP) are used as an enzyme label, while the choice of a substrate depends on detection mechanism, i.e. spectrophotometry, fluorescence, or luminescence.[35] The assay is carried out in a 96- or 384- well format that has enables automation and commercialization of the assay.

The primary ELISA formats in use can be categorized on basis of antigen capture method and detection method, as in Figure 1.4. Antigen can either be directly immobilized on the plate through physical adsorption (Figure 1.4A-B) or indirectly via capture antibody immobilized on the plate (Figure 1.4C). In each case an antibody, tagged with an enzyme label, is used for detection. In an indirect assay, a secondary antibody is captured on the detection antibody, the former being tagged with the enzyme label (Figure 1.4B). Perhaps most common is the

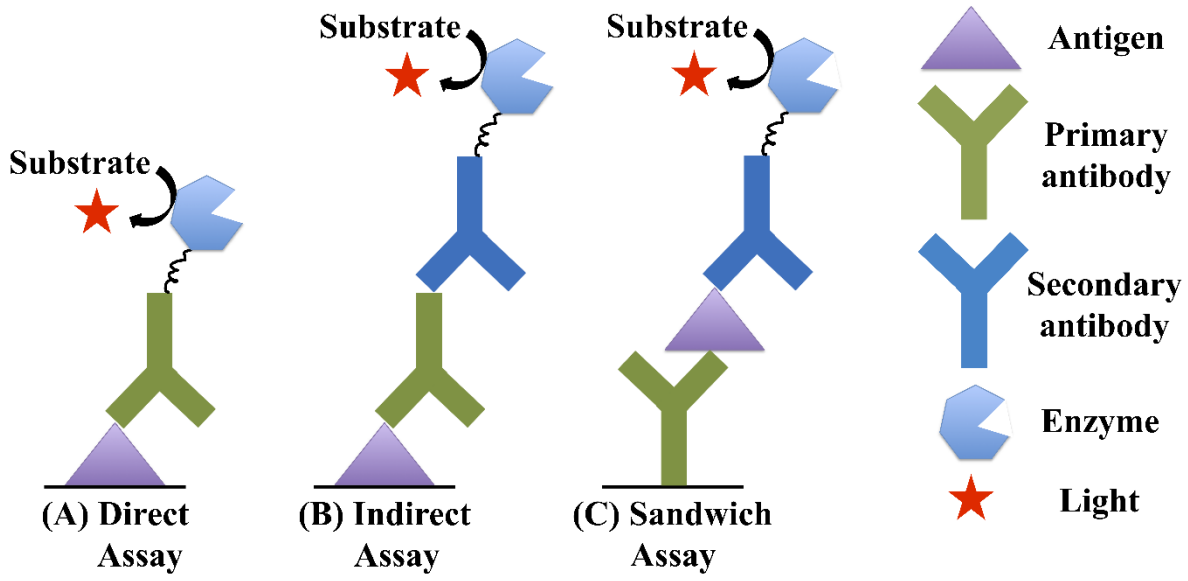

Figure 1.4: ELISA operational platforms include (A) direct, (B) indirect, and (C) sandwich assay. The sandwich assay, with surface bound capture antibody, is perhaps most commonly used as the gold standard in protein detection.

"sandwich" format, where a primary (or capture) antibody (Ab_1) specific to target protein is attached to the bottom of a well plate (Figure 1.4C). Samples containing the target protein are then added to the well and allowed to incubate for a specified time. Unreacted sample is removed via washing, followed by the incubation with the secondary (or detection) Antibody (Ab_2). The secondary antibody is tagged with the enzyme label. Once incubation and subsequent washing is complete, a substrate chemical is introduced which on conversion by the enzyme produces optical output. Typically, a visible signal is produced and is read by a spectrophotometer. Commercially available ELISAs have low detection limits in picogram per milliliter (pg mL^{-1})

range, which can be improved to high femtogram per milliliter (fg mL^{-1}) with use of fluorescence tags if needed.

Several ELISA kits and automation systems are available commercially, as seen in Table 1.1. Some multiplex analyzers are commercially available (Table 1.1), capable of measuring up to 10 proteins simultaneously. Systems like Luminex (R&D systems), FirePlex (Abcam) employ fluorescence detection, while Roche Diagnostics or Mesoscale Discovery use electrochemiluminescence. Even surface plasmon resonance has been applied to ELISA based protein detection by Horiba Inc. and BIO-RAD.

Detection method	**Multiplexing**	**Automation**	**Detection limit**	**Commercial Suppliers**
Spectrophotometry	Single	No	pg mL^{-1}	Quantikine,[36] SimpleStep[37]
Spectrophotometry	up to 8	Yes	pg mL^{-1}	Elysis[38]
Fluorescence	20 - 75	Yes	pg mL^{-1}	Luminex,[39] FirePlex[40]
Electrochemiluminescence	up to 10	No	High fg mL^{-1} to pg mL^{-1}	MESO QuickPlex[41]
Surface Plasmon Resonance	up to 6	No	pg mL^{-1}	ProteOn[42]

Table 1.1: ELISA platform has been commercialized in a versatile selection of assays, including single biomarker kits, automated multiplexed instruments. Introducing colorimetry, fluorescence, electrochemiluminescence, and even surface plasmon resonance detection techniques has also diversified its applications.

ELISA detection mechanism has been adapted to versatile biological sample detections: Protein attached to cell surfaces or present within cell too can be detected. Flow cytometry has been employed for cellular surface proteins, where detection antibodies with fluorescent tags are incubated with the sample.[35] As cells with completed immunoassay pass the detection cell, the fluorescence from captured antibodies is quantified. Recently, intracellular proteins have been successfully detected with flow cytometry by rendering the cell membrane permeable and subsequently staining target proteins by fluorescent antibodies.[43] Similar approach is used in case of in vivo imaging of target proteins: Fluorescent antibodies are injected into the test subject, which travel to areas containing the analyte. Imaging can potentially show protein distribution in organs aiding diagnosis of some cancers.

ELISAs have consistently been used for clinical quantification of proteins and often yield reliable results, although they are time and labor intensive, and require large sample volumes. The latter is particularly disadvantageous when multiple proteins panels need to be screened.[27] Nevertheless, multiplexing requires expensive consumables and reagents, including chips and laser sources. The best commercially available alternative for simultaneous multi protein quantification with high sensitivity and specificity is mass spectrometry based proteomics. In research stages, an array of electrochemical protein detection techniques are investigated that offer a cheaper and more robust analytical platform.

1.3.3 Electrochemical Detection platforms

Electrochemical detection is a low-cost and robust alternative to ELISA methodology, suitable for developing portable devices without expensive equipment; electrical signals are also more suitable for electronic displays in POC device construction. The rapidly market integrated

handheld glucose meters, accounting for nearly 85% of the POC market[44], use electrochemical detection methodology highlighting its robustness for such application.

ELISA methodology has been simplistically adapted to electrochemical platforms by electrode surface modification with Ab_1. The sandwich immunoassay is then developed on the electrode chips as in ELISA, however the enzyme is selected for an electrical output, in contrast to an optical output, on reaction with the substrate. Detection tracks changes in electrical parameters, such as impedance, conductance, potential, or current, the last two being easiest to incorporate into POC devices. HRP, one of the common ELISA enzyme labels, has well-established electrochemical reactions with multiple substrates.[45] Other enzymes or substitute materials used for electrochemical immunoassays include AP, glucose oxidase, and conductive polymers.[46]

HRP contains a single central heme group that readily undergoes catalytic oxidation/reduction in the presence of hydrogen peroxide (Scheme 1.1). Hydrogen peroxide oxidizes iron in the heme center to its oxidized form (Fe^{IV}=O), thus activating the enzyme. The enzymes can then be easily reduced at the electrode surface during reaction with the substrate. Multiple enzyme labels can be introduced on the sensor surface by incorporating nanoparticles with multiple surface-bound enzyme labels, thus amplifying signal generation and increasing assay sensitivity beyond conventional ELISA capabilities.[46] This approach has been further discussed in chapter 2.

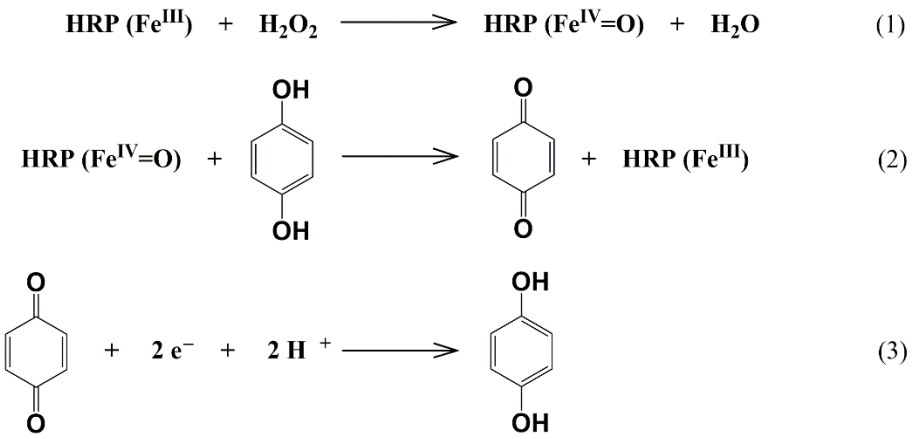

Scheme 1.1: Electrochemical signal generation with HRP enzyme labels. HRP is readily oxidized at the heme center in presence of H_2O_2 (1) and is the reduced in the presence of a substrate such as hydroquinone (2). The benzoquinone generated in (2) can be reduced at the electrode surface generating a current (3).

1.4 Nanoparticles in Electrochemical Immunoassays

Nanoparticles have drawn attention for use in electrochemical assays due to the possibility of developing multi-label, multi-functional sensing molecules. Nanoparticles were however initially used to increase electrochemically active surface area of the electrodes in electrochemical immunosensors. As nanoparticles have high surface-to-volume ratios, researchers could achieve lower detection limits and higher sensitivity to reach clinically relevant concentration ranges.[47] Dequaire et al[48] first used gold nanoparticles bound to multiple detection antibodies in an electrochemical sandwich immunoassay, by measuring stripping voltammetry.

Newer approaches, while not focusing on stripping of the nanoparticles, have used metallic or polymeric nanoparticles, or quantum dots with multiple enzyme and antibody labels to amplify electrochemical measurements, including impedence, amperometry, and voltammetry, in modified ELISA platforms. As previously discussed attaching multiple enzyme labels to nanoparticles can greatly enhance the sensitivity: Wang et al[49] were the first to use such bioconjugates for detection of DNA, wherein thousands of alkaline phosphatase and probe DNA were surface bound to multiwall carbon nanotubes to achieve femtomolar detection of IgG in buffer.

Our research heavily employs nanoparticles, magnetic beads, single walled carbon nanotubes (SWCNs), for both electrode surface area enhancement and bioconjugate formation, in designing ultrasensitive electrochemical biosensors for cancer protein biomarkers.[45,46,50,51] Earlier, shortened single wall carbon nanotubes (SWCNs) have been self-assembled into an upright carbon nanotube "forest" from DMF solutions onto electrode surface pre-coated with thin iron oxide-Nafion layer.[52,53] Antibodies are surface-bound by amide coupling using 1-(3-(dimethylamino)propyl)-3ethylcarbodiimide hydrochloride (EDC) and N-hydrosulfosuccinimide (NHSS), as the SWCNs have end carboxyl groups. Antibody concentration on the electrodes increases 10-15 fold, leading to 10-fold signal increase during the electrochemical immunoassays.

Alternatively, ~ 5 nm glutathione-protected gold nanoparticles have been used to increase electrochemically active surface area of screen-printed carbon electrodes and to introduce surface carboxyl groups, to which antibodies can be covalently bound through carbodiimide chemistry.[45] The nanoparticles are coated on electrode surface through simple layer-by-layer assembly protocol.[54] Additionally, magnetic particles decorated with protein detection antibodies

and HRP enzyme labels are used to introduce further signal amplification. The magnetic beads allow for sample purification as the bioconjugates can be washed after Ab_2-protein conjugation prior to incubation with Ab_1. These superparamagnetic beads range in size from 500 nm to 50 μm, and provide a simple and inexpensive alternative to using nanoparticles. Further modification to assay protocol introduces use of biotin-antibodies and biotin-HRP labels with streptavidin-coated magnetic beads for rapid and reliable synthesis of such bioconjugates.[45] Similar electrochemical protocol has been adapted to analysis of L-selectin protein in chapter 2.

1.5 Inkjet Printing

Inkjet printing is a non-impact deposition technology, capable of printing a two-dimensional pattern with versatile selection of inks on multiple substrates. High level of commercial interest led to development of continuous and drop-on-demand inkjet printers, with both finding a niche for industrial applications. Inkjet or 2D printing relies on gravity-formed droplet deposition. Prototypes of earliest two-dimensional printers were developed and marketed during 1950s and 60s.[55] With the innovation of drop-on-demand technology, and its adaptation to other media in 1970s and 80s, improved their potential for customized patterns, increasing range of their applications.[56–58]

Presently, two-dimensional matrixes of drops are used to design thin films from organic compounds, inorganic particles,[59] biomolecules,[59] and polymers[60] with versatile thermal,[61] electrical,[50,62] optical[63] properties. More recently, 2D printers have been adapted to construct 3-dimentional scaffolds and structure with applications in pharmaceuticals,[64] live tissues,[65] and ceramics.[66]

1.5.1 Continuous printing

In continuous printing, a stream of ink is broken into high-speed individual droplets by application of vibrations, as seen in Figure 1.5. Further downstream, droplets are selectively charged to control the droplet size (typically 20 - 150 mm)[67] and trajectory towards the substrate. Unused ink is collected in a waste container, which may be recycled. Printing is performed with either uncharged or charged droplet streams in single-dot or multiple-dot printers respectively, the latter providing higher speeds of printing.[55,68]

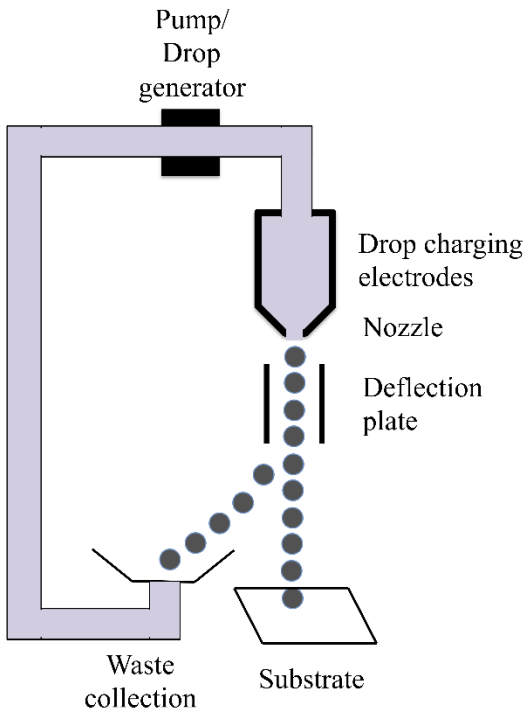

Figure 1.5: Schematic of continuous inkjet printing process. The ink droplets generated pass through a pair of high voltage deflection plates. A controlled droplet size moves on towards the substrate. Deflected ink droplets are collected and may be circulated for reuse.

This low resolution, but high-speed technology has found extensive use in printing labels in manufacturing, such as date, and time stamps. The adaptability of continuous inkjet printing to analytical and biological applications is limited. The reasons are two-fold: Cost and inflexible ink selection. The high equipment and maintenance cost, in addition to high volume of ink wastage prevents extensive implementation of this technology. More importantly, applications are reduced to inks that can be charged, while using volatile solvents.

1.5.2 Drop-on-demand printing

Drop-on-demand (DOD) printing employs pressure pulses for "on-demand" droplet formation, replacing the charging and deflection systems used in continuous printing, as seen in Figure 1.6A. Thermal (Figure 1.6B)[69,70] or piezoelectric (Figure 1.6C)[56,71,72] element is used most frequently to achieve droplet formation. Other mechanisms in developmental stages use acoustic,[73,74] electrostatic,[75] electrohydrodynamic,[76] and valve pressure pulses.[77] In contrast to continuous inkjet printing, droplets < 20 mm in diameter are achieved;[55,78] combining it with time controlled printing enhances the accuracy and resolution of this technology. Further, the removal of charging requirements expand applications of DOD printing to multi-functional inks, including polymers, biological materials, and ceramics.

Thermal DOD printers use thermal evaporation of ink solvents for droplet formation. Heating up to 400˚C is achieved in ≤ 10 second timespan at a heating element in the path of ink flow. Solvent evaporation at the surface of this heating element forms an air bubble leading to ink droplet expulsion, see Figure 1.6B; fresh ink fills the chamber as the air bubble collapses.[79] Thermally stable inks in low-boiling solvents are required for this DOD process, limiting its

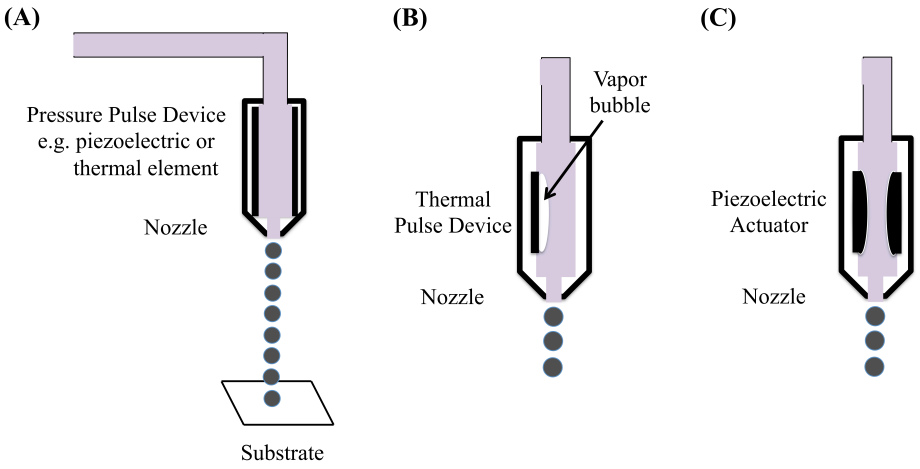

Figure 1.6: Schematic for (A) a generic drop-on-demand inkjet printer. The pressure pulse device is commonly either (B) thermal or (C) piezoelectric. Drops are generated due to contracting and expanding vapor bubble or the flexing of a piezo-material in thermal and piezoelectric devices respectively.

applicability in printing thermally sensitive inks and biological media. However, phase-change inks, low-melting salts can be printed consistently with thermal inkjet printers.

Piezoelectric printing utilizes an expandable element of piezoelectric material, controlled by electric voltage ramps to generate pressure pulses required for DOD printing (Figure 1.6C). As the element expands on application of a voltage, an ink droplet leaves the holding chamber. The retraction to original shape by this element fills the chamber with fresh ink.[79,80] This non-interactive, physical process of droplet formation in piezoelectric DOD printers makes them universally suitable to all types of inks. While the cost associated with piezoelectric element and software is high, the easy control over droplet size by variation in voltage, pulse length and

frequency, and the aperture of ink release has attracted considerable use in analytical and biological applications.

1.6 Overview of Dissertation

Sensor development encompasses versatile approaches in analytical chemistry, including biomarker discovery, sensor fabrication, and analysis. Each of these stages can use nanotechnology for tunable and customized approach leading to low-cost, yet accurate analytical platforms. This thesis aims to address the different aspects of sensor development through showcasing a few applications of analytical tools. Firstly, an existing electrochemical immunoarray methodology is adapted to the evaluation of CD62L protein in metastatic bladder cancer, with the goal of commenting on clinical relevance as a possible biomarker. Secondly, nanoparticles are used in multiple approaches utilizing inkjet printing for the development of thin film sensors, including construction of anti-fraud QR code, printing disposable sensors, and fabrication of a catalytic reactor.

Chapter 1 introduces the contextual significance of the work completed, including the importance of nanomaterials in analytical chemistry research, portable sensor design, protein detection strategies, and inkjet printing technology. The chapter delivers the information needed to highlight the rational approach adapted to applications of nanomaterials in biomarker discovery and thin film sensors. The technologies detailed in this chapter provide a theoretical framework for the work presented in this dissertation.

Chapter 2 details an adaptation of a well-established semi-automated microfluidic electrochemical immunoarray methodology towards the quantification of L-selectin protein in bladder cancer patients. The bead-based electrochemical immunoarray provides a sensitive, low

cost alternative to conventional immunosorbent protein assays, which is able to accurately quantify the protein in low-volume serum samples, while maintaining a low patient sample dilution factor. The results indicate the immunosensor to be more reliable than the gold standard ELISA. L-selectin shows distinct elevation in serum concentration for bladder cancer patients compared to cancer-free controls, suggesting possible clinical relevance as a biomarker.

Chapter 3 concentrates on the development and fabrication of a chemical identification tag for the purpose of improved anti-fraud measures. Zinc oxide nanoparticles, in pure or doped solutions, with selective optical properties are inkjet printed in form of QR codes. These are analyzed by dispersion properties to classify true and false optical tags, providing an elegant solution to improve counterfeit detection methods. Inkjet printing these thin film sensors provides a low-cost approach to manufacturing that is adaptable to variety of printing substrates, as evidenced by the prototype prints on ICs. Possible applications include security tags on electronic components, therapeutics, and other high value materials.

Chapter 4 introduces the application of inkjet printed to disposable thin-film electrochemical sensors and catalytic reactors. In part one, a novel bronze material is evaluated for its dispersive properties and possible utilization as a conductive ink for an electrochemical sensor. The parameters involved in substrate and ink optimization for inkjet printing these nanomaterials are discussed. Further work will include printing of the sensors, and evaluating their electrochemical performance. Part two details a design for well plate format 3D printed catalytic reactor that incorporates inkjet printed catalytic nanomaterials. Manganese oxide sol-gel materials with known catalytic properties are optimized for inkjet printing. An integrated inkjet and 3D printed reactor system is designed for multiplexed catalytic performance evaluation.

Further work will include printing of the prototype and evaluating its performance with simple electrocatalytic reactions.

1.7 References

(1) Market report on emerging nanotechnology now available, 2014. National Science Foundation Web Site. https://www.nsf.gov/news/news_summ.jsp?cntn_id=130586 (accessed May 8, 2018).

(2) Evers, P. *Nanotechnology in Medical Applications: The Global Market; HLC069C*; BCC Research, 2015.

(3) NNI Budget, 2018. National Nanotechnology Initiative Web Site. https:// www.nano.gov/about-nni/what/funding (accessed May 8, 2018).

(4) Elsevier. *Nanotechnologies Output, Impact and Collaboration - A Comparative Analysis of France and Other Countries*; 2015.

(5) López-Lorente, Á. I.; Valcárcel, M. Analytical Nanoscience and Nanotechnology. In *Gold Nanoparticles in Analytical Chemistry - Comprehensive Analytical Chemistry*; López-Lorente, Á. I., Valcárcel, M., Eds.; Elsevier: Poland, 2014; Vol. 66, pp 3–35.

(6) Boonjob, W.; Miró, M.; Segundo, M. A.; Cerdà, V. Flow-through Dispersed Carbon Nanofiber-Based Microsolid-Phase Extraction Coupled to Liquid Chromatography for Automatic Determination of Trace Levels of Priority Environmental Pollutants. *Anal. Chem.* **2011**, *83* (13), 5237–5244.

(7) Spietelun, A.; Marcinkowski, Ł.; de la Guardia, M.; Namieśnik, J. Recent Developments and Future Trends in Solid Phase Microextraction Techniques towards Green Analytical Chemistry. *J. Chromatogr. A* **2013**, *1321*, 1–13.

(8) Lavrik, N. V.; Taylor, L. T.; Sepaniak, M. J. Nanotechnology and Chip Level Systems for Pressure Driven Liquid Chromatography and Emerging Analytical Separation Techniques: A Review. *Anal. Chim. Acta* **2011**, *694* (1–2), 6–20.

(9) Bhadra, M.; Mitra, S. Nanostructured Membranes in Analytical Chemistry. *TrAC Trends Anal. Chem.* **2013**, *45*, 248–263.

(10) Tennico, Y. H.; Hutanu, D.; Koesdjojo, M. T.; Bartel, C. M.; Remcho, V. T. On-Chip Aptamer-Based Sandwich Assay for Thrombin Detection Employing Magnetic Beads and Quantum Dots. *Anal. Chem.* **2010**, *82* (13), 5591–5597.

(11) Liu, S.; Zhao, Y.; Parks, J. W.; Deamer, D. W.; Hawkins, A. R.; Schmidt, H. Correlated Electrical and Optical Analysis of Single Nanoparticles and Biomolecules on a Nanopore-Gated Optofluidic Chip. *Nano Lett.* **2014**, *14* (8), 4816–4820.

(12) Manz, A.; Effenhauser, C. S.; Burggraf, N.; Harrison, D. J.; Seiler, K.; Fluri, K. Electroosmotic Pumping and Electrophoretic Separations for Miniaturized Chemical Analysis Systems. *J. Micromech. Microeng.* **1994**, *4*, 257–265.

(13) Blom, M. T.; Chmela, E.; Oosterbroek, R. E.; Tijssen, R.; van den Berg, A. On-Chip Hydrodynamic Chromatography Separation and Detection of Nanoparticles and Biomolecules. *Anal. Chem.* **2003**, *75* (24), 6761–6768.

(14) Zhang, S.; Wang, S.; Zhang, X. A Catalytic Nanomaterial-Based Optical Chemo-Sensor Array. *J. Am. Chem. Soc.* **2006**, *128* (45), 14420–14421.

(15) Pumera, M.; Escarpa, A. Nanomaterials as Electrochemical Detectors in Microfluidics and CE: Fundamentals, Designs, and Applications. *Electrophoresis* **2009**, *30* (19), 3315–3323.

(16) Sandhu, A.; Handa, H.; Abe, M. Synthesis and Applications of Magnetic Nanoparticles for Biorecognition and Point of Care Medical Diagnostics. *Nanotechnology* **2010**, *21* (44), 442001.

(17) Luppa, P. B.; Müller, C.; Schlichtiger, A.; Schlebusch, H. Point-of-Care Testing (POCT): Current Techniques and Future Perspectives. *TrAC Trends Anal. Chem.* **2011**, *30* (6), 887–898.

(18) Wang, P.; Lin, Z.; Su, X.; Tang, Z. Application of Au Based Nanomaterials in Analytical Science. *Nano Today* **2017**, *12*, 64–97.

(19) Kaur, A.; Gupta, U. A Review on Applications of Nanoparticles for the Preconcentration of Environmental Pollutants. *J. Mater. Chem.* **2009**, *19* (44), 8279–8289.

(20) Lucena, R.; Simonet, B. M.; Cárdenas, S.; Valcárcel, M. Potential of Nanoparticles in Sample Preparation. *J. Chromatogr. A* **2011**, *1218* (4), 620–637.

(21) Gross, G. M.; Nelson, D. A.; Grate, J. W.; Synovec, R. E. Monolayer-Protected Gold Nanoparticles as a Stationary Phase for Open Tubular Gas Chromatography. *Anal. Chem.* **2003**, *75* (17), 4558–4564.

(22) Duan, A.-H.; Xie, S.-M.; Yuan, L.-M. Nanoparticles as Stationary and Pseudo-Stationary Phases in Chromatographic and Electrochromatographic Separations. *TrAC Trends Anal. Chem.* **2011**, *30* (3), 484–491.

(23) Murphy, C. J.; Sau, T. K.; Gole, A. M.; Orendorff, C. J.; Gao, J.; Gou, L.; Hunyadi, S. E.; Li, T. Anisotropic Metal Nanoparticles: Synthesis, Assembly, and Optical Applications. *J. Phys. Chem. B* **2005**, *109* (29), 13857–13870.

(24) Sha, M. Y.; Xu, H.; Penn, S. G.; Cromer, R. SERS Nanoparticles: A New Optical Detection Modality for Cancer Diagnosis. *Nanomedicine* **2007**, *2* (5), 725–734.

(25) Komuro, N.; Takaki, S.; Suzuki, K.; Citterio, D. Inkjet Printed (Bio)Chemical Sensing Devices. *Anal. Bioanal. Chem.* **2013**, *405* (17), 5785–5805.

(26) Zhang, Y.; Ge, S.; Yu, J. Trends in Analytical Chemistry Chemical and Biochemical

Analysis on Lab-on-a-Chip Devices Fabricated Using Three-Dimensional Printing. *TrAC Trends Anal. Chem.* 2016, pp 166–180.

(27) Rusling, J. F.; Kumar, C. V.; Gutkind, J. S.; Patel, V. Measurement of Biomarker Proteins for Point-of-Care Early Detection and Monitoring of Cancer. *Analyst* **2010**, *135* (10), 2496–2511.

(28) Atkinson, A. J.; Colburn, W. A.; DeGruttola, V. G.; DeMets, D. L.; Downing, G. J.; Hoth, D. F.; Oates, J. A.; Peck, C. C.; Schooley, R. T.; Spilker, B. A.; et al. Biomarkers and Surrogate Endpoints: Preferred Definitions and Conceptual Framework. *Clin. Pharmacol. Ther.* **2001**, *69* (3), 89–95.

(29) Henry, N. L.; Hayes, D. F. Cancer Biomarkers. *Mol. Oncol.* **2012**, *6* (2), 140–146.

(30) American Cancer Society. *Cancer Facts & Figures 2018*; Atlanta, 2018.

(31) World Health Organization. *World Health Statistics 2017: Monitoring Health for the SDGs, Sustainable Development Goals*; Geneva, 2017.

(32) Ludwig, J. A.; Weinstein, J. N. Biomarkers in Cancer Staging, Prognosis and Treatment Selection. *Medscape Oncol.* **2017**.

(33) Goossens, N.; Nakagawa, S.; Sun, X.; Hoshida, Y. Cancer Biomarker Discovery and Validation. *Transl. Cancer Res.* **2015**, *4* (3), 256–269.

(34) Nelson, D. A.; Cox, M. M. Protein Structure. In *Lehninger Principles of Biochemistry*; W. H. Freeman and Company: New York, 2005; pp 178–182.

(35) Nimse, S. B.; Sonawane, M. D.; Song, K.-S.; Kim, T. Biomarker Detection Technologies and Future Directions. *Analyst* **2016**, *141* (3), 740–755.

(36) ELISAs and ELISA Kits: R&D Systems. R&D Systems Web Site. https:// www.rndsystems.com/products/elisas (accessed May 10, 2018).

(37) SimpleStep ELISA® kits: sensitive results in 90 minutes. Abcam Web Site. http://www.abcam.com/kits/simplestep-elisa-kits (accessed May 10, 2018).

(38) Automated Analyzers - ELISA - HUMAN Diagnostics Worldwide. Human Web Site. https://www.human.de/products/elisa/automated-analyzers/ (accessed May 10, 2018).

(39) Luminex® Assays and Luminex High Performance Assays: R&D Systems. R&D Systems Web Site. https://www.rndsystems.com/products/luminex-assays-and-high-performance-assays (accessed May 10, 2018).

(40) Multiplex immunoassays for flow cytometers | FirePlex. Abcam Web Site. http://www.abcam.com/nav/elisa-matched-antibody-pairs-and-multiplex-immunoassays/multiplex-immunoassays (accessed May 10, 2018).

(41) MESO QuickPlex SQ 120. Meso Scale Discovery Web Site. https://www.mesoscale.com/ en/products_and_services/instrumentation/quickplex_sq_120 (accessed May 10, 2018).

(42) ProteOn™ XPR36 Surface Plasmon Resonance (SPR) System | LSR. Bio-Rad Web Site. https://www.bio-rad.com/en-in/applications-technologies/proteon-xpr36-surface-plasmon-resonance-spr-system?ID=LUSM664EH (accessed May 10, 2018).

(43) Flow cytometry intracellular staining protocol. Abcam Web Site. http://www.abcam.com/protocols/flow-cytometry-intracellular-staining-protocol (accessed May 10, 2018).

(44) Gubala, V.; Harris, L. F.; Ricco, A. J.; Tan, M. X.; Williams, D. E. Point of Care Diagnostics: Status and Future. *Anal. Chem.* **2012**, *84* (2), 487–515.

(45) Krause, C. E.; Otieno, B. A.; Bishop, G. W.; Phadke, G.; Choquette, L.; Lalla, R. V.; Peterson, D. E.; Rusling, J. F. Ultrasensitive Microfluidic Array for Serum Pro-Inflammatory Cytokines and C-Reactive Protein to Assess Oral Mucositis Risk in Cancer Patients. *Anal. Bioanal. Chem.* **2015**, *407* (23), 7239–7243.

(46) Rusling, J. F.; Bishop, G. W.; Doan, N. M.; Papadimitrakopoulos, F. Nanomaterials and Biomaterials in Electrochemical Arrays for Protein Detection. *J. Mater. Chem. B* **2014**, *2* (1), 12–30.

(47) Freeman, R. G.; Grabar, K. C.; Allison, K. J.; Bright, Robin, M.; Davis, J. A.; Guthrie, A. P.; Hommer, M. B.; Jackson, M. A.; Smith, P. C.; Walter, D. G.; et al. Self-Assembled Metal Colloid Monolayers: An Approach to SERS Substrates. *Science* **1995**, *267* (5204), 1629–1632.

(48) Dequaire, M.; Degrand, C.; Limoges, B. An Electrochemical Metalloimmunoassay Based on a Colloidal Gold Label. *Anal. Chem.* **2000**, *72* (22), 5521–5528.

(49) Wang, J.; Liu, G.; Jan, M. R. Ultrasensitive Electrical Biosensing of Proteins and DNA: Carbon-Nanotube Derived Amplification of the Recognition and Transduction Events. *J. Am. Chem. Soc.* **2004**, *126* (10), 3010–3011.

(50) Jensen, G. C.; Krause, C. E.; Sotzing, G. A.; Rusling, J. F. Inkjet-Printed Gold Nanoparticle Electrochemical Arrays on Plastic. Application to Immunodetection of a Cancer Biomarker Protein. *Phys. Chem. Chem. Phys.* **2011**, *13* (11), 4888.

(51) Dixit, C. K.; Kadimisetty, K.; Otieno, B. A.; Tang, C.; Malla, S.; Krause, C. E.; Rusling, J. F. Electrochemistry-Based Approaches to Low Cost, High Sensitivity, Automated, Multiplexed Protein Immunoassays for Cancer Diagnostics. *Analyst* **2016**, *141* (2), 536–547.

(52) Yu, X.; Munge, B.; Patel, V.; Jensen, G.; Bhirde, A.; Gong, J. D.; Kim, S. N.; Gillespie, J.; Gutkind, J. S.; Papadimitrakopoulos, F.; et al. Carbon Nanotube Amplification Strategies for Highly Sensitive Immunodetection of Cancer Biomarkers. *J. Am. Chem. Soc.* **2006**, *128* (34), 11199–11205.

(53) Kim, S. N.; Rusling, J. F.; Papadimitrakopoulos, F. Carbon Nanotubes for Electronic and Electrochemical Detection of Biomolecules. *Adv. Mater.* **2007**, *19* (20), 3214–3228.

(54) Mani, V.; Chikkaveeraiah, B. V.; Patel, V.; Gutkind, J. S.; Rusling, J. F. Ultrasensitive

Immunosensor for Cancer Biomarker Proteins Using Gold Nanoparticle Film Electrodes and Multienzyme-Particle Amplification. *ACS Nano* **2009**, *3* (3), 585–594.

(55) Le, H. P. Progress and Trends in Ink-Jet Printing Technology. *J. Imaging Sci. Technol.* **1998**, *42* (1), 49–62.

(56) Zoltan, S. I. Pulsed Droplet Ejecting System. US3857049A, December 24, 1974.

(57) Vaught, J. L.; Cloutier, F. L.; Donald, D. K.; Meyer, J. D.; Tacklind, C. A.; Taub, H. H. Thermal Ink Jet Printer. US4490728A, December 25, 1984.

(58) Andresen, P.; Faubel, M.; Haeusler, D.; Kraft, G.; Luelf, H.-W.; Skofronick, J. G. Characteristics of a Piezoelectric Pulsed Nozzle Beam. *Rev. Sci. Instrum.* **1985**, *56* (11), 2038–2042.

(59) Sumerel, J.; Lewis, J.; Doraiswamy, A.; Deravi, L. F.; Sewell, S. L.; Gerdon, A. E.; Wright, D. W.; Narayan, R. J. Piezoelectric Ink Jet Processing of Materials for Medical and Biological Applications. *Biotechnol. J.* **2006**, *1* (9), 976–987.

(60) *The Chemistry of Inkjet Inks*; Magdasi, S., Ed.; World Scientific Publishing Company: Singapore, 2010.

(61) Pekarovicova, A.; Bhide, H.; Fleming, P. D.; Pekarovic, J. Phase-Change Inks. *J. Coatings Technol.* **2003**, *75* (936), 65–72.

(62) Hoth, C. N.; Schilinsky, P.; Choulis, S. A.; Brabec, C. J. Printing Highly Efficient Organic Solar Cells. *Nano Lett.* **2008**, *8* (9), 2806–2813.

(63) Bao, B.; Li, M.; Li, Y.; Jiang, J.; Gu, Z.; Zhang, X.; Jiang, L.; Song, Y. Patterning Fluorescent Quantum Dot Nanocomposites by Reactive Inkjet Printing. *Small* **2015**, *11* (14), 1649–1654.

(64) Ursan, I. D.; Chiu, L.; Pierce, A. Three-Dimensional Drug Printing: A Structured Review. *J. Am. Pharm. Assoc.* **2013**, *53* (2), 136–144.

(65) Lee, J.-Y.; Choi, B.; Wu, B.; Lee, M. Customized Biomimetic Scaffolds Created by Indirect Three-Dimensional Printing for Tissue Engineering. *Biofabrication* **2013**, *5* (4), 045003.

(66) Warnke, P. H.; Seitz, H.; Warnke, F.; Becker, S. T.; Sivananthan, S.; Sherry, E.; Liu, Q.; Wiltfang, J.; Douglas, T. Ceramic Scaffolds Produced by Computer-Assisted 3D Printing and Sintering: Characterization and Biocompatibility Investigations. *J. Biomed. Mater. Res. Part B Appl. Biomater.* **2010**, *93B* (1), 212–217.

(67) Yamada, T.; Matsuda, Y.; Yoshino, M.; Sakata, M. Micro-Dot Ink Jet Recorder. US4746928A, 1988.

(68) Kenyon, R. W. Ink Jet Printing. In *Chemistry and Technology of Printing and Imaging Systems*; Gregory, P., Ed.; Springer Netherlands: Amsterdam, 1996; pp 113–138.

(69) Kobayashi, H.; Koumura, N.; Ohno, S. Liquid Recording Medium. US4243994A, 1981.

(70) Buck, R. T.; Cloutier, F. L.; Erni, R. E.; Low, R. N.; Terry, F. D. Disposable Ink Jet Head. US4500895A, 1985.

(71) Stemme, N. Arrangement of Writing Mechanisms for Writing on Paper with a Colored Liquid. US3747120A, 1973.

(72) Kyser, E. L.; Sears, S. B. Method and Apparatus for Recording with Writing Fluids and Drop Projection Means Therefor. US3946398A, 1976.

(73) Elrod, S. A.; Hadimioglu, B.; Khuri-Yakub, B. T.; Rawson, E. G.; Richley, E.; Quate, C. F.; Mansour, N. N.; Lundgren, T. S. Nozzleless Droplet Formation with Focused Acoustic Beams. *J. Appl. Phys.* **1989**, *65* (9), 3441–3447.

(74) Kwon, J. W.; Kamal-Bahl, S.; Kim, E. S. In Situ DNA Synthesis on Glass Substrate for Microarray Fabrication Using Self-Focusing Acoustic Transducer. *IEEE Trans. Autom. Sci. Eng.* **2006**, *3* (2), 152–158.

(75) Silverbrook, K. Fax Machine with Concurrent Drop Selection and Drop Separation Ink Jet Printing. US5781202A, 1998.

(76) Lee, J.-G.; Cho, H.-J.; Huh, N.; Ko, C.; Lee, W.-C.; Jang, Y.-H.; Lee, B. S.; Kang, I. S.; Choi, J.-W. Electrohydrodynamic (EHD) Dispensing of Nanoliter DNA Droplets for Microarrays. *Biosens. Bioelectron.* **2006**, *21* (12), 2240–2247.

(77) Mueller, U.; Nyarsik, L.; Horn, M.; Rauth, H.; Przewieslik, T.; Saenger, W.; Lehrach, H.; Eickhoff, H. Development of a Technology for Automation and Miniaturization of Protein Crystallization. *J. Biotechnol.* **2001**, *85* (1), 7–14.

(78) Wallace, D. B. Automated Electronic Circuit Manufacturing Using Ink-Jet Technology. *J. Electron. Packag.* **1989**, *111* (2), 108–111.

(79) Hudd, A. Inkjet Printing Technologies. In *The Chemistry of Inkjet Inks*; Magdassi, S., Ed.; World Scientific: Singapore, 2009; pp 3–18.

(80) Mikalsen, A. Ink Jet Apparatus and Method Employing Phase Change Ink. US4742364A, November 26, 1988.

Chapter 2

Evaluation of Soluble L-Selectin in Bladder Cancer Patients Using a Microfluidic Bead-based Modified ELISA Assay

2.1 Abstract

A low-cost, sensitive bead-based electrochemical immunoarray is reported for soluble L-selectin (or CD62L protein), a potential biomarker for the staging of bladder cancer. A semi-automated modular microfluidic array is used with online antigen capture on superparamagnetic beads that are subsequently delivered to a detection chamber housing multiple sensors. The assay is designed to accurately detect CD62L in diluted serum with limit of detection (LOD) at 0.25 ng mL^{-1} and a dynamic range of 0.25 - 100 ng mL^{-1}. The microfluidic array gives significantly better accuracy and higher sensitivity than a standard ELISA kit, which is shown to be subject to signficiant systematic error in high and low concentration ranges. 41 serum samples, from patients with varying grades of bladder cancer and cancer-free controls, are analyzed by the immunoarray and ELISA and CD62L levels are correlated. This work establishes a new accurate assay for CD62L, and highlights the potential of this protein in serum as a biomarker for detection of locoregional progression of bladder cancer.

2.2 Introduction

2.2.1 Bladder cancer: Statistics and Stages

Bladder cancer arises from the urothelium, presenting as non-invasive disease in majority of patients (Figure 2.1). 2018 will see nearly 81,000 newly diagnosed cases and ~17,200 deaths from bladder cancer, according to the American Cancer Society.[1] Four times more prevalent in men than women, bladder cancer occurs at the median diagnosis age of 65 years.[1] Bladder cancer tumors are categorized as high- or low-grade tumors, both having a high risk of recurrence. High-grade tumors additionally have a higher risk of invading the muscle wall of the bladder, spreading to distant organ sites, and progressing to late stage cancer, thus dramatically varying

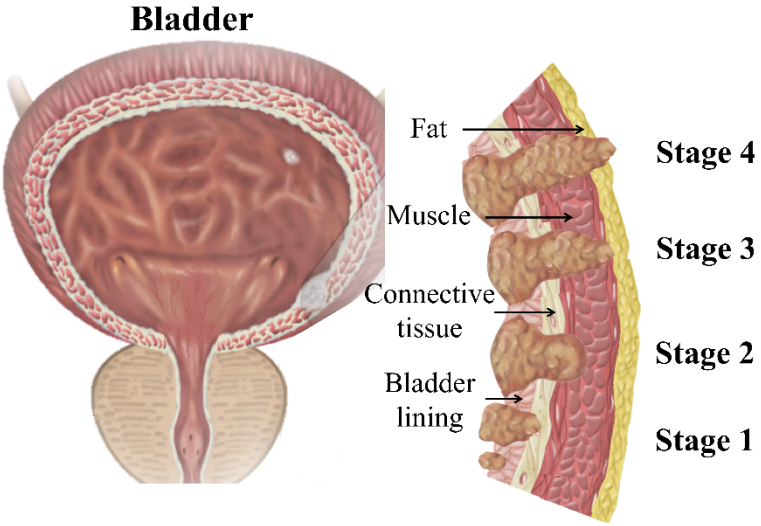

Figure 2.1: Bladder cancer presents at the urothelium of human bladder. Staging of the disease is based on tumor growth from the bladder lining outwards into the muscle wall and beyond. (*Figure adapted from reference 2*)

five-year survival rates with stage of disease. In more than 70% of patients, bladder cancer will reoccur within 2 years of remission,[3] making long-term monitoring with non-invasive biomarker test key to improving patient outcomes.

Bladder cancer is staged based on growth of the tumor into wall of the bladder, as shown in Figure 2.1.[4] At stage 1, the tumor may be present in the bladder lining and the connective tissue, without breaching into the muscle layer. As the tumor grows into the muscle layer of the bladder, the tumor is classified as stage 2. Stage 3 indicates the cancer has grown into the fatty tissue, the prostate, uterus or vagina, and local lymph nodes. At stage 4, cancer may have gown into the pelvis or abdominal wall, nearby organs, or even fully metastasized to local and distant lymph nodes. Non-invasive tumors (stage 1 and 2) have five year survival of ~88% whereas locally advanced/metastatic disease have a poorer prognosis with only a 6% survival rate.[5,6] While about 50% tumors are detected at stage 1, the low outcomes at later stages highlight the need for diagnostic molecular tests. Tumor biomarkers are not yet clinically employed for determination of a patient's progression, prognosis or treatment, and there are no molecular forecasters for high grade disease or metastatic potential in bladder cancer cases.[1,7,8]

2.2.2 Current Detection Strategies

Currently, Bladder cancer is detected with a combination non-invasive and invasive test: They include urinalysis, voided urine cytology (VUC), cystoscopy, biopsy, biomarker tests, and imaging studies, Figure 2.2.[9] The efficiency of such tests varies greatly based on knowledge of patient habits and their risk of developing bladder cancer. At present, no routine screening test is available for bladder cancer. Early detection of bladder cancer is often due to appearance of physiological symptom, such as passing of blood in urine, unusual bladder activity, pain during

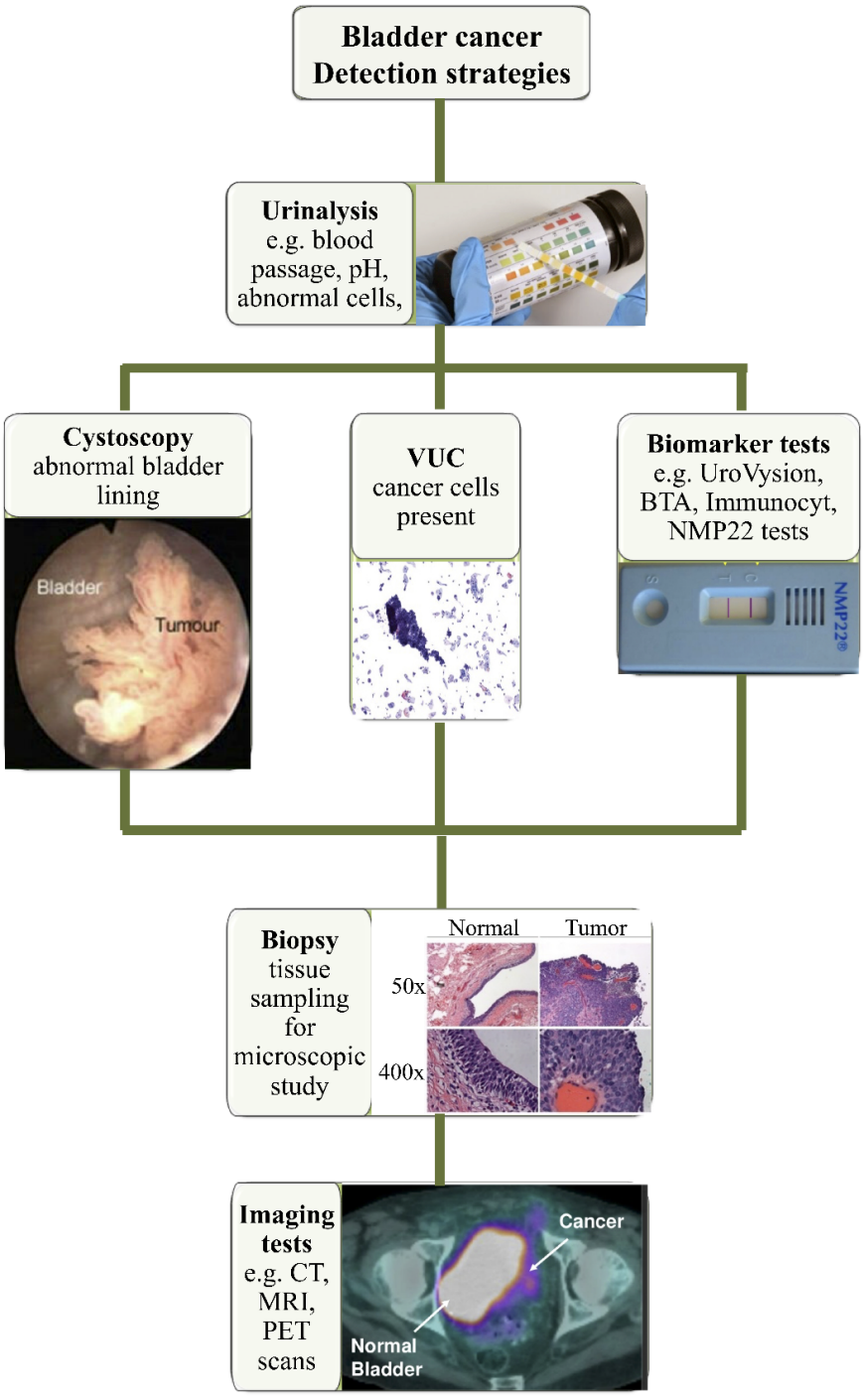

Figure 2.2: Detection strategies for bladder cancer. Early detection tools include urinalysis, voided urine cytology (VUC), cystoscopy, and biomarker test, such as UroVysion^{TM}, NMP22, etc. Biopsy and imaging tests are used to confirm and stage the disease.

urination, etc. Urinalysis, a common screening test, can check for any abnormal physical or biochemical urine characteristics, such as pH, elevated cell count, blood composition in urine, etc.[10] The test strips provide only qualitative measure of anomalies in urine (Figure 2.2). Although non-invasive and easily accessible, such changes in urine can also result from infections or other health conditions; thus urinalysis is not used as a routine screening test for bladder cancer.

If bladder cancer is suspected from urinalysis — due to risk factors in patients that include birth defects, chemical exposure, or previous occurrence of cancer — VUC and cystoscopy are performed. VUC is a non-invasive test that microscopically examines urine for the presence of possible cancer cells, such as clumps of cells seen in Figure 2.2. Early stage and low-grade tumors rarely shed cancer cells into the urine, limiting VUC to detection of primarily high-grade, late stage tumors.[9] Nevertheless, VUC is a high accuracy, non-invasive confirmatory test for bladder cancer.

In cystoscopic procedures, a cystoscope, a thin hollow tube with a camera, is inserted into the bladder to visually examine lining of the bladder and the urethra for anomalies (Figure 2.2). Skill level and cost (due to anesthesia) are at times prohibitive factors in successful detection of bladder cancer. Due to high risk of recurrence, bladder cancer patients undergo checkups quarterly in the first two years of remission and thereafter semi-annually, making patient discomfort particular disadvantageous to the use of this invasive procedure. On observing abnormal cell lining during cystoscopy, the physician will collect samples for biopsy. As with any cancer biopsy, results may be conclusive and confirmatory or inconclusive due to tissue heterogeneity and skill of the physician in recognizing abnormal bladder lining.[9,11,12] In case of

bladder cancer, biopsy is also used to assess spread of cancer and its grade, i.e. low- or high-grade.

FDA has additionally approved multiple POC devices and biomarker tests for bladder cancer; these include UroVysion™, bladder tumor associated antigen (BTA) test, Immunocyt, NMP22 (BladderChek®).[10] UroVysion™, manufactured by Abbott molecular, is a urine-based genetic biomarker test that uses fluorescence to detect aneuploidy, an unusual number of chromosomes in cells, in certain chromosomes.[13] Although with low false negative rate, similar to VUC this test can only detect cancer if minimum threshold of cells are present in urine and only if cancer is present with the target genetic changes. BTA test is a single step lateral flow device based on colorimetric detection of tumor-associated antigen hCFHrp (human complement factor H-related protein). The test has moderate specificity at 50 - 85%, however has a high false positive rate lowering its predictive value to < 20%.[14] Immunocyt™ (DiagnoCure Inc., Canada) is a fluorescence biomarker test measuring two mucin-like antigens and carcinoembryonic antigen. Immunocyt has low positive predictive value at 26%, but researchers have suggested delaying cystoscopy based on negative Immunocyt results due to the high negative predictive value of 93% observed.[15] NMP22 antigen test is available as ELISA kit or as POC device BladderChek® (Abbott), and assays nuclear mitotic apparatus protein 1 (NUMA1) with sensitivity and specificity at 56% and 88% respectively.[16] Like Immunocyt, negative NMP22 test has been used to delay cystoscopy in patients with recurring bladder cancer.

All biomarker tests have a low false-negative rate and are thus used primarily to confirm absence of cancer in patients in remission or those with recurring tumors. Nevertheless, in monitoring new and surviving patients, these tests cannot stage and grade bladder cancer tumors. Imaging techniques, which include computed tomography (CT scan), magnetic resonance

imaging (MRI), and positron emission tomography (PET scan) are principal tests for staging and grading tumors.[9] A CT scan takes X-ray images, after a contrast dye is injected into the patient, to recreate 3-dimensional images of tumors in the bladder or at lymph nodes (in case of metastasis). MRI, much like CT scan, uses a specialized contrast medium with magnetic fields for imaging tumors or enhanced lymph nodes. PET scans, used in isolation or with CT scans, image tumors after injection of a radioactive dye. The dye is selectively absorbed by cancer cells, providing much cleaner images; early indications suggest it may be more effective in assessing spread of bladder cancer than CT or MRI scans. Additionally, ultrasound — a technique that uses sounds waves without a contrast dye — can be employed to detect spread of bladder cancer to kidneys and rest of the urinary tract. Doctor's skill in staging and grading tumors from these images is perhaps critical to patient outcomes as survival rates decline rapidly in late stage bladder cancer.

2.2.3 Microfluidic System for Electrochemical Immunoassay

We have developed high sensitivity microfluidic protein immunoassays (also referred to as "immunoarray") with modular semi-automated microfluidics and labeled detection beads.[17] Our microfluidic system (Figure 2.3A) consists of low-cost in-house reaction chamber (Figure 2.3B) and detection chamber (Figure 2.3C), assembled downstream from a pump, injector, and switching valves.[18] The pump drives the flow for the entire system, usually at flow rates of 0.1 - 1 mL min^{-1}. The injector delivers 100 μL of magnetic beads, analyte samples, and sensing solution by manual injection. Switching valves allow control over directionality of flow, either to reaction chamber alone, detection chamber alone, or to the reaction chamber and

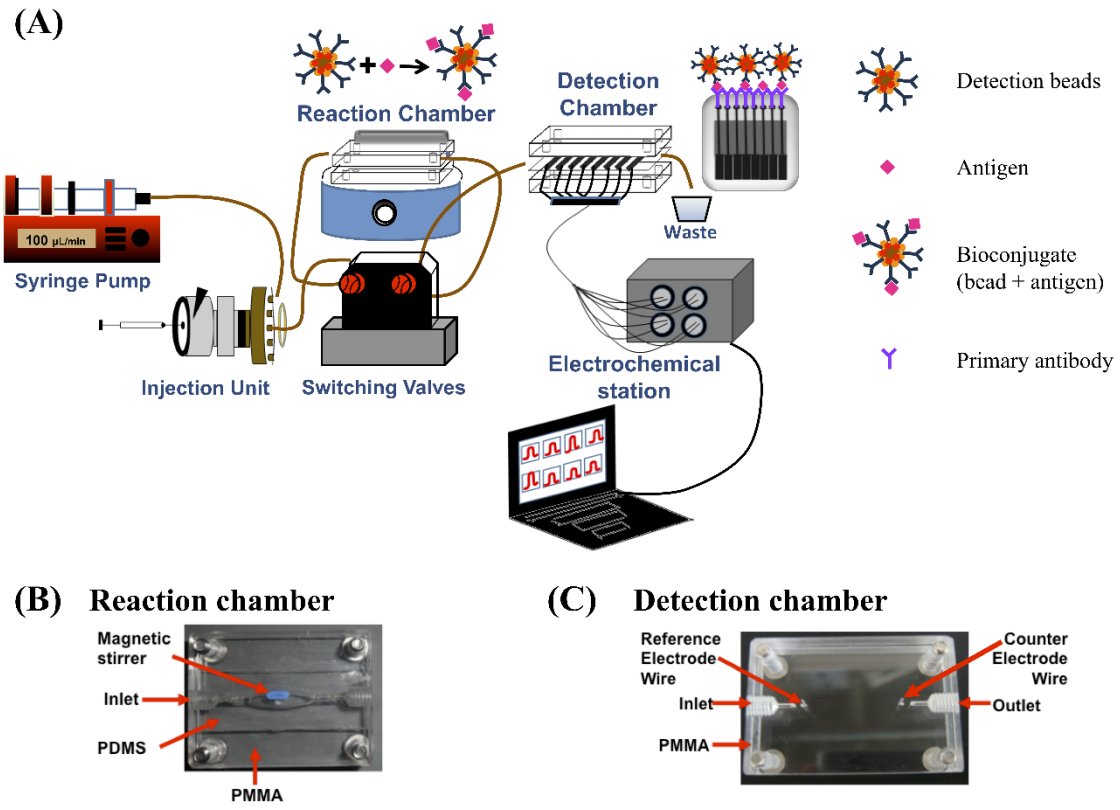

Figure 2.3: An in-house microfluidic system (A) for electrochemical immunoarray consisting of a pump, injector, switching valves, reaction chamber (B), and a detection chamber (C). The antigen and detection beads are stirred in reaction chamber (B) for incubation of antigen and detection antibodies. The electrodes, on which the immunoassay is completed by incubation with primary antibodies, are housed in the detection chamber (C) and connected to an electrochemical station and a computer for data capture and analysis.

detection chamber in a sequence. PEEK tubings and leuers complete all fluidic connections between the various components.

The reaction and detection chamber are fabricated by casing a molded poly(dimethylsiloxane) (PDMS) channel between two poly(dimethylmethacrylate) (PMMA) or polycarbonate plates. The PDMS channels regulate the volume of each chamber and provide a leak-proof channel. The reaction chamber has an oval PDMS channel (~ 100 μL in volume) that contains a magnetic stir bar. The top PMMA plate of reaction chamber has two machined openings for an inlet and an outlet (Figure 2.3B); the bottom PMMA plate provides a flat support surface to the assembly. The reaction cell sits atop a magnetic stirrer allowing stirring of contained solution during the immunoarray. In our protocol, magnetic beads (MB) are first injected into the system and captured in the reaction chamber while holding a magnet on top of the chamber (Figure 2.3A). The analytical sample is then injected and flow is stopped as the sample reaches the chamber. The two are then stirred for a fixed amount of time to facilitate the reaction between detection beads and the antigen (Ag).

The detection chamber has a narrow rectangular PDMS channel (~ 60 μL) that can encase the 8-electrode reaction spots. Like the reaction chamber, the detection chamber's top plate also has an inlet and outlet for the flow. Additionally, the plate has grooves on either side of the inlet and outlet line housing a silver/silver chloride (Ag/AgCl) reference electrode and platinum (Pt) counter electrode (Figure 2.3C), such that these lie above and below the 8-electrode sensor reaction spots. The reacted solution is transferred from the reaction chamber to the detection chamber, where the immunoarray is completed and electrochemical detection is performed.

2.2.4 Scope of Current Research

Recent research has been directed at understanding the biological process involved in cancer progression to improve targeted and personalized therapy. Several molecules from the lymphatic system are being studied for correlation with metastasis in cancer cases.[19–21] Selectins, a class of mammalian vascular adhesion molecules, are some of such biomolecules.[22–27] Specifically, L-selectin (or CD62L), expressed on a variety of inflammatory cells, plays a crucial role in migration and homing of lymphocytes to lymph nodes.[28–30] A previous study shows a marked increase in gene and cellular expression of L-selectin in muscle-invasive high-grade bladder cancer tumors in cell lines and in human tissues, and suggests a potential role of CD62L as a biomarker for metastatic bladder cancer.[7] A more sensitive and accurate technique than standard enzyme-linked Immunosorbent assay (ELISA) for serum protein quantification could lead to better diagnoses to direct treatment plans.

Our approach utilizes magnetic beads massively labeled with detection antibodies (Ab_2) and horseradish peroxidase (HRP) capture target proteins (i.e. detection beads) that are delivered to an amperometric sandwich immunoassay detection chip, providing a fast, low-cost alternative to ELISA and other commercial protein tests.[31–33] Versatility and accuracy of this approach has been demonstrated by ultrasensitive multiplexed detection of cytokines,[17,18,34] prostate specific antigen (PSA),[35] and other protein and peptide biomarkers[36–38] at fg mL^{-1} levels in human serum. In this chapter, an adaptation of this immunoarray is presented, wherein the number of HRP enzyme labels on the magnetic bead bioconjugate are optimized to measure circulating CD62L protein at clinically relevant levels. Limit of detection (LOD) is obtained at 0.25 ng mL^{-1} and excellent sensitivity with log-linear dynamic range of four orders of magnitude is seen in the

pg mL^{-1} to ng mL^{-1} range for CD62L. Accuracy is demonstrated by multiple validation experiments, and serum samples from cancer-free and bladder cancer patients are analyzed. The immunoarray is observed to be more sensitive and accurate than a standard CD62L ELISA kit, and serious systematic errors in the latter approach are identified. Preliminary results suggest that the microfluidic serum immunoarray can differentiate between cancer-free and bladder cancer patients (diagnostic sensitivity = 93.6%, specificity = 100%) and between patients with low-grade and high-grade lesions (sensitivity = 90%, specificity = 91%).

2.3 Experimental

2.3.1 Chemicals and Instruments

Screen-printed 8-electrode carbon array (700 μm diameter) sensors are purchased from Kanichi Research Services Ltd (Manchester, England). L-glutathione reduced (GSH, ≥98%), gold (III) chloride trihydrate ($HAuCl_4 \cdot 3H_2O$, ≥99.9%), sodium borohydride ($NaBH_4$, 99%), poly(diallydimethylammonium chloride) (PDDA, MW 200,000-300,000, 20% in water), 1-(3-(dimethylamino)propyl)-3-ethylcarbodiimide hydrochloride (EDC), N-hydroxysulfosuccinimide (NHSS), bovine serum albumin (BSA), calf serum, Tween-20, sodium chloride (NaCl), potassium chloride (KCl), sodium phosphate dibasic (Na_2HPO_4, ≥98%), sodium phosphate monobasic monohydrate ($NaH_2PO_4 \cdot 3H_2O$, ≥98%), hydroquinone (HQ, ≥99%), hydrogen peroxide (H_2O_2, 30%) are purchased from Sigma-Aldrich (St. Louis, MO, USA). The polydimethylsiloxane (PDMS) kit is obtained from Dow Corning (Auburn, MI, USA). Streptavidin-coated superparamagnetic beads (MP, 1 μm Dynabeads) and biotinylated horseradish peroxidase (HRP, 2.5 mg mL^{-1}) are purchased from Life Technologies (Carlsbad,

CA, USA). All solutions are prepared using 18 MΩ·cm water purified by passing house-distilled water through a Hydro Service and Supplies purification system (Durham, NC, USA).

Monoclonal anti-human L-Selectin (CD62L) antibody (Ab_1, Catalog Number: BBA24, Clone: 4G8), biotinylated anti-human L-Selectin antibody (Ab_2, Catalog Number: BAF728), recombinant human L-Selectin/CD62L protein antigen (Ag, Catalog Number: ADP2), and Human sL-Selectin/CD62L ELISA kit (Catalog Number: BBE4B) are purchased from R&D Systems (Minneapolis, MN, USA). Human serum samples are collected from patients at the University of Connecticut Health Center (UCHC). Upon approval from the IRB and Written Informed Consent from patients, sample collection is completed. All samples are stored at or below -80°C until use. Absorbances are measured for each assay experiment using FlexStation 3 multi-mode microplate reader (Molecular Devices, Sunnyvale, CA, USA). CHI 1040C multipotentiostat electrochemical workstation (Austin, TX, USA) is used for 8-channel amperometric detection.

2.3.2 Fabrication of Immunoarray Sensor

Screen-printed 8-electrode carbon array sensors are fabricated with layer-by-layer (LBL) assembly as previously described. Briefly, arrays are coated with successive layers of polycation PDDA and negatively charged 5 nm glutathione-coated gold nanoparticles (GSH-AuNPs) using LBL electrostatic adsorption for 20 min each as previously reported and as illustrated in Figure 2.4. Incubating a freshly prepared crosslinking solution of EDC and NHSS for 10 min activates terminal surface carboxyl groups on the GSH-AuNP layer. The electrode sensor arrays are subsequently spotted with primary or capture antibody (Ab_1), which is allowed to incubate overnight at 4°C resulting in Ab_1 immobilization via an amidization reaction, Figure 2.4.

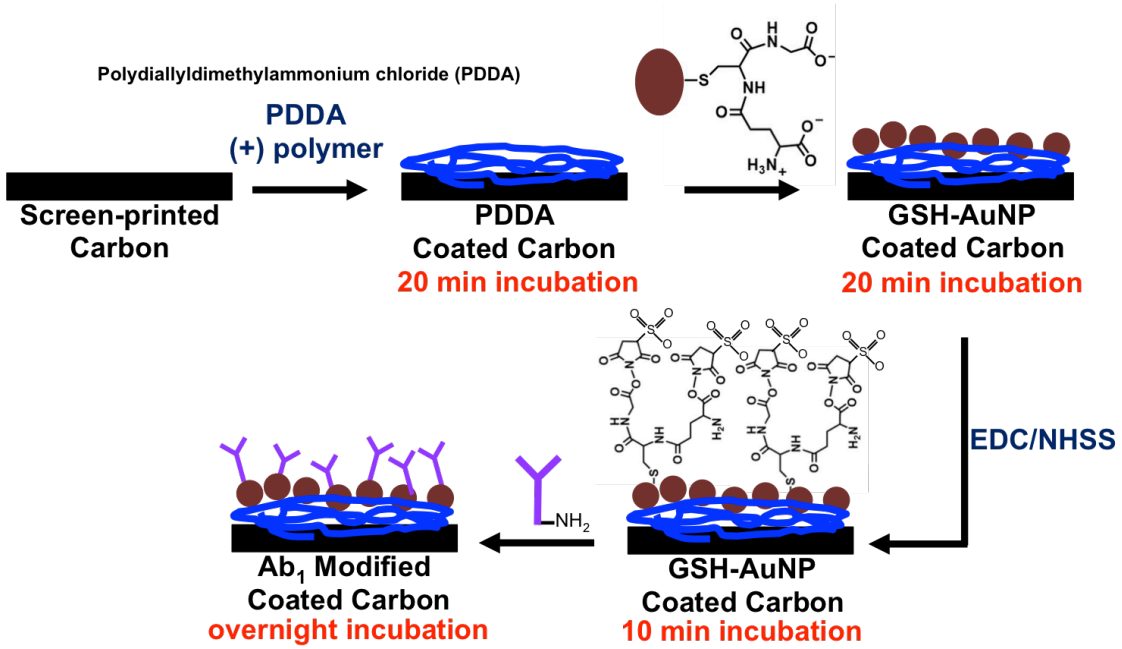

Figure 2.4: Protocol for layer-by-layer assembly introducing capture antibodies on electrode surface. Initial layers of PDDA, glutathione gold nanoparticles are coated by physical absorption. The antibodies are then covalently bound to the carboxyl groups on gold nanoparticles by carbodiimide chemistry using EDC/ NHSS.

Furthermore, prior to utilizing, the arrays are blocked with 2% BSA in PBS for 1 hr at 4°C to inhibit non-specific binding (NSB).

2.3.3 Preparation of Bioconjugates

A previous protocol is implemented for the attachment of numerous biotin-Ab_2 and biotin-HRP labels to 1 µm diameter streptavidin-coated superparamagnetic beads (MPs, 10 mg mL^{-1}), as seen in Figure 2.5. Briefly, MPs are magnetically separated using an Invitrogen DynaMag spin magnet and subsequently washed with PBS pH 7.4 three separate times. Then

simultaneously biotin-Ab_2 and biotin-HRP are added into the MP dispersion containing 0.1% BSA in PBS pH 7.4 at a ratio of 1:2:4:4 (MP:Ab_2:HRP:BSA) followed by incubation at 37°C for 30 min. After conjugation, the bead bioconjugate (MP-Ab_2-HRP, Figure 2.5) dispersion is magnetically separated and washed three distinct times with 0.1% BSA in PBS pH 7.4 to remove any excess Ab_2 and HRP. Lastly, the bioconjugate is reconstituted with 0.1% BSA in PBS pH 7.4 and stored at 4°C until needed. Once optimized concentrations of both Ab_2 and HRP

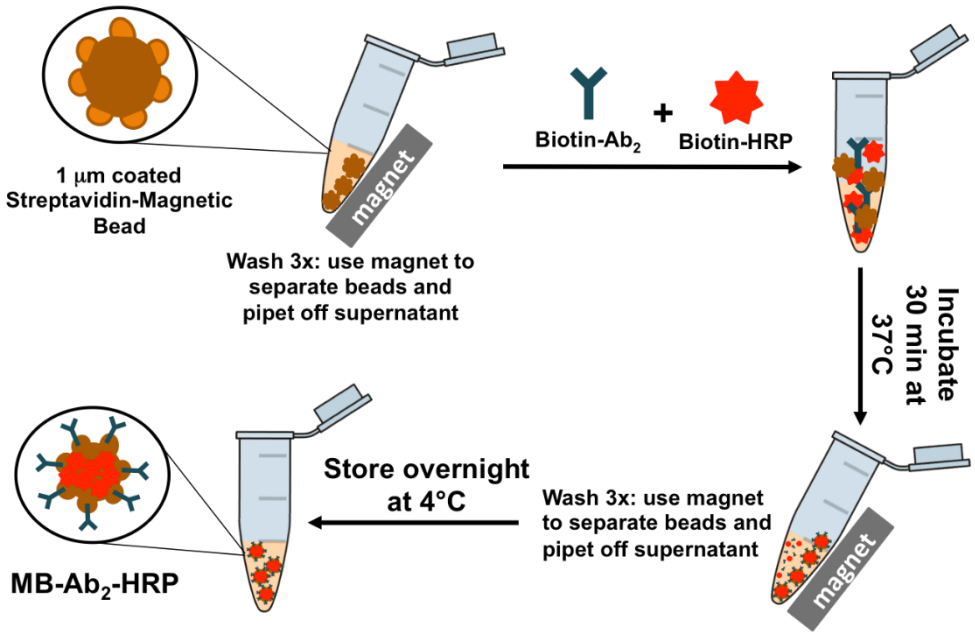

Figure 2.5: MB-Ab_2-HRP bioconjugates, used as the detection assembly, are prepared by incubating washed streptavidin coated superparamagnetic beads with biotin-Ab_2 and biotin-HRP with 0.1% BSA in PBS buffer in 1:2:4:4 ratio. After 30 minute incubation at 37°C, the beads are washed and stored in 0.1% BSA in PBS at 4°C until used.

are determined, characterization assays are completed. Specifically, bioconjugate particles originally had 3,200 (± 300) Ab_2 per MP and 10,000 (± 500) HRP per MP. After optimization for higher dynamic range, new concentrations used are 0.5 mg mL^{-1} HRP, 100 mg mL^{-1} Ab_1, and 10 mg mL^{-1} Ab_2 (Figure 2.6). The new bioconjugate had on average 2,100 (± 200) Ab_2 per MP and 5,000 (± 400) HRP per MP labels, as measured by bicinchoninic acid assay (BCA) kit (Thermo Scientific, Rockland, IL, USA)[39] and 2,2'-azino-bis(3-ethylbenzthiazoine-6-sulfonic acid) (ABTS) end-point assay (Sigma Aldrich, St. Louis, MO, USA)[40]. Absorbances are measured for each assay experiment using FlexStation 3 multi-mode microplate reader (Molecular Devices, Sunnyvale, CA, USA).

2.3.4 On-line Capture and Detection Protocol

An established modular on-line protein capture microfluidic system is employed, as shown in Figure 2.3A; this system provides a semi-automated methodology for protein detection. Previously published immunoarray procedure is used. Briefly, the system is first subjected to a flow of water followed by PBS-Tween 20. The detergent solution is used to minimize adhesion and NSB of undesirable molecules. Once the fluidic system is washed, 50 µL of bioconjugate (MP-Ab_2-HRP) is added to 150 µL of 20 mM PBS pH 7.4. This bioconjugate dispersion is then loaded into a 100 µL sample loop, injected at 100 µL min^{-1}, and allowed to fill the capture chamber. Next, protein Ag (standard or patient sample) in diluted calf serum is loaded and then injected into the capture chamber. Once the capture chamber is filled, stirring within the chamber is allowed for 30 min to facilitate protein capture (Figure 2.3A). Throughout both sequentially injections, a magnet bar is held atop the capture chamber to ensure MP-Ab_2-HRP are captured.

After the 30 min incubation period, resultant protein Ag-MP-Ab_2-HRP bioconjugates are transferred to the detection chamber, which houses a CD62L Ab_1 modified 8-electrode immunoarray, by switching the valves in the proper direction and pumping PBS-Tween 20 at 100 μL min^{-1} carrying the protein Ag-MP-Ab_2-HRP into the detection chamber. The flow is stopped once the red-brown color of MPs filled the entire channel; this provides an indication the transfer process is complete. Bioconjugates incubated at the electrode surfaces for 15 min to allow efficient capturing and completion of the immunoarray sandwich, Figure 2.3A). PBS-Tween 20 flow is resumed to remove any unbound bioconjugates followed by further washing with hydroquinone (HQ) for production of an electrochemical background signal. Amperometric detection is completed at -0.2 V vs. Ag/AgCl by injecting a sensing solution of 1 mM HQ mediator and 0.1 mM hydrogen peroxide (H_2O_2) at 100 μL min^{-1} into the detection chamber via the sample loop to activate the HRP labels on the bioconjugates. Prior to detection, the 8-electrode sensor array, platinum (Pt) counter, and Ag/AgCl reference are connected to a CHI 1040BC multipotentiostat (Figure 2.3A). An electrochemical redox-cycle yields amperometric current signals proportional to concentration of protein analyte (see Scheme 1.1). Once electrochemical detection is complete, a fresh modified 8-electrode array is inserted into the detection chamber for incubation of the next sample, which is undergoing protein capture during prior detection.

2.3.5 Optimization of Enzyme Label

Enzyme labels densely attached onto MP bioconjugates are optimized prior to finalizing CD62L protein antibody concentrations. This critical optimization step permits extension of the dynamic range from pg mL^{-1} to ng mL^{-1}. In particular, four different sets of MPs with varying

concentrations of biotin-HRP labels, specifically 0.25, 0.5, 1.25 and 2.5 mg mL^{-1}, and a constant concentration of Ab_2 are prepared. Following preparation, assays are performed by injection of a control (0 ng mL^{-1}), low (1 ng mL^{-1}), and high (10 ng mL^{-1}) antigen sample for each respective biotin–HRP concentration. As observed in Figure 2.6A, 0.5 mg mL^{-1} biotin–HRP provides the greatest signal difference between low and high concentrations; therefore, 0.5 mg mL^{-1} is utilized for further optimization processes and attainment of the standard calibration curve.

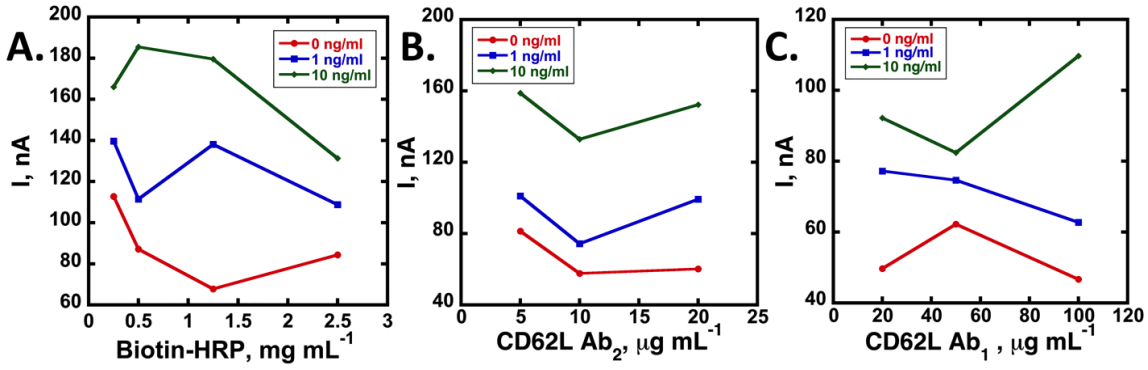

Figure 2.6: Optimization results for CD62L sandwich immunoarray performance upon employing standard concentrations of 0, 1 and 10 ng mL^{-1}. (A) Optimization of Biotin-HRP using consistent Ab_1 and Ab_2 concentrations. Optimal concentration of biotin-HRP is determined to be 0.5 mg mL^{-1}. (B) Optimized result for secondary antibody (Ab_2) using consistent Ab_1 and biotin-HRP label concentrations. Optimal concentration of Ab_2 is determined to be 10 mg mL^{-1} and (C) Optimized outcome for primary antibody (Ab_1) using consistent Ab_2 and biotin-HRP label concentrations. Optimal concentration of Ab_1 is determined to be 100 mg mL^{-1}.

2.3.6 Optimization of Antibodies for Protein CD62L

In addition to enzyme label, the capture antibody (Ab_1) and detection antibody (Ab_2) bound on the immunoarray platform and MP bioconjugate respectively are optimized to achieve maximum signal sensitivity prior to execution of a standard calibration curve. First, the detection antibody is optimized. In particular, the concentration of HRP and Ab_1 are kept constant and MP bioconjugates are prepared with three different Ab_2 concentrations, specifically 5, 10 and 20 μg mL^{-1}. Subsequently, assays are performed by injection of a control (0 ng mL^{-1}), low (1 ng mL^{-1}), and high (10 ng mL^{-1}) antigen sample for each respective bioconjugate concentration and amperometric current signals are compared. The optimum concentration of 10 μg mL^{-1} Ab_2 is selected, as shown in Figure 2.6B.

The concentration of the primary antibody is crucial as this improves assay sensitivity and minimizes NSB. Therefore, arrays with varying concentrations of Ab_1, specifically 5, 20, and 100 μg mL^{-1}, are prepared and the immunoassay is completed by the aforementioned procedure. During this Ab_1 optimization process, Ab_2 and biotin–HRP concentrations are kept constant. After comparison between each of the amperometric current signals, 100 μg mL^{-1} Ab_1 is selected and employed as the optimum concentration, as indicated in Figure 2.6C. Therefore, the best immunoarray performance is obtained when 100 μg mL^{-1} Ab_1 is bound on the sensor surface, while 10 μg mL^{-1} Ab_2 and 0.5 mg mL^{-1} biotin–HRP are attached to the MP bioconjugates. These conditions are employed for all latter experiments.

2.3.7 Patient Sample Analysis and Data Processing

After method optimization and accuracy validation, 41 serum samples from pateints with varying stages and grades of cancer are analyzed using the immunoarray procedure detailed above as well as ELISA kit BBE4B from R&D Systems. Samples (5 μL) are diluted 100-fold in PBS (pH 7.4) to bring CD62L levels into the dynamic range of the assay. Statistical analyses including box plots and receiver operating characteristic (ROC) analyses are done using MedCalc software.

2.4 Results

2.4.1 Optimization of Dynamic Range

Soluble CD62L protein in human serum is previously reported at 0-700 ng mL^{-1} in cancer-free control subjects, and at 500-2000 ng mL^{-1} in lymphoma patients based on results from standard ELISA. For the bead-based microfluidic immunoassay, a standard calibration curve for protein CD62L is first prepared under conditions for highest sensitivity using 3,200 (±300) Ab_2 and 10,000 (±500) HRP per MP. Typical amperometric peaks (Figure 2.7A) under these conditions give a semi-log calibration plot with dynamic range of 4.9 to 625 pg mL^{-1} (Figure 2.7B).

Although high sensitivity is achieved (slope 61.3 ± 4.8 nA log[CD62L, pg mL-1])$^{-1}$), patient sample dilutions of >10,000-fold are needed to remain within the dynamic range which could lead to serial dilution errors. To avoid high dilution, we decrease the number of HRP labels on the magentic beads. Biotin-HRP concentration during attachment to the beads is decreased five-fold to give 2,100 (±200) Ab_2 and 5,000 (±400) HRP per MP. The calibration for

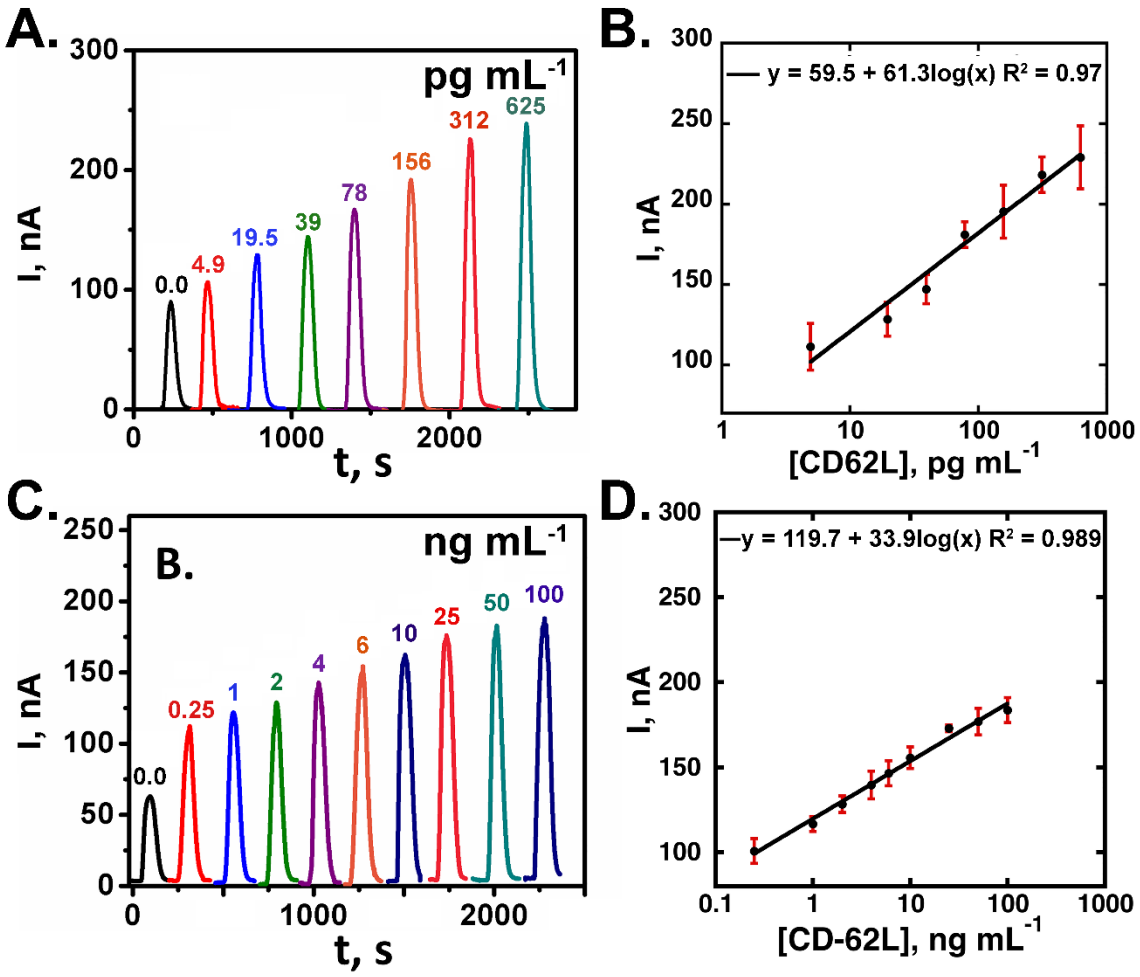

Figure 2.7: Calibrations using protein CD62L standards in 5-fold diluted calf serum with amperometric detection using 1 mM HQ and 0.1 mM H_2O_2 at -0.2 V vs. Ag/AgCl. (A) High sensitivity calibration peaks and (B) Calibration graph with dynamic range from 0.25 ng mL^{-1} to 100 ng mL^{-1}. (C) Calibration peaks for assay adapted to clinical range and (D) Calibration graph with a dynamic range from 4.9 pg mL^{-1} to 625 pg mL^{-1}.

these conditions is established in the ng mL^{-1} range, with detection limit 0.25 ng mL^{-1}. The log-linear dynamic range extended to 100 ng mL^{-1} (Figure 2.7C-D). Good reproducibility is signified by small error bars (n=8). Furthermore, excellent sensitivity with slope of calibration plot at 33.9 nA ± 1.3 (log[CD62L], ng mL^{-1})$^{-1}$ and $R^2 \geq 0.98$, as revealed in Figure 2.7D, are achieved in 30 min assays. The calibration is observed to be reproducible day-to-day with good agreement in both slope (≤ 8 %) and y-intercept (≤ 15 %), as seen in Figure 2.8.

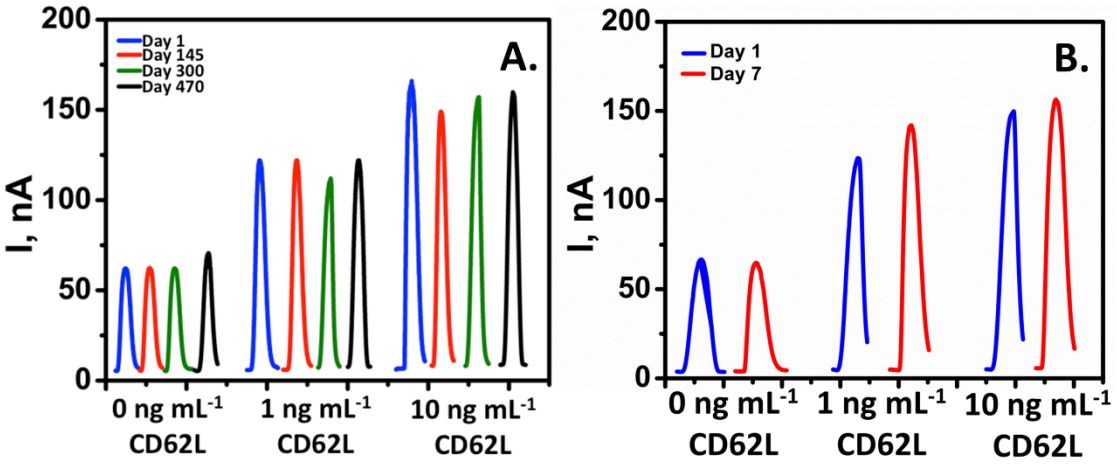

Figure 2.8: Amperometric signals to demonstrate assay reliability and stability. (A) Current signals from four independent days for 0, 1, and 10 ng mL^{-1} CD62L. (B) Comparison of current signals indicating stability of surface bound Ab_1 on the LBL sensor array over duration of one week for 0, 1, and 10 ng mL^{-1} CD62L.

2.4.2 Assay Validation using Spiked Calf Serum Samples

Serum is spiked with different concentrations of pure CD62L and analyzed for validating accuracy of the immunoarray. Since human serum contained high levels of indigenous protein CD62L, calf serum is consequently used as a surrogate. Calf serum is spiked at 75, 250, 350, 550, 700, 1500, 3000 and 5500 ng mL^{-1} and diluted 100-fold with PBS pH 7.4 prior before assays to replicate the patient sample protocol. The recovery amongst the eight spiked samples is within 83–116% for the immunoarray system (Figure 2.9A-B), which falls within acceptable analytical limits. However, ELISA yields varying concentration-dependent recoveries within 37–97%, as displayed in Figure 2.9A-B. With spiked levels as true values, these data show that the immunoarray method provides good accuracy in the 75-5500 ng/mL range, but that the ELISA kit has large errors above 1500 ng/mL and below 350 ng/mL CD62L.

Correlation plots show that ELISA recovery vs. true spiked levels yields a slope of 0.45 ± 0.03 (Figure 2.9C), well below the perfect correlation slope of 1, suggesting a general underestimation of CD62L by ELISA. For immunoarray results vs. true spiked levels (Figure 2.9D), a slope of 1.01 ± 0.02 with y-intercept at 0.13 ± 0.47 is found indicating excellent correlation with the actual CD62L levels and confirming accuracy of the assay.

Further statistical treatment confirms this bias in ELISA kit. A one sample mean t-test is performed for individual spiking levels, for each detection method.[41] Lower and upper concentration limits at 95% CI are calculated for individual recovery levels, as shown in Table 2.1. The detection method under consideration is accurate if the corresponding true spiked level is within the calculated range (For example, 75 ng mL^{-1} lies within the limits of 53.26 - 97.44). This test is also performed at 90% CI and yielded similar results (data not shown).

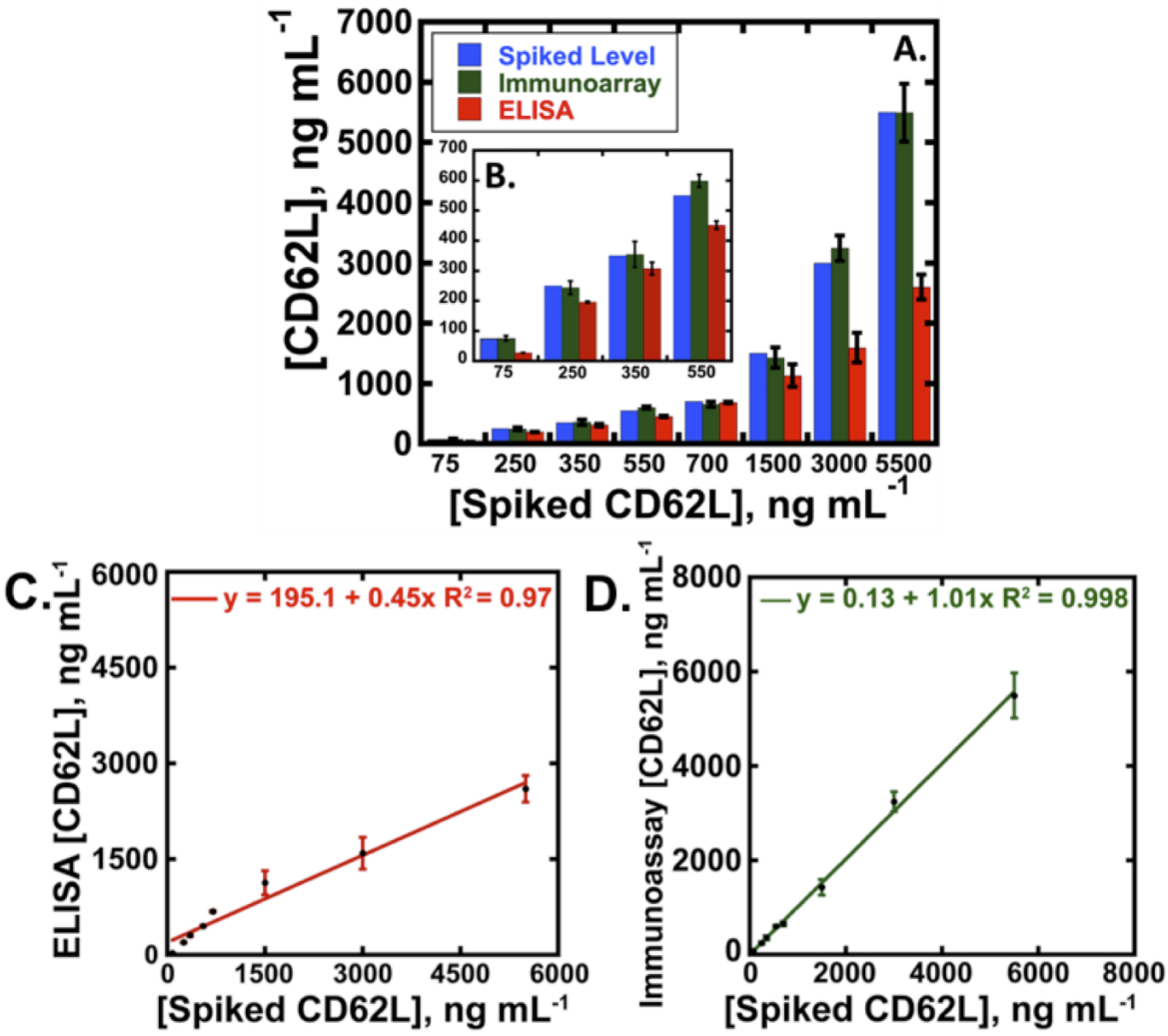

Figure 2.9: (A) Comparison of Immunoarray and ELISA results with known spiked levels of CD62L standards in calf serum, at 75, 250, 350, 550, 700, 1500, 3000, and 5500 ng mL^{-1}. Recovery is observed to be within 83%–116% for the Immunoarray and 37–97% for standard ELISA. (B) Zoomed inset for spiking levels 75 to 550 ng mL^{-1}. Correlation plots for (C) ELISA and (D) Immunoarray vs. spiking CD62L level showed immunoarray (slope = 1.01) is more accurate than ELISA (slope = 0.45). ELISA underestimates concentration above 1500 ng mL^{-1} and less than 550 ng mL^{-1}.

Spiking level (ng mL-1)	Immunoarray		ELISA		Two sample mean t-test at 95% CI*
	Calculated conc. range (ng mL-1)	t-test at 95% CI	Calculated conc. Range (ng mL-1)	t-test at 95% CI	
75	53.26 – 97.44	no diff.	18.95 – 35.97	**Sig. diff.**	**Sig. diff.**
250	201.1 – 304.8	no diff.	169.7 – 221.9	**Sig. diff.**	**Sig. diff.**
350	249.0 – 425.4	no diff.	121.2 – 493.2	no diff.	no diff.
550	555.9 – 641.9	no diff.	290.4 – 623.4	no diff.	**Sig. diff.**
700	565.0 – 739.4	no diff.	578.6 – 784.8	no diff.	no diff.
1500	1008 – 1844	no diff.	-280.0 – 2333	no diff.	no diff.
3000	2722 – 3763	no diff.	601.7 – 2250	**Sig. diff.**	**Sig. diff.**
5500	4305 – 6681	no diff.	921.4 – 4465	**Sig. diff.**	**Sig. diff.**

Table 2.1: Sample mean t-tests for spiked sample recoveries from Immunoarray and ELISA performed to determine the accuracy of each analytical method. Two sample mean t-test is performed between Immunoarray and ELISA recoveries. ELISA is found to underperform outside the concentration range of 350 - 1500 ng mL^{-1}.

* represents two sample mean t-test analysis for the null hypothesis, ELISA recovered concentration = Immunoarray recovered concentration
sig. diff. represents significantly different based on $t_{statistical} > t_{critical}$ or $P < 0.05$
no diff. represents statistically similar based on $t_{statistical} < t_{critical}$ or $P > 0.05$

From Table 2.1, we conclude that significant bias exists outside the concentration range of 350 - 1500 ng mL^{-1} for ELISA. Such trend is not observed for our method; specifically the immunoarray detection method yields recovery concentrations statistically similar to true spiked levels at 95% CI at all spiked levels.

Furthermore, immunoarray and ELISA methods are compared using the two sample mean t-test (Table 2.1).[41,42] Specifically, in our case, null hypothesis is set such that ELISA recovery = immunoarray recovery. Statistically relevant differences exit in recoveries if $t_{statistical} > t_{critical}$ ($P < 0.05$). Upon analysis, we concluded that good correlation exists for the CD62L range of 350-1500 ng mL^{-1}, with exception of 550 ng mL^{-1} (Table 2.1). These results indicate better accuracy of the immunoassay over the ELISA method, and reveal large systematic errors at the low and high concentration ranges for the ELISA kit.

Additional statistical analysis of correlation plots for spiked sample analyses provide further information on the accuracy of ELISA method. A slope of 1.0 and y-intercept of 0 ± 3SD indicates that analytical methods correlate very well, i.e. recoveries from both methods would be statistically similar. Verification of statistically relevant differences in slopes is performed by linear regression t-tests at 95% confidence interval (CI), see Table 2.2.[42] Recovered concentrations are utilized and $t_{statistical}$ is calculated using deviation from expected slope of 1 and observed standard error of the slope. Meanwhile, $t_{critical}$ is a tabulated value from required CI and degrees of freedom.[41,42] In cases where $t_{statistical} > t_{critical}$ ($P < 0.05$), deviations from expected results are statistically significant. As observed in Table 2.2 the only recoveries from immunoarray are statistically similar to true spiked concentrations ($P > 0.05$). ELISA recoveries are statistically different at $P = <0.00001$. These results further showed presence of systematic error in the ELISA method.

Linear Regression Plot	Slope ± SD	y-intercept ± SD ($ng\ mL^{-1}$)	t-test at 95% CI
Immunoarray vs. Spiked level*	1.013 ± 0.020	0.1298 ± 46.86	no diff.
ELISA vs. Spiked level*	0.4551 ± 0.0327	195.1 ± 75.3	**Sig. diff.**

Table 2.2: Linear regression t-test for spiked sample correlation plots. On accurate and precise measurement, the correlation plot will have slope of 1 and y-intercept of 0. Immunoarray shows statistically similar values to expected results, whereas ELISA does not have accurate recoveries for spiked samples.

* n = 8, Null hypothesis is slope of correlation plot = 1.
sig. diff. represents significantly different based on $t_{statistical} > t_{critical}$ or $P < 0.05$
no diff. represents statistically similar based on $t_{statistical} < t_{critical}$ or $P > 0.05$

2.4.3 Analysis of Bladder Cancer Patient Samples

The microfluidic immunoarray protocol is utilized to analyze 41 serum samples from bladder cancer patients divided across four subsets: 10 samples from cancers-free control individuals, 11 from patients with low- grade tumors, 10 with high-grade tumors expressing no metastasis, and 10 samples from at least regionally metastasized high-grade tumors. The resulting immunoarray average CD62L protein levels (Figure 2.10A) are 367 ± 141 ng mL^{-1} for controls, 2243 ± 839 ng mL^{-1} for low-grade, 4551 ± 1662 ng mL^{-1} high-grade non-metastatic, and 1177 ± 532 ng mL^{-1} for high-grade metastatic tumors. Furthermore, ELISA is also done

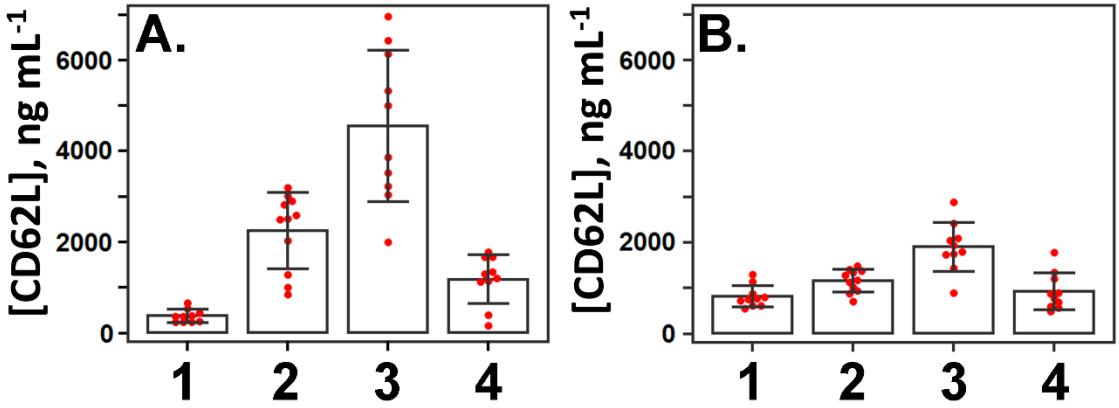

Figure 2.10: Box plot analysis for 41 patient samples for four different subsets (1 = cancer free controls, 2 = low-grade tumors, 3 = high-grade non-metastatic tumors, and 4 = high-grade metastatic tumors): (A) Immunoarray (B) ELISA. Red dots represent individual recovered patient sample concentrations. Box top represents the mean and error bars are plotted at 1 standard deviation of the mean.

and yielded results that are significantly different for these samples, presumably related to the large errors found in the ELISA assay (Figure 2.10B).

Box plots visualize trends in CD62L levels for the four subsets of patient samples for the electrochemical immunoarray and ELISA (Figure 2.10A-B). An ascending trend in circulating CD62L levels is observed concurrent with increasing severity of bladder cancer stage, with the exception of high-grade metastatic tumors for which CD62L levels in serum are lower than for high-grade non-metastatic tumors. The box plots indicate minimal overlap between the pooled

sample data for the individual sample subsets and t-tests confirmed that each subset had statistically different means at 95% confidence (Table 2.3).

Assay type	Assay type	t-test at 95% CI
Cancer-free controls vs. All Cancers	Immunoarray	**Sig. diff.**
	ELISA	**Sig. diff.**
Cancer-free controls vs. Low-Grade	Immunoarray	**Sig. diff.**
	ELISA	**Sig. diff.**
Cancer-free controls vs. High-Grade Non-Metastatic	Immunoarray	**Sig. diff.**
	ELISA	**Sig. diff.**
Cancer-free controls vs. High-Grade Metastatic	Immunoarray	**Sig. diff.**
	ELISA	no diff.
Low-Grade vs. High-Grade Non-Metastatic	Immunoarray	**Sig. diff.**
	ELISA	**Sig. diff.**
Low-Grade vs. High-Grade Metastatic	Immunoarray	**Sig. diff.**
	ELISA	no diff.
High-Grade Non-Metastatic vs. High-Grade Metastatic	Immunoarray	**Sig. diff.**
	ELISA	**Sig. diff.**

Table 2.3: Two sample mean t-test to differentiate patient sample subsets. P-value < 0.05 suggests the difference between subset averages is statistically significant, i.e. the test can differentiate between the two subsets based on CD62L concentration.

n = 10 for cancer-free controls patient subset, n = 11 for low-grade tumors subset, n = 10 for high-grade non-metastatic tumors and n = 10 for high-grade metastatic tumor subset.
Null hypothesis is set as:
mean of patient sample subset 1 = mean of patient sample subset 2.
sig. diff. represents significantly different based on $t_{statistical} > t_{critical}$ or $P < 0.05$
no diff. represents statistically similar based on $t_{statistical} < t_{critical}$ or $P > 0.05$

The null hypothesis is set such that the average recovered CD62L concentration for subset 1 = subset 2. In this case, $t_{statistical} > t_{critical}$ ($P < 0.05$) signified statistically relevant difference between the recovered CD62L concentrations for the subsets under consideration, i.e. the method is able to distinguish between the two patient sample subsets. From Table 2.3, both assay detection methods distinguish tumor grade based upon circulating detected CD62L, with the exception of ELISA for control vs. high-grade metastatic as well as low-grade vs. high-grade metastatic tumors. Thus, the previous report of higher CD62L serum levels in metastatic vs. non-metastatic bladder cancers[7] is possibly biased by the systematic ELISA error. Although both assay detection methods differentiate between patient sample subsets, the immunoarray method performs at a higher confidence level ($P_{Immunoarray} << P_{ELISA}$). The immunoarray analyses of serum samples from bladder cancer patients show a clear up-regulation in circulating CD62L levels progressing from controls to non-metastatic low-grade to non-metastatic high-grade cancers.

Receiver-operator characteristic (ROC) plots on the patient sample data are done to assess diagnostic utility. Here, sensitivity (true positive rate) is plotted against 100-specificity (false positive rate) for a series of concentration thresholds. An assay with perfect discrimination has a ROC curve that has 100% sensitivity and specificity).[43] The area under a ROC curve (AUC) quantifies the overall ability of the test to discriminate between individuals in 2 different classes, e.g. with and without cancer. Data with zero false positives and zero false negatives has an AUC of 1.00. ROC plots are obtained (Figure 2.11) for all pair combinations of patient sample subsets to obtain corresponding sensitivity and specificity values, AUC, and optimal concentration thresholds. Sensitivity $\geq$ 70%, specificity $\geq$ 70%, and AUC $\geq$ 0.50 are obtained for both Immunoarray and ELISA for all but one ROC pair grouping (Table 2.4).

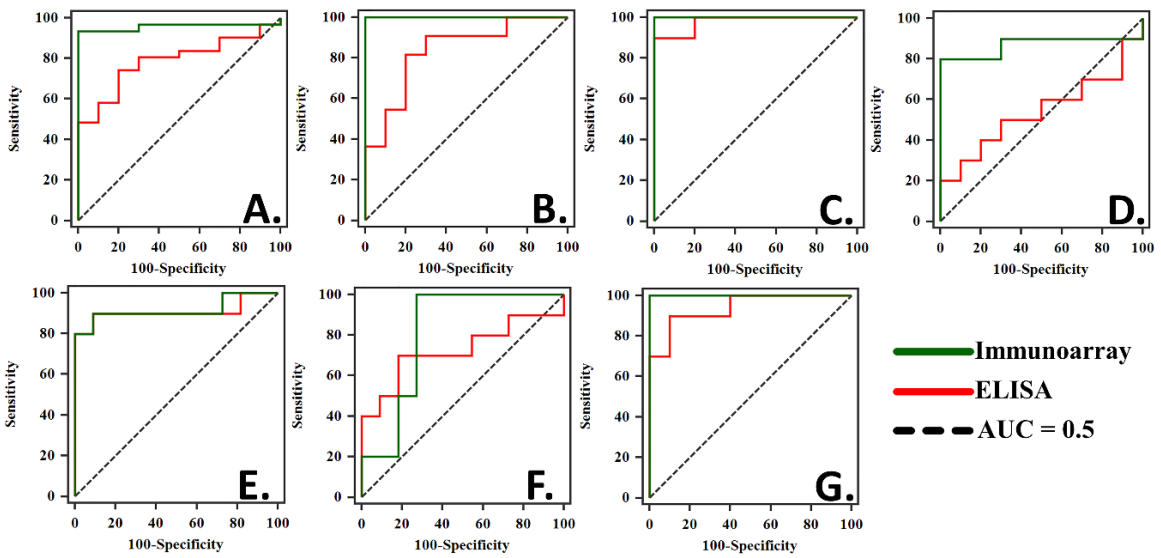

Figure 2.11: Receiver operating characteristic (ROC) curves comparing (A) cancer free-controls vs. all cancer patient samples, (B) controls vs. low-grade tumors, (C) controls vs. high-grade non-metastatic tumors, (D) controls vs. high grade metastatic tumors, (E) low-grade vs. high-grade non-metastatic tumors, (F) low grade vs. high-grade metastatic tumors, and (G) high-grade non-metastatic vs. high-grade metastatic tumors.

ROC Comparison	Assay type	Sensitivity	Specificity	AUC	Criterion
Cancer-free controls vs. All Cancers	Immunoarray	93.55	100.0	0.958	> 649.7
	ELISA	74.19	80.00	0.787	> 873.8
Cancer-free controls vs. Low-Grade	Immunoarray	100.0	100.0	1.000	> 649.7
	ELISA	81.82	80.00	0.836	> 873.8
Cancer-free controls vs. High-Grade Non-Metastatic	Immunoarray	100.0	100.0	1.000	> 649.7
	ELISA	90.00	100.0	0.980	> 1291
Cancer-free controls vs. High-Grade Metastatic	Immunoarray	80.00	100.0	0.870	> 649.7
	ELISA	40.00	80.00	0.540	> 873.8
Low-Grade vs. High-Grade Non-Metastatic	Immunoarray	90.00	90.91	0.918	> 3010
	ELISA	90.00	90.91	0.909	> 1401
Low-Grade vs. High-Grade Metastatic	Immunoarray	100.0	72.23	0.809	≤ 1783
	ELISA	70.00	81.82	0.727	≤ 881.0
High-Grade Non-Metastatic vs. High-Grade Metastatic	Immunoarray	100.0	100.0	1.000	≤ 1783
	ELISA	90.00	90.00	0.940	≤ 1338

Table 2.4: ROC analysis parameters for patient sample subsets. Immunoarray has consistently more accurate performance in patient sample subset differentiation compared to ELISA. The criteria concentration value is selected at the best sensitivity and specificity when multiple differential concentration criteria points are available.

n = 10 for cancer-free controls patient subset, n = 11 for low-grade tumors subset, n = 10 for high-grade non-metastatic tumors and n = 10 for high-grade metastatic tumor subset.
Perfect patient sample subset discrimination will have sensitivity = 100%, specificity = 100%, and AUC = 1.0.
The criterion value is the discriminating concentration of CD62L, above or below which the sample will be assessed into different patient sample subsets.

Significant differences are found by two sample mean t-test ($P < 0.05$, Table 2.3) for all subsets comparisons, except for cancer-free controls vs. high-grade metastatic and low-grade vs. high-grade metastatic for ELISA.[42] Importantly, both immunoarray and ELISA are able to differentiate between low-grade and high-grade lesions, prior to metastasis (sensitivity = 90%, specificity = 91%, Table 2.4), despite systematic errors in the ELISA assay. However, metastatic samples could not be distinguished from low or high-grade non-metastatic cancers since serum CD62L levels are lower in the metastatic samples. Clearly, the immunoarray protocol provides better sensitivity and specificity compared to the ELISA kit. Consequently, the Immunoarray detection provides better discrimination between the different tumor classifications.

2.4.4 Comparison of Patient Sample Results for Immunoarray and ELISA

Immunoarray results for circulating CD62L levels are plotted against standard ELISA results for the 41 patient samples (10 healthy and 31 cancer samples). A linear correlation plot produces a slope of 2.764 ± 0.283, y-intercept of -1208 ± 371, and $R^2 = 0.710$, as seen in Figure 2.12. Since immunoarray accuracy is already verified (Figure 2.9B-C), this plot further confirms that the ELISA kit underestimates CD62L levels in serum A correlation plot of immunoarray vs. ELISA recoveries for spiked samples shows results similar to the patient sample correlation plot (as seen in Figure 2.12, Table 2.5), indicating that systematic errors in the ELISA are also observed during patient sample analysis. These results are statistically different from expected linear correlation (slope = 1 and y-intercept = 0), when subjected to linear regression t-test (as per above procedure) at 95% CI ($P < 0.05$) (Table 2.5) and at 90% CI (data not shown).

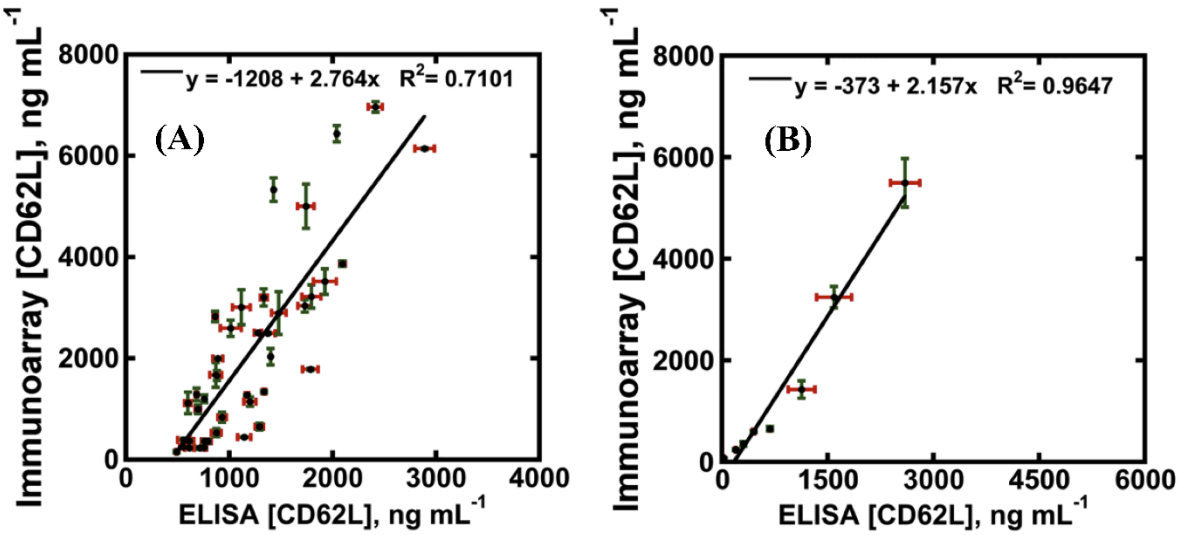

Figure 2.12: Linear correlation plots for Immunoarray vs. ELISA results for detection of CD62L in serum samples from patient samples. ELISA underestimates patient sample CD62L levels, as seen by slope = 2.76.

Linear Regression Plot	Slope ± SD	y-intercept ± SD (ng mL^{-1})	t-test at 95% CI
Spiked sample recoveries§ Immunoarray vs. Spiked level*	2.157 ± 0.169	-373.0 ± 201.0	**Sig. diff.***
Patient sample recoveries‡ ELISA vs. Spiked level*	2.764 ± 0.283	-1208 ± 371	**Sig. diff.***

Table 2.5: Linear regression t-test for spiked sample and patient sample correlation plot. Both plots have statistically similar slopes and y-intercepts, indicating that systematic error in ELISA equally affects both spiked sample and patient sample analysis.

§ n = 8 for spiked sample correlation plot, ‡ n = 41 for patient sample correlation plot.
Null hypothesis is slope of correlation plot = 1.
* represents statistically similar systematic error between the patient sample recoveries and spiked sample recoveries, by linear regression t-test.
sig. diff. represents significantly different based on $t_{statistical} > t_{critical}$ or $P < 0.05$.
no diff. represents statistically similar based on $t_{statistical} < t_{critical}$ or $P > 0.05$

Furthermore, linear regression is also plotted for spiked sample recoveries (Figure 2.12B). A mean t-test for the two regression slopes yield P = 0.2196 at 95% CI and since P > 0.05, systematic error in CD62L ELISA is uniformly present in both spiked and patient sample analysis, as noted in Table 2.5. Moreover, similar to patient sample correlation, spiked samples correlation plot different significantly from expected linear plot with slope =1 and y-intercept = 0.

2.5 Discussion

Results show that a newly optimized bead-based microfluidic immunoassay for CD62L gave much better accuracy and sensitivity than ELISA (Figure 2.9, Figure 2.11, Figure 2.12; Table 2.1Table 2.5). Most serum protein ELISAs are reliable and are often used as referee assays to compare to newly developed methods for protein measurement. However, results reported here suggest the importance of verifying the accuracy of each ELISA method as well, before using it as a reference method. In the present case, the CD62L ELISA significantly underestimated CD62L levels outside the serum concentration range of 350 - 1500 ng mL^{-1}. Results from spiked sample analyses and correlation plot slopes (Figure 2.9, Figure 2.12) are further analyzed with the one sample mean t-test, two sample mean t-test, and linear regression (Table 2.1-2.5), and confirm systematic error in ELISA in both spiked and patient sample analysis as do Figure 2.9 and Figure 2.12. These errors affect spiked sample recoveries (Figure 2.9) and patient sample analysis (Figure 2.12) equally.

The recovered concentrations for patient samples from ELISA had a bias in low (< 350 ng mL^{-1}) and high concentration ranges (>1500 ng mL^{-1}), thus partially masking clear distinction between the four patient sample classes as (Figure 2.10). In contrast, recoveries with

the bead-based microfluidic immunoassay provide accurate estimates of circulating CD62L levels in patient serum samples. Extensive statistical analyses strongly support the reliability and accuracy of the new microfluidic CD62L immunoarray. Additionally, the immunoarray's dynamic range can be easily modified to suit the relevant concentration range of the samples by modulating the number of HRP labels and antibodies on the magnetic beads. The immunoarray protocol provides the additional benefit of allowing a single dilution factor over the entire dynamic range. Due to higher sensitivity and good accuracy, this semi-automated microfluidic assay module provides a promising tool with low technical burden for protein CD62L in a short assay time of 30 mins using low patient sample volumes.

High CD62L gene and cellular expression reported previously supported a substantial increase in soluble CD62L protein expression with increasing stage of the disease.[7] We observed a distinct elevation in circulating CD62L protein level between low-grade and high-grade tumor patients prior to metastasis for both methods, while our immunoassay provided a sharper differentiation between the various sample sub-groups. Since the number of patient samples is relatively small, and no data is available on patient outcomes subsequent to sample collection, results provided here are still clinically inconclusive concerning diagnostic utility of CD62L. Further studies with larger sample size and accurate timeline of clinical outcomes are warranted to evaluate the performance of this more accurate and reliable method for quantification of serum CD62L.

2.6 Conclusions

A sensitive, accurate bead-based immunoarray method for detection of CD62L is documented with tunable dynamic range by optimizing the number of enzyme labels on magnetic beads. Accurate detection of circulating CD62L revealed increasing levels of CD62L from low-grade vs. high-grade lesions in bladder cancer, and if fully verified may offers serum-based test for bladder cancer staging. Panels of biomarkers could also be investigated with this methodology in future to enhance diagnostic power for staging and grading bladder cancer.

2.7 References

(1) American Cancer Society. *Cancer Facts & Figures 2018*; Atlanta, 2018.

(2) TCGA bladder cancer study reveals potential drug targets, similarities to several cancers, 2014. National Human Genome Research Institute Web Site. https://www.genome.gov/27556023/ (accessed May 11, 2018).

(3) Goodison, S.; Rosser, C. J.; Urquidi, V. Bladder Cancer Detection and Monitoring: Assessment of Urine- and Blood-Based Marker Tests. *Mol. Diagnosis Ther.* **2013**, *17* (2), 71–84.

(4) Bladder Cancer Staging | Bladder Cancer Stages, 2017. American Cancer Society. https://www.cancer.org/cancer/bladder-cancer/detection-diagnosis-staging/staging.html (accessed May 13, 2018).

(5) Herr, H. W.; Donat, S. M. Outcome of Patients with Grossly Node Positive Bladder Cancer after Pelvic Lymph Node Dissection and Radical Cystectomy. *J. Urol.* **2001**, *165* (1), 62–64.

(6) Noone, A. M.; Howlader, N.; Krapcho, M.; Miller, D.; Brest, A.; Yu, M.; Ruhl, J.; Tatalovich, Z.; Mariotto, A.; Lewis, D. R.; et al. *SEER Cancer Statistics Review, 1975-2015*; Bethesda, MD, 2018.

(7) Choudhary, D.; Hegde, P.; Voznesensky, O.; Choudhary, S.; Kopsiaftis, S.; Claffey, K. P.; Pilbeam, C. C.; Taylor, J. A. Increased Expression of L-Selectin (CD62L) in High-Grade Urothelial Carcinoma: A Potential Marker for Metastatic Disease. *Urol. Oncol. Semin. Orig. Investig.* **2015**, *33* (9), 387.e17-387.e27.

(8) Stein, J. P.; Lieskovsky, G.; Cote, R.; Groshen, S.; Feng, A. C.; Boyd, S.; Skinner, E.;

Bochner, B.; Thangathurai, D.; Mikhail, M.; et al. Radical Cystectomy in the Treatment of Invasive Bladder Cancer: Long-Term Results in 1,054 Patients. *J. Clin. Oncol.* **2001**, *19* (3), 666–675.

(9) Tests for Bladder Cancer, 2016. American Cancer Society. https://www.cancer.org/cancer/bladder-cancer/detection-diagnosis-staging/how-diagnosed.html (accessed May 14, 2018).

(10) Can Bladder Cancer Be Found Early?, 2016. American Cancer Society. https://www.cancer.org/cancer/bladder-cancer/detection-diagnosis-staging/detection.html (accessed May 14, 2018).

(11) Faus, C.; Roda, D.; Frasson, M.; Roselló, S.; García-Granero, E.; Flor-Lorente, B.; Navarro, S. The Role of the Pathologist in Rectal Cancer Diagnosis and Staging and Surgical Quality Assessment. *Clin. Transl. Oncol.* **2010**, *12* (5), 339–345.

(12) Kumar, R.; Srivastava, R.; Srivastava, S. Detection and Classification of Cancer from Microscopic Biopsy Images Using Clinically Significant and Biologically Interpretable Features. *J. Med. Eng.* **2015**, *2015*, 1–14.

(13) UroVysion Bladder Cancer Kit | Abbott Molecular. Abbott Web Site. https://www.molecular.abbott/int/en/products/oncology/urovysion-bladder-cancer-kit (accessed May 13, 2018).

(14) Nasuti, J. F.; Gomella, L. G.; Ismial, M.; Bibbo, M. Utility of the BTA Stat Test Kit for Bladder Cancer Screening. *Diagn. Cytopathol.* **1999**, *21* (1), 27–29.

(15) Têtu, B.; Tiguert, R.; Harel, F.; Fradet, Y. ImmunoCyt/UCyt+^{TM} Improves the Sensitivity of Urine Cytology in Patients Followed for Urothelial Carcinoma. *Mod. Pathol.* **2005**, *18* (1), 83–89.

(16) Wang, Z.; Que, H.; Suo, C.; Han, Z.; Tao, J.; Huang, Z.; Ju, X.; Tan, R.; Gu, M. Evaluation of the NMP22 BladderChek Test for Detecting Bladder Cancer: A Systematic Review and Meta-Analysis. *Oncotarget* **2017**, *8* (59), 100648–100656.

(17) Otieno, B. A.; Krause, C. E.; Latus, A.; Chikkaveeraiah, B. V.; Faria, R. C.; Rusling, J. F. On-Line Protein Capture on Magnetic Beads for Ultrasensitive Microfluidic Immunoassays of Cancer Biomarkers. *Biosens. Bioelectron.* **2014**, *53*, 268–274.

(18) Krause, C. E.; Otieno, B. A.; Bishop, G. W.; Phadke, G.; Choquette, L.; Lalla, R. V.; Peterson, D. E.; Rusling, J. F. Ultrasensitive Microfluidic Array for Serum Pro-Inflammatory Cytokines and C-Reactive Protein to Assess Oral Mucositis Risk in Cancer Patients. *Anal. Bioanal. Chem.* **2015**, *407* (23), 7239–7243.

(19) Christiansen, A.; Detmar, M. Lymphangiogenesis and Cancer. *Genes Cancer* **2011**, *2* (12), 1146–1158.

(20) Williams, S. G.; Stein, J. P. Molecular Pathways in Bladder Cancer. *Urol. Res.* **2004**, *32* (6), 373–385.

(21) Milowsky, M. I.; Bryan Rumble, R.; Booth, C. M.; Gilligan, T.; Eapen, L. J.; Hauke, R. J.; Boumansour, P.; Lee, C. T. Guideline on Muscle-Invasive and Metastatic Bladder Cancer (European Association of Urology Guideline): American Society of Clinical Oncology Clinical Practice Guideline Endorsement. *J. Clin. Oncol.* **2016**, *34* (16), 1945–1952.

(22) Haznedaroğlu, I. C.; Benekli, M.; Ozcebe, O.; Savaş, M. C.; Güllü, I. H.; Dündar, S. V; Kirazli, Ş. Serum L-Selectin and P-Selectin Levels in Lymphomas. *Haematologia (Budap).* **2000**, *30* (1), 27–30.

(23) Matsuura, N.; Narita, T.; Mitsuoka, C.; Kimura, N.; Kannagi, R.; Imai, T.; Funahashi, H.; Takagi, H. Increased Level of Circulating Adhesion Molecules in the Sera of Breast Cancer Patients with Distant Metastases. *Jpn. J. Clin. Oncol.* **1997**, *27* (3), 135–139.

(24) Wittig, B. M.; Kaulen, H.; Thees, R.; Schmitt, C.; Knolle, P.; Stock, J.; Meyer zum Büschenfelde, K. H.; Dippold, W. Elevated Serum E-Selectin in Patients with Liver Metastases of Colorectal Cancer. *Eur. J. Cancer* **1996**, *32* (7), 1215–1218.

(25) Belanger, S. D.; St-Pierre, Y. Role of Selectins in the Triggering, Growth, and Dissemination of T-Lymphoma Cells: Implication of L-Selectin in the Growth of Thymic Lymphoma. *Blood* **2005**, *105* (12), 4800–4806.

(26) Vlad, A.; Deglesne, P.-A.; Letestu, R.; Saint-Georges, S.; Chevallier, N.; Baran-Marszak, F.; Varin-Blank, N.; Ajchenbaum-Cymbalista, F.; Ledoux, D. Down-Regulation of CXCR4 and CD62L in Chronic Lymphocytic Leukemia Cells Is Triggered by B-Cell Receptor Ligation and Associated with Progressive Disease. *Cancer Res.* **2009**, *69* (16), 6387–6395.

(27) Ay, C.; Simanek, R.; Vormittag, R.; Dunkler, D.; Alguel, G.; Koder, S.; Kornek, G.; Marosi, C.; Wagner, O.; Zielinski, C.; et al. High Plasma Levels of Soluble P-Selectin Are Predictive of Venous Thromboembolism in Cancer Patients: Results from the Vienna Cancer and Thrombosis Study (CATS). *Blood* **2008**, *112* (7), 2703–2708.

(28) McEver, R. P. Selectin-Carbohydrate Interactions during Inflammation and Metastasis. *Glycoconj. J.* **1997**, *14* (5), 585–591.

(29) Qian, F.; Hanahan, D.; Weissman, I. L. L-Selectin Can Facilitate Metastasis to Lymph Nodes in a Transgenic Mouse Model of Carcinogenesis. *Proc. Natl. Acad. Sci. U. S. A.* **2001**, *98* (7), 3976–3981.

(30) Arbonés, M. L.; Ord, D. C.; Ley, K.; Ratech, H.; Maynard-Curry, C.; Otten, G.; Capron, D. J.; Teddert, T. F. Lymphocyte Homing and Leukocyte Rolling Are Impaired in L-Selectin Deficient Mice. *Immunity* **1994**, *1* (4), 247–260.

(31) Dixit, C. K.; Kadimisetty, K.; Otieno, B. A.; Tang, C.; Malla, S.; Krause, C. E.; Rusling, J. F. Electrochemistry-Based Approaches to Low Cost, High Sensitivity, Automated, Multiplexed Protein Immunoassays for Cancer Diagnostics. *Analyst* **2016**, *141* (2), 536–547.

(32) Rusling, J. F.; Bishop, G. W.; Doan, N. M.; Papadimitrakopoulos, F. Nanomaterials and

Biomaterials in Electrochemical Arrays for Protein Detection. *J. Mater. Chem. B* **2014**, *2* (1), 12–30.

(33) Rusling, J. F.; Kumar, C. V.; Gutkind, J. S.; Patel, V. Measurement of Biomarker Proteins for Point-of-Care Early Detection and Monitoring of Cancer. *Analyst* **2010**, *135* (10), 2496–2511.

(34) Krause, C. E.; Otieno, B. A.; Latus, A.; Faria, R. C.; Patel, V.; Gutkind, J. S.; Rusling, J. F. Rapid Microfluidic Immunoassays of Cancer Biomarker Proteins Using Disposable Inkjet-Printed Gold Nanoparticle Arrays. *ChemistryOpen* **2013**, *2* (4), 141–145.

(35) Chikkaveeraiah, B. V.; Mani, V.; Patel, V.; Gutkind, J. S.; Rusling, J. F. Microfluidic Electrochemical Immunoarray for Ultrasensitive Detection of Two Cancer Biomarker Proteins in Serum. *Biosens. Bioelectron.* **2011**, *26* (11), 4477–4483.

(36) Chikkaveeraiah, B. V; Soldà, A.; Choudhary, D.; Maran, F.; Rusling, J. F. Ultrasensitive Nanostructured Immunosensor for Stem and Carcinoma Cell Pluripotency Gatekeeper Protein NANOG. *Nanomedicine* **2012**, *7* (7), 957–965.

(37) Malhotra, R.; Patel, V.; Chikkaveeraiah, B. V.; Munge, B. S.; Cheong, S. C.; Zain, R. B.; Abraham, M. T.; Dey, D. K.; Gutkind, J. S.; Rusling, J. F. Ultrasensitive Detection of Cancer Biomarkers in the Clinic by Use of a Nanostructured Microfluidic Array. *Anal. Chem.* **2012**, *84* (14), 6249–6255.

(38) Otieno, B. A.; Krause, C. E.; Jones, A. L.; Kremer, R. B.; Rusling, J. F. Cancer Diagnostics via Ultrasensitive Multiplexed Detection of Parathyroid Hormone-Related Peptides with a Microfluidic Immunoarray. *Anal. Chem.* **2016**, *88* (18), 9269–9275.

(39) Smith, P. K.; Krohn, R. I.; Hermanson, G. T.; Mallia, A. K.; Gartner, F. H.; Provenzano, M. D.; Fujimoto, E. K.; Goeke, N. M.; Olson, B. J.; Klenk, D. C. Measurement of Protein Using Bicinchoninic Acid. *Anal. Biochem.* **1985**, *150* (1), 76–85.

(40) Pütter, J.; Becker, R. Peroxidases. In *Methods of Enzymatic Analysis Vol. III*; Bergmeyer, H.-U., Ed.; Verlug Chemie: Deerfields Beach, FL, 1983; pp 286–293.

(41) Harris, D. C. Statistics. In *Quantitative Chemical Analysis*; W. H. Freeman and Company: New York, 2007; pp 53–77.

(42) McDonald, J. H. *Handbook of Biological Statistics*, 3rd ed.; Sparky House Publishing: Baltimore, MD, 2014.

(43) Zweig, M. H.; Campbell, G. Receiver-Operating Characteristic (ROC) Plots: A Fundamental Evaluation Tool in Clinical Medicine. *Clin. Chem.* **1993**, *39* (4), 561–577.

Chapter 3

Inkjet Printed Optical Phase Tags for Improved Counterfeit Detection

3.1 Abstract

An Optical Phase Tag (OPT) is fabricated by deposition of Zinc Oxide (ZnO) pattern on Aluminum (Al) substrate. A prototype OPT is inkjet printed on an integrated circuit (IC) in the shape of a quick-response (QR) code. This unique and low-cost OPT with a simple, yet elegant fabrication process makes the tag more secure and less likely to be breached by an attacker. Moreover, the controlled quilt building and layering process allows OPT to securely store valuable information about an object, such as a data sheet or a 3D image object. Nano-materials are applied for fabrication of these QR codes allowing customization of optical signatures. To authenticate the OPT, a two-step verification process is used: Polarimetric readings, and reflected light measurements. Material is inspected by illuminating the OPT with a coherent, linearly polarized light, analyzing the polarimetric readings, and computing the Stokes parameter. The second step involves using a coherent light source to illuminate the OPT and recording reflected light. This distinct signature is authenticated using nonlinear correlation. The two-step authentication process can successfully authenticate a true OPT, while providing a protocol for detecting counterfeit OPTs. Additionally, the fabrication process can be adapted to versatile array of substrates, expanding the use of such OPT authentication system.

3.2 Introduction

Counterfeit goods have a devastating effect on an economy, or even cost lives in case of counterfeit medicines. The U.S. government and the WHO has reported on increasing access to counterfeit medication as an emerging threat that goes beyond loss of revenue, to increased burden on the healthcare system and even loss of lives.[1,2] Besides medications, electronic parts and consumer goods are large contributors to the counterfeit markets worldwide.[3] Electronic counterfeiting can have far-reaching impact, especially in the aviation, defense, or aerospace industry.[4] Global value of counterfeit and pirated products is expected to reach $2.3 trillion by 2022, according to the International Chamber of Commerce.[5] The counterfeit market has a complex supply chain and has even crossed over into legitimate distribution, which prevents simple regulation measures from being effective.[1,2]

Improving counterfeit detection and manufacturing portable detection tools has attracted considerable research in recent years, with the market value predicted at $5.3 billion by 2025.[6] Common anti-counterfeiting strategies for electronic goods and components, such as analog, microprocessor or memory integrated circuits (ICs), transistors, include inclusion of tracking device or affixing tags or barcodes (that can be read with portable scanners) on to the packaging or the actual goods.[7–9] Tuyls and Batina[7] developed an anti-cloning strategy for the market available radio frequency identification (RFID) tags, which can be used for electronic tracking of a shipment. Physically unclonable functions have also been explored as a counterfeit detection method.[10] Romero et al[11] developed a protocol for quantifying the electromagnetic signature of these RFID tags as an anti-counterfeiting measure. However, these methods are expensive due to the sophisticated technology. Barcodes and Quick Response (QR) codes are currently used for

generating safety checks. Nevertheless, the visual code is easy to scan, hack, and replicate. To enhance effectiveness against counterfeiting, optical phase tags (OPT) have been recently introduced.[8,9,12–14] An OPT made of Scotch tape is placed on an IC using customized thin film deposition and lithography: Polarimetric measurements are added to the authentication process reducing possibility of fraud.[12] OPTs containing gold and other nanoparticles are also embedded in a quick-response code.[8,13] The polarization characteristics are examined using transmission mode setups; thus, no investigation is made into these OPTs placed on an object, such as an IC.

Selection of materials used to print the OPTs is crucial in establishing a sound, error-proof authentication process. Nanomaterial synthesis with shape and size selection can alter optical and conductive properties. Fabricating OPTs from such materials will provide customized optical systems, supplementing design of such low-error easy authentication tags.[15,16] ZnO ink is used to fabricate the tags in this following study: ZnO nanoparticles are a well-studied nanoparticle system with excellent control over optical properties and cheap synthesis protocols.[17–19] These printing inks can be further modified by introducing a) change in shape and size of particles[15], b) doping with metals, c) change in physical color manifestation by addition of a dye. Inkjet printing can easily fabricate customized QR code patterns for the OPTs by deposition of the ZnO ink; smooth adaption of this process to any target substrate makes it suitable for broad application purposes.[20,21]

Light waves have an associated electrical and magnetic field that is present in all x- and y- directions in case of non-polarized light. When light is polarized, the electrical wave is constrained to a single plane within the x- and y-axis. As light interacts with the surface, the reflected light can have different polarization from incident coherent light. This change is dependent on surface material, as well as incident wavelength and angle of incidence.

Stokes parameters is a set of values describing the polarization of an electromagnetic radiation accounting for individual parameters, i.e. total intensity, degree of polarization, shape parameters of the polarization circle or ellipse.[22] Degree of polarization quantifies how much of the incident light is polarized, from the Stokes parameters. Other than polarization, reflected light also has a unique speckle pattern, or the intensity image formed from interaction between light waves reflected off the object's surface. This noise-like pattern provides information about a material and can serve as a fingerprint as the light reflects differently due to the unique surface structure of the material. According to Goodman,[22] it can be reasonably assumed that the light reflected from surface is complex Gaussian. Thus a correlator function can be used to visualize the speckle pattern as a peak.

In this work, a two-step authentication scheme to determine the authenticity of an OPT is presented. An OPT of ZnO nanoparticles in inkjet printed on Aluminum (Al) coated substrate in the shape of a quick-response (QR) code. The fabrication of such tag directly onto an IC is also discussed. This unique OPT is then authenticated using a two-step scheme. First, material inspection is performed on the OPT by examining the polarimetric signatures of the OPT, under an incident coherent light, and computing the stokes parameters.[23,24] The recorded pattern can then be authenticated using non-linear correlation.[25] Moreover, we show that by using the two-step authentication system, we are able to successfully verify the authenticity of an OPT and its material composition. To the best of our knowledge, this is the first report of fabricating a complex optical phase tag directly on an object followed by both object authentication and material inspection.

3.3 Experimental

3.3.1 Chemicals and Instruments

Zinc acetate ($Zn(CH_3COO)_2$), copper acetate ($Cu(CH_3COO)_2$), nickel oxide (NiO), ethylene glycol (EG, $(CH_2OH)_2$), ethanol (EtOH, CH_3OH) are purchased from Sigma Aldrich (St. Louis, MO, USA). Common household Aluminum foil is purchased from a generic grocery shop. ICs are obtained from Analog Devices, and Intel. A Dimatix DMP-2800 Materials Printer from FUJIFILM Dimatix, Inc. (Santa Clara, CA, USA) is used for inkjet printing. Savannah 100 Atomic Layer Deposition System from Veeco Instruments (Waltham, MA) is used for aluminum layer deposition on ICs. Optical analysis is performed using a linearly polarized green laser diode light source, a neutral density filter, and a Canon EOS 5D Mark II camera, and a CCD.

3.3.2 Preparation of ZnO inks

The ZnO ink is prepared according to a previously reported method with modifications.[23] In a typical synthesis, 0.5 M $Zn(CH_3COO)_2$ solution is prepared in EG by heating at 110 °C for ½ hr to prepare a transparent solution. Once the solution is cooled to room temperature, EtOH is added to optimize the viscosity and the surface tension of the prepared ink (see Table 3.1). Filtration of the solution provides a clear and homogenous ZnO solution, with molal concentration at ~ 0.33 M, viscosity of 10-13.5 cP, and surface tension of 36-38 dyne cm^{-1}. Doped ZnO solutions are prepared by addition of 10% $Cu(CH_3COO)_2$ and 10% NiO dopants prior to filtration. The final solvent compositions of doped inks are also optimized (see Table 3.1). The successful synthesis of materials is validated by X-Ray Diffraction.

Solution #	Dopant	Solvent composition (EG:EtOH)	Viscosity (cP)	Surface tension (dynes cm^{-1})
1	No	4 : 1	49.435 (4.560)	34.863 (0.448)
2	**No**	**2 : 1**	**13.489 (0.732)**	**37.881 (0.924)**
3	No	1.5 : 1	7.222 (0.660)	33.927 (0.564)
4	*10 % Cu*	*2 : 1*	*9.931 (0.465)*	*36.241 (0.657)*
5	*10 % Ni*	*1.75 : 1*	*10.734 (0.539)*	*34.292 (2.161)*

Table 3.1: Pure ZnO inks are optimized for inkjet printing at suggested viscosity and surface tension ranges of 10-12 cP and 32-42 dyne cm^{-1} respectively. Final solvent composition of the ink for printing is selected at 2:1 EG:EtOH (**in bold**). With this benchmark, the 10% Cu and 10% Ni ion doped inks are optimized for final solvent composition of 2:1 and 1.75:1 EG:EtOH respectively (*in italics*). Errors for viscosity and surface tension are shown in parenthesis.

3.3.3 Substrate Selection and Optimization

Initial substrate optimization is required to achieve high surface adhesion, improving longevity of the OPTs. Glass, Kapton, untreated Aluminum (Al) foil, and NaOH-treated Al foil are tested for ZnO adhesion. Due to its hydrophilic surface, both untreated and NaOH treated Al foil show better adhesion for ZnO inks, in contrast to hydrophobic polymeric and glass substrates. Due to ease of preparation, untreated, washed Al foils are used as substrate for printing.

3.3.4 Fabrication of QR Code Prototypes

The datasheet for the IC (Figure 3.1A) is encrypted using the full-phase double-random-phase encryption (DRPE) (Figure 3.1B-C) with photon-counting (PC-DRPE) (Figure 3.1D), after assessing many different encryption algorithms.[22,26–28] Once the image is encrypted, the image is vectorized and Huffman coding is iteratively applied until the image sequence is sufficiently small and able to be stored in a QR code (Figure 3.1E).[29] After printing was optimized for Al foil, OPT is printed on a commercially available IC.

ICs are first coated with a thin Al layer (~ 100 nm thickness) by physical vapor deposition. QR code with 25 % or Q-level error allowance is designed online with QR code 2D barcode generator (RACO industries) (Figure 3.1F). The pattern is edited to 1040 dpi resolution and 1.0 cm x 1.0 cm size, and printed with a customized waveform and drop spacing of 15 μm using a Dimatix DMP-2800 Materials Printer. The printed patterns are annealed at 200°C for 1 hr to ensure total conversion to ZnO and solvent evaporation prior to optical analysis, as seen in Figure 3.1G.

Upon optimization of doped ZnO inks, 2D and 3D quilt patterns are designed as true and false class. 2D quilt pattern is printed such that specified areas of the QR code are printed with a combination of the undoped ZnO or Cu/ Ni doped inks in a quilt pattern, as illustrated in Figure 3.2A. The 3D quilt is fabricated by sequentially printing with different inks for each layer (see Figure 3.2B). The true and false class QR codes will differ by placement within a single layer in the former and by sequence of layers in the latter.

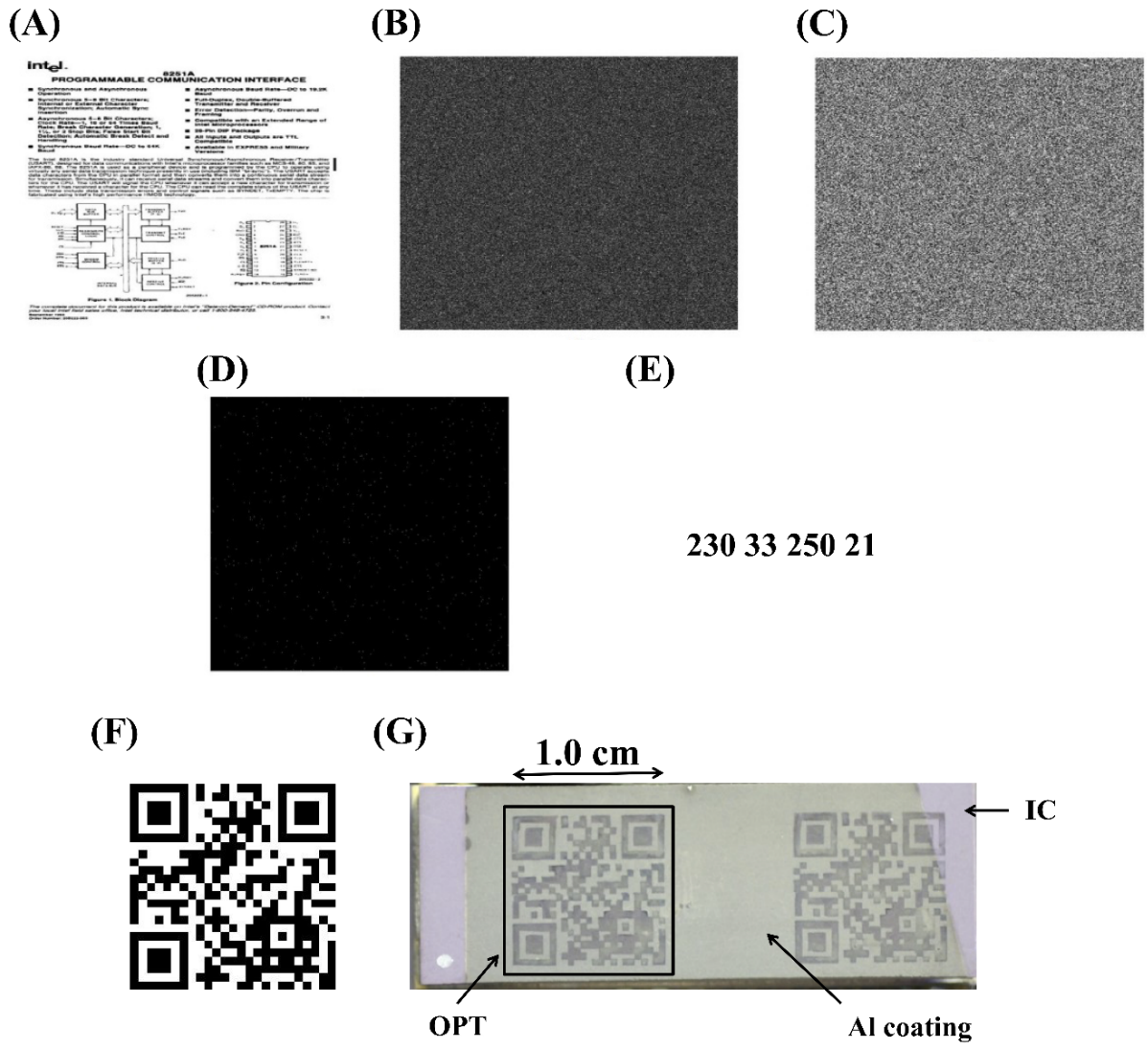

Figure 3.1: Generation and fabrication of an OPT on Al-coated IC. An IC datasheet (A) is encrypted with DRPE (B-C) and PC-DRPE (D). The image is then vectorized and Hoffman coding is applied till a small sequence is generated (E). A QR code is designed (F) using an online QR code 2D barcode generator (RACO industries). The OPT is inkjet printed (G) as a QR code on Al-coated IC using ZnO nanoparticle ink and measures 1 cm x 1 cm in size.

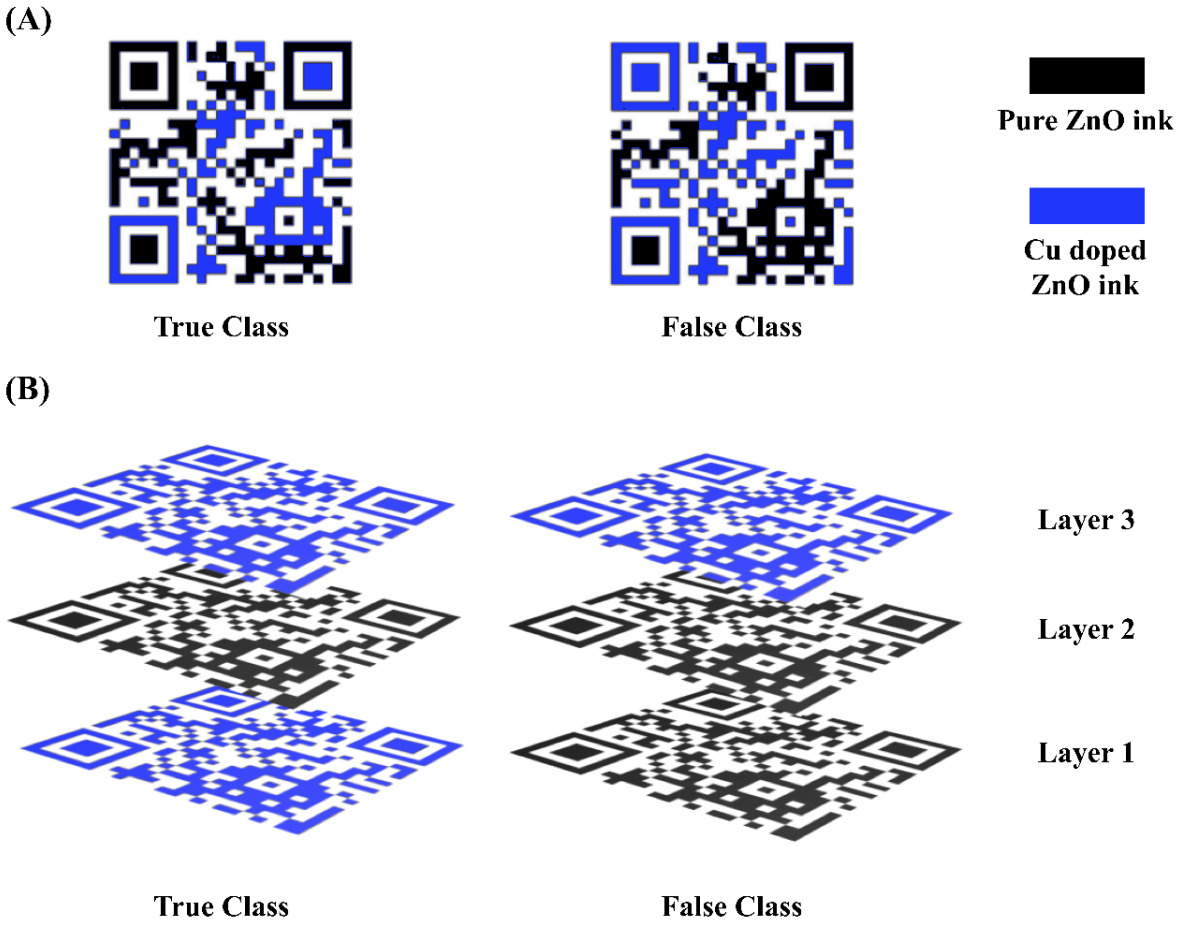

Figure 3.2: (A) 2D and (B) 3D quilt pattern QR code prototypes depict the different ways true and false class codes may be fabricated. (A) 2D quilt is fabricated by printing specified areas with patches of pure ZnO ink and the rest with doped ink (e.g. 10% Cu doped ZnO ink). The placement of doped ink will differ between true and false class. (B) 3D quilt is fabricated by printing successive layers of either pure or doped ZnO ink. The true and false classes of QR codes are differentiated by the sequence of the layers.

3.3.5 Authentication of QR Codes

The two-step authentication process for the OPTs includes polarimetric signature and speckle pattern signature. For both set of experiments, the optical setup consisted of a coherent laser light being incident on the OPT material and the reflected beam being captured by a CCD camera (Figure 3.3A-D). A neutral density filter is used to reduce the intensity of the laser diode. For polarimetric signature, a polarizer is added in the path of reflected light (Figure 3.3A-B). A resolution of 5616 x 3744 pixels and sensor size of 36 mm x 24 mm is used for detection, with an exposure time is set to 0.033 ms, F/# of 2.5 and ISO level of 5000.

Polarimetric signatures are recorded and Stokes parameters and the degree of polarization are calculated to characterize the OPT material composition. Degree of polarization can be computed by placing a polarizer in front of the recording sensor and analyzing intensity of recorded light, as shown in Figure 3.3A-B. The polarization is rotated 0^0, 45^0, 90^0, and 135^0 with respect to the x-axis of the cartesian coordinate system. Speckle pattern is captured directly by the camera without a polarizer, as illustrated in Figure 3.3C-D. Intensity of these patterns is recorded over time as many different speckles are imaged and their intensity decreases with time.[27] Image authentication is performed by applying k-th order nonlinear filter with $k = 0.3$ and comparing resulting peaks.[29]

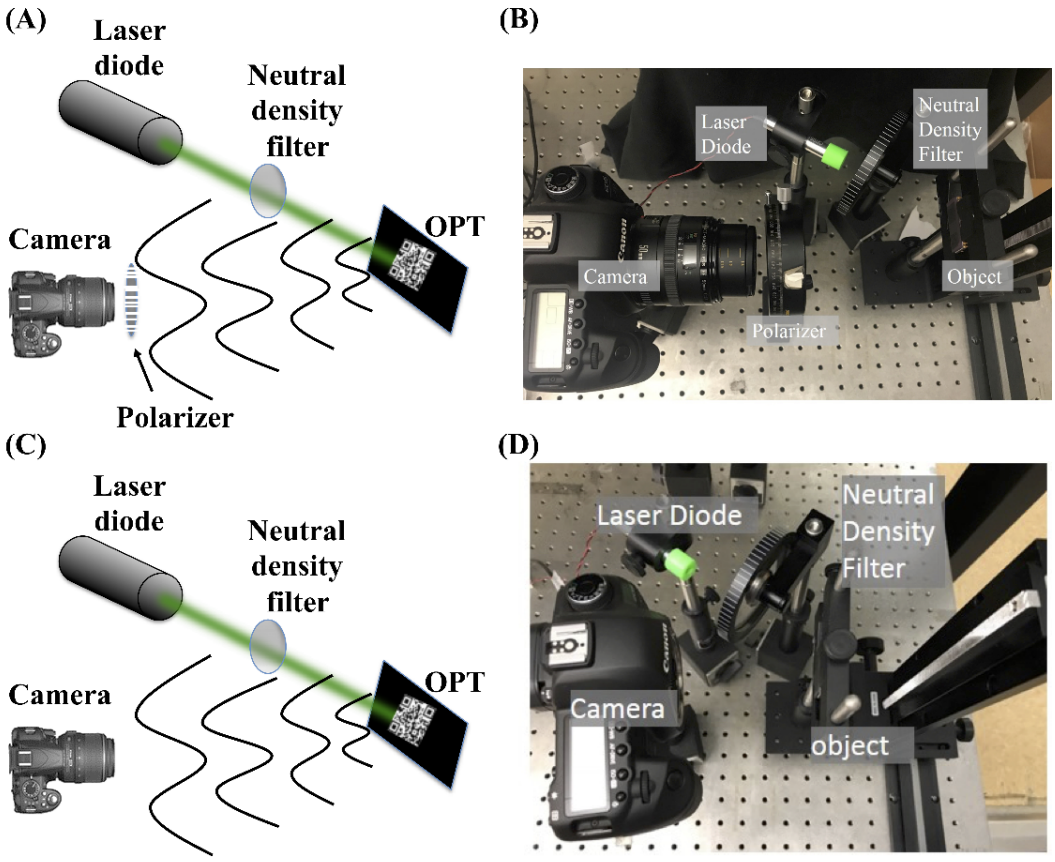

Figure 3.3: Experimental setup for polarimetric readings (A-B) and speckle pattern capture (C-D). (A) Schematic and (B) experimental optical setup for polarimetry consists of a green laser diode incident on the object. The reflected light is then passed through a polarizer and recorded by a CCD. For speckle authentication, (C) schematic and (D) experimental optical setup is similar, without the inclusion of a polarizer.

3.4 Results

3.4.1 Characterization of Pure and Doped ZnO Inks

Inkjet printed blocks of pure and doped ZnO inks are analyzed by transmission electron microscopy (TEM) for visual examination of effect of doping on the ZnO ink (Tecnai T12S/TEM, Thermo Fisher Scientific, Hillsboro, OR, USA), as seen in Figure 3.4A-C. The morphology observed for pure ZnO showed hexagonal structures ~ 20 nm in size. On doping with Cu and Ni, flat rectangular morphology is observed. Cu doped ZnO ink showed higher crystallinity than Ni doped ZnO ink.

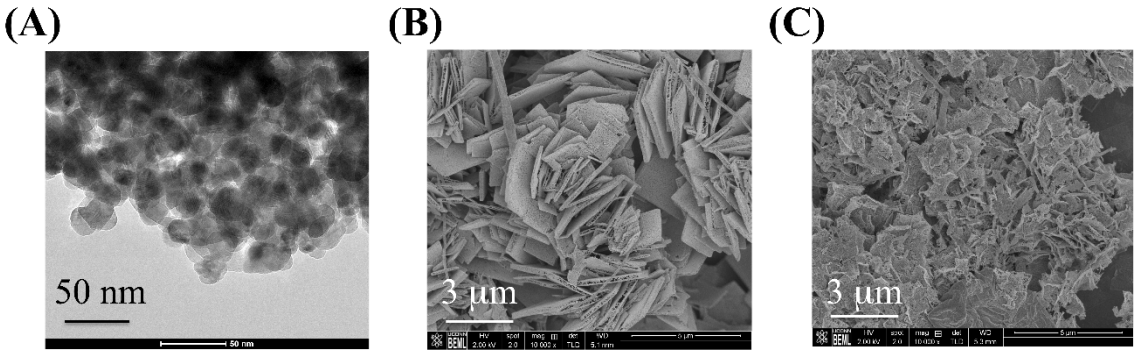

Figure 3.4: TEM images of (A) Pure ZnO, (B) 5 % Cu doped ZnO, and (C) 5 % Ni doped ZnO ink. The change in morphology, i.e. size and shape, of the crystals indicates that optical properties of inks will change upon doping.

3.4.2 Scanning QR Codes

Consistent fabrication of OPTs is achieved by selected printing method. The QR code is successfully scanned with either of two imaging methods: Simple scan by a generic smartphone QR code scanner app is able to read the encrypted number sequence, if enough contrast is present between the code and the IC. Otherwise, the code is simply imaged using the Canon EOS 5 camera, enlarged on a computer screen, and read using a smartphone app. A true-class OPT is defined as a error-free printed QR code on an Al-coated IC, as seen in Figure 3.5A: This will be referred to as OPT 1. OPT 1 is scanned (see Figure 3.5B), reading the encrypted and compressed data matching that from Figure 3.1E. This information is then decompressed and decrypted to yield a noise-like image (Figure 3.5C). For purpose of visual authentication, non-linear correlation using the k-th order nonlinear filter with $k = 0.3$. A significant peak is observed, normalized to 1 (Figure 3.5D), indicating an authentic image.

Moreover, a false class datasheet is used to authenticate the image, shown in Figure 3.6A. The k-th order nonlinear filter is then used this image as an input with no resultant significant peak indicating a false class image (Figure 3.6B). The output is normalized relative to the output of the nonlinear correlator for a true class image resulting in a maximum peak of 0.03.

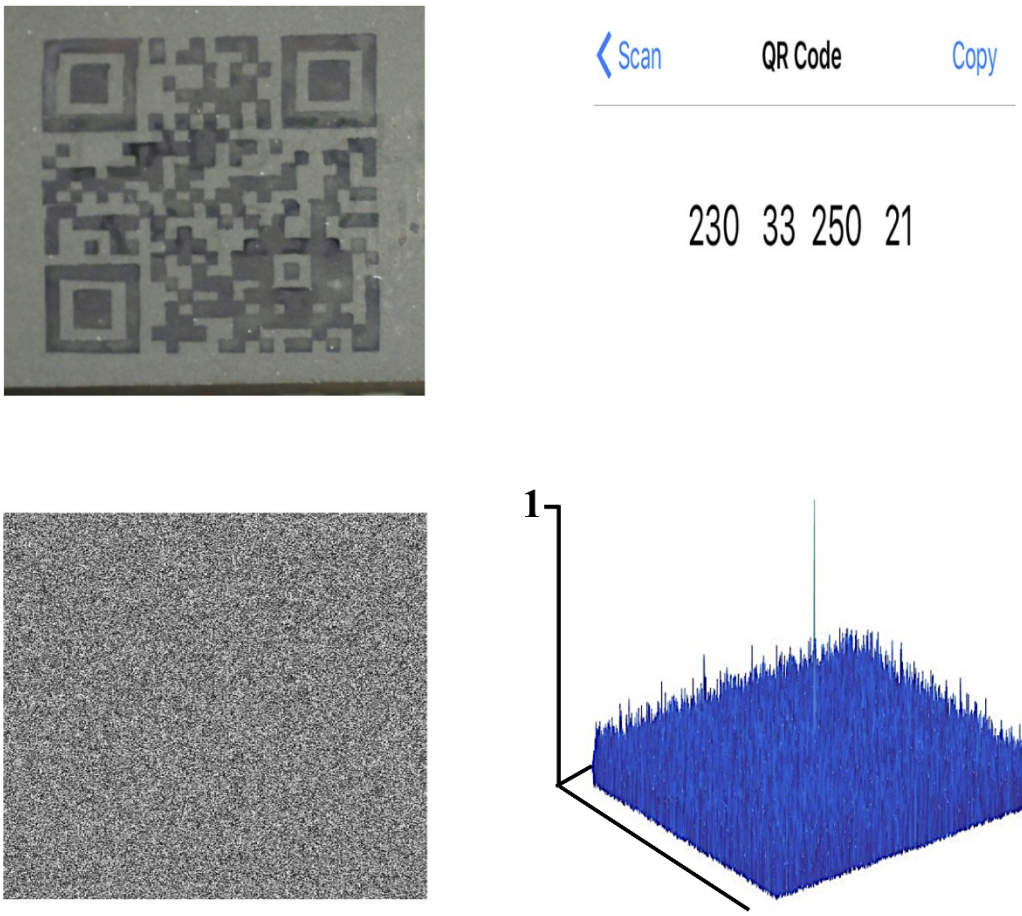

Figure 3.5: (A) Enlarged OPT, denoted as OPT1, printed on an IC and (B) Scanned OPT. (C) Decrypted image followed by (D) Authentication using the *k*-th order nonlinear filter, with *k* = 0.3, normalized to 1.

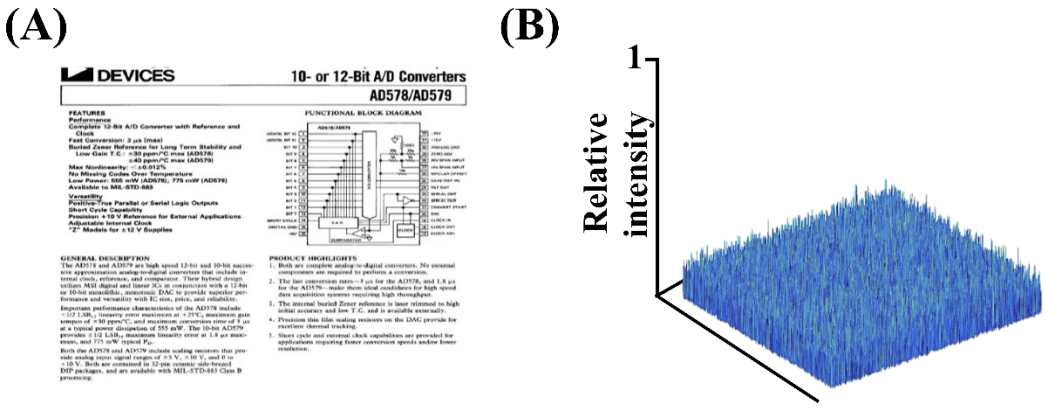

Figure 3.6: (A) False image, a datasheet for an IC of different brand is transformed through the *k*-th order nonlinear filter, with k = 0.3. The image on normalization relative to the true class image peak, gave a maximum peak of 0.03 (B).

3.4.3 Authentication of OPTs with Polarimetry

A typical polarization signature for a true class OPT is shown in Figure 3.7A-D, wherein true class image is the OPT 1 as seen in Figure 3.5A. The Degree of Linear Polarization (DoLP) is also calculated to assess the OPTs fabrication (Figure 3.7E). The average DoLP for true class QR code is 0.5654 with a standard deviation of 0.0459 (Table 3.2). Moreover, the serial number of the IC has an average DoLP of 0.45050 with a standard deviation of 0.0467 and the DoLP of the QR code with Al missing is 0.4634 with a standard deviation of 0.0281 (Table 3.2). These measurements are acquired by segmenting out the OPT, serial number, and Al.

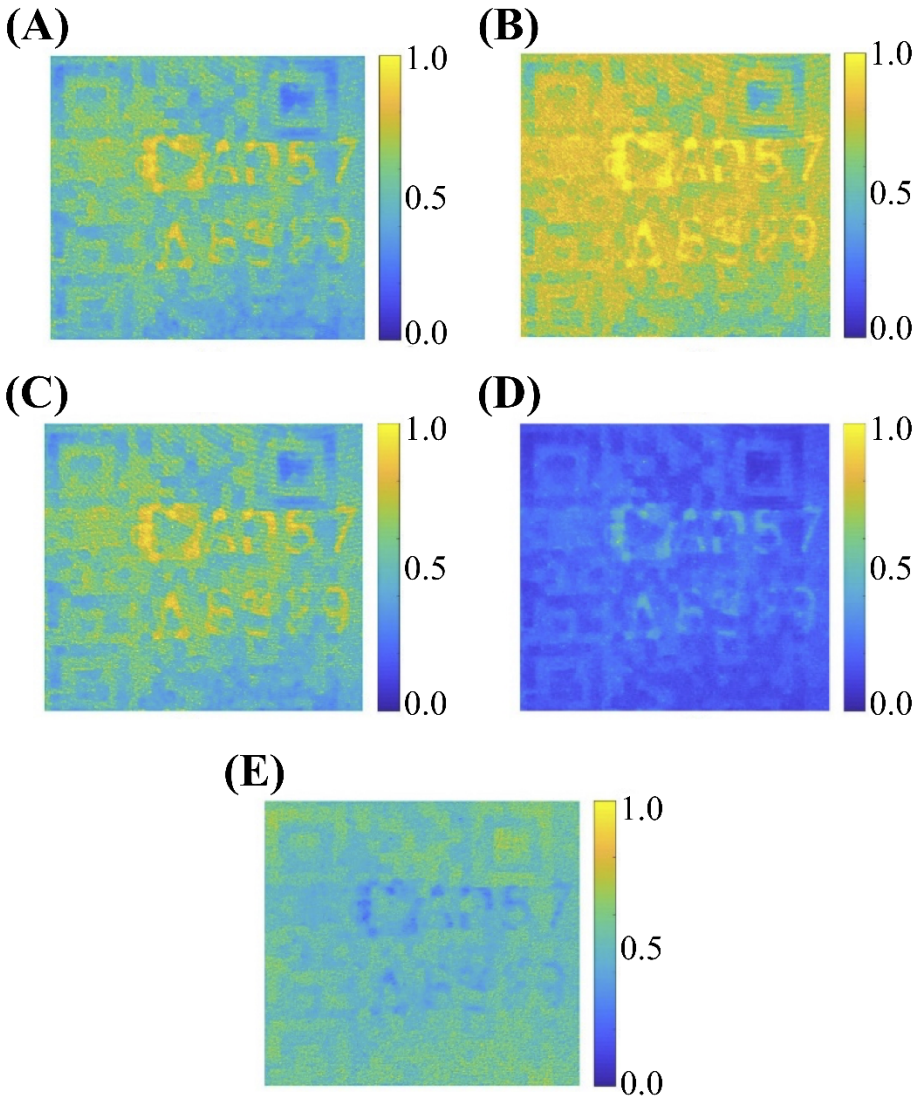

Figure 3.7: Polarimetric readings for OPT 1 corresponding to (A) 0^{o}, (B) 45^{o}, (C) 90^{o}, and (D) 135^{o} of the polarizer. (E) Degree of linear polarization (DoLP) is also imaged.

DoLP image	Average DoLP	Standard deviation
OPT 1	0.5654	0.0459
Serial no. on OPT 1	0.4505	0.0467
Al missing from OPT 1	0.4634	0.0281
OPT 2	0.5671	0.0314
Al missing from OPT 2	0.4199	0.0398
OPT 3	0.5987	0.0539
OPT 4	0.3063	0.0539

Table 3.2: DoLP is studied for an array of true and false class OPTs. Good correlation is found in areas where OPT is correctly printed. DoLP is seen to vary from average value of true class upon damage to or change in printing and handling of the OPT.

False class OPTs are analyzed with polarimetry for comparison: One is partially printed on the non-Al coated IC, another is degraded, and a third is annealed for longer than 1 hr turning the print white (Figure 3.8A,C, and E). The polarimetric signatures for these fabricated OPTs demonstrate the robustness of material inspection for the OPT tag authentication scheme (Figure 3.8B, D, and F). The QR code partially deposited on non-coated IC or OPT 2 has average polarization of the QR code is 0.5671 with a standard deviation of 0.0314 (Table 3.2), despite the absence of serial number in the background (see Figure 3.8B). The top right corner is printed direct on the IC circuit and has an average DoLP of about 0.4199 and standard deviation of 0.0398 (Table 3.2), which differs from the DoLP for an OPT printed on Al coated IC.

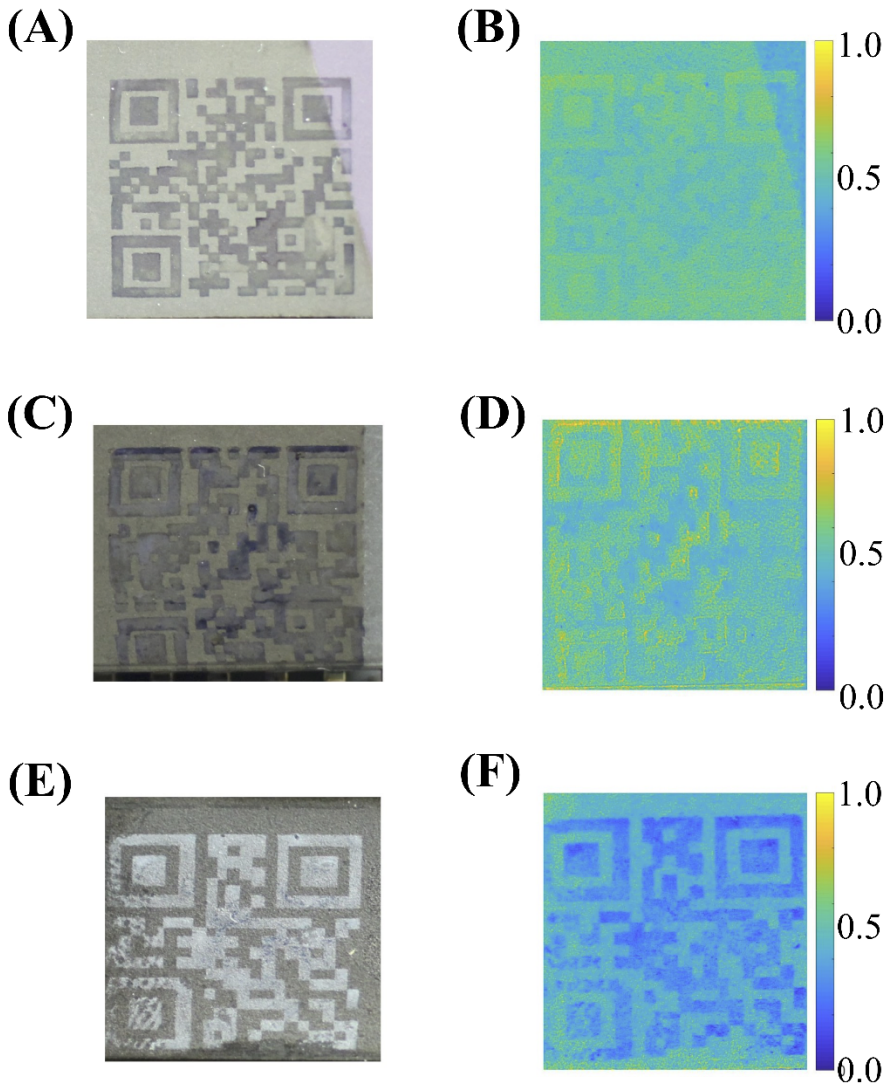

Figure 3.8: Tampered QR codes or "false class" OPTs are compared to OPT 1 as "true class". (A) Partially printed OPT on non Al-coated IC (OPT 2), (B) the DoLP image of OPT 2. (C) A degraded OPT (OPT 3) and (D) its DoLP images are studied. (E) OPT whose color has changed from black to white (OPT 4) and (F) the corresponding DoLP image are also analyzed.

Degraded OPT has average DoLP of 0.5987 with a standard deviation of 0.0539 (Table 3.2). Lastly, OPT with the color changed to white (Figure 3.8E), referred to as OPT 4, has average DoLP is 0.3063 and standard deviation of 0.0539 (Table 3.2). As white is a highly reflective material, the DoLP is highly unpolarized as reflected by the DoLP value.

3.4.4 Authentication with Speckle Pattern

The second part of the classification scheme involves observing the speckle signature of the OPT. Authentication is performed using the *k*-th order nonlinear filter. To evaluate the performance of the system, the peak-to-output energy metric is used. This metric is defined as:

$$\boldsymbol{POE} = \frac{|\boldsymbol{E}[\boldsymbol{y}(\boldsymbol{\tau},\boldsymbol{\tau})]|^{\boldsymbol{2}}}{\boldsymbol{E}\{\overline{[\boldsymbol{y}(\boldsymbol{t},\boldsymbol{\tau})]^{\boldsymbol{2}}}\}}, \tag{1}$$

where POE denotes peak to correlation energy, E[.] denotes expected value, $E[|y(\tau,\tau)|]^2$ denotes the energy of the peak and $E\{\overline{[y(t,\tau)]^2}\}$ denotes the energy of the scene.

Figure 3.9A depicts the speckle signature when OPT 1 (see Figure 3.5A) is illuminated with a green laser diode. Green color channel is used for captured images. The *k*-th order non-linear filter is used for authentication using $k = 0.3$. A significant peak is observed indicating an authentic signature (Figure 3.9B). Note that the output is normalized to 1. Moreover, the POE is 2434. A false class speckle signature is inputted into the system, shown in Figure 3.9C, obtained from OPT 2 (Figure 3.6A). The output of the correlator shows no significant peak and the POE is significantly lower with a value of 0.6504 (Figure 3.9D).

The classification is also examined with x-axis translation, wherein object is moved ±5 mm in the x-direction. The resulting change in POE shows a single maxima at a

0 mm translation, and steadily decreases when moved in either direction (data not shown). A practical implication of this study is that the distance of the CCD is from the object is important. As the CCD is further from the object, it is less sensitive to translation.[14]

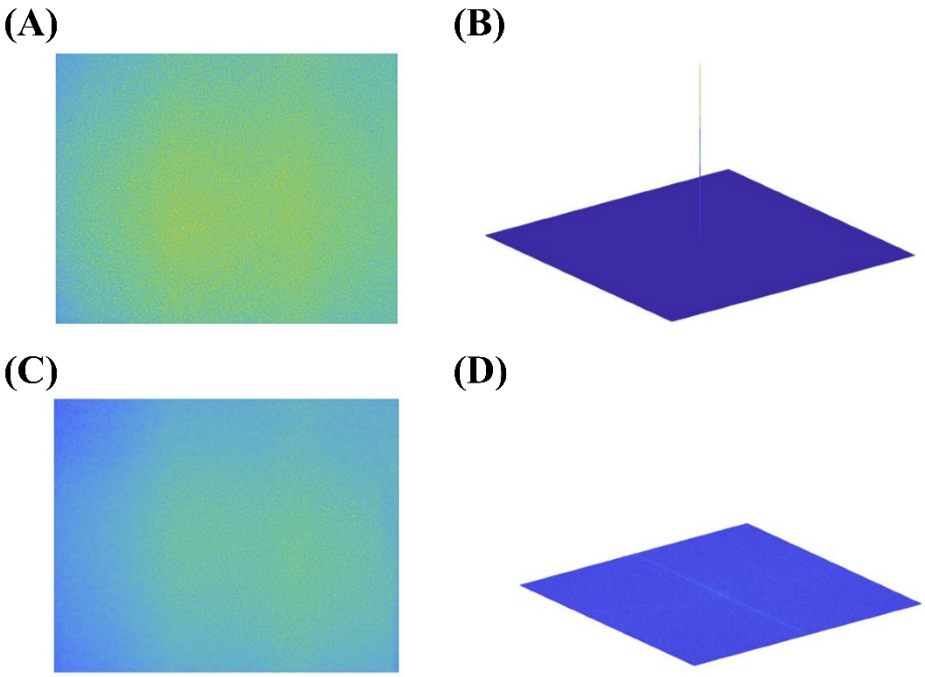

Figure 3.9: (A) True class speckle signature obtained from OPT and (B) its authenticated pattern using the *k*-th order nonlinear filter with k = 0.3, normalized to relative intensity of 1. (C) False class optical signature pattern and (D) corresponding authenticated signal. Observed values for correlator function for true class = 1 and false class = 0.04.

3.5 Discussion

A robust fabrication and authentication method has been achieved with the current protocol of inkjet printing ZnO nanoparticles as a QR code on Al-coated ICs. The multi-step authentication process proves useful in eliminating even minor damages or changes in the fabrication process. The first point of inspection is the visual examination and scanning of the QR code. Damaged or worn off QR codes cannot be scanned successfully (Figure 3.10), such is the case of OPT 3 (Figure 3.8C). However, QR codes not printed fully Al-coated ICs or OPT 2 (Figure 3.8A) or those that have turned white due to prolonged annealing or OPT 4 (Figure 3.8E) will still pass visual examination and scanning step (Figure 3.10). Thus, QR code scan alone is not able differentiate OPTs with minor non-conformance in the inkjet printing.

The next authentication step includes analysis by polarimetry and computation of Stokes parameters and DoLP. This step enhances the authentication process by analyzing QR code's material composition. It will pass QR codes that are printed by ZnO material and have similar deposition and physical appearance. Thus OPT 3 and OPT 4 will not pass inspection, however OPT 2 will as large portion of the QR code is printed on the Al-coated IC (see Figure 3.10).

The final step in the authentication protocol measures speckle signature, which is indicative of surface roughness. As the Al-coating on the IC would contribute to overall surface roughness, this step is able to distinguish true image OPT 1 from false image of OPT 2 (Figure 3.10). Moreover, any other errors during the fabrication process will similarly fail the speckle signature authentication. Thus a simple and efficient authentication protocol is for inkjet printed ZnO nanoparticle optical phase tags.

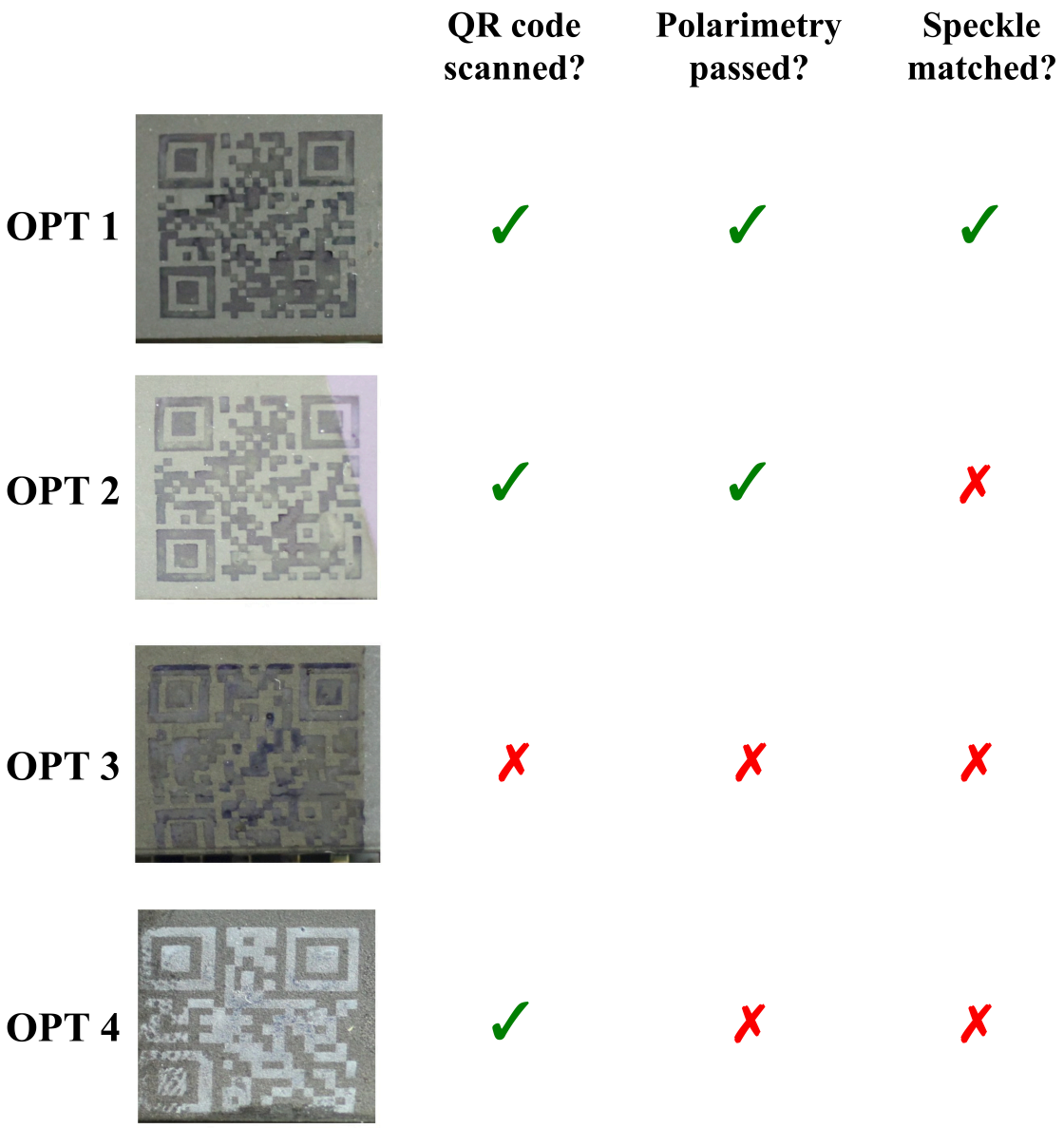

Figure 3.10: Summary of authentication process for inkjet printed OPTs on Al-coated ICs. Physical appearance, damage to the print, change in annealing process, and other non-conforming QR codes will be deemed false class using the chosen authentication process.

3.6 Conclusion

A secure object authentication system has been presented that involves placing a unique optical phase tag (OPT), comprised of inkjet deposited ZnO nanoparticles on Al-coated integrated circuits. Moreover, the tag takes the form of a QR code, which stores critical information about an object, such as the data sheet. The authentication process has two major components: First step consists of material inspection and determining that the OPT has not been altered, changed or tampered. This is accomplished by illuminating the QR code with a coherent light source, and computing the Stokes parameters along with the degree of linear polarization. The next step is speckle authentication by illuminating the OPT with a coherent light source and capturing the reflected light, which is then authenticated using nonlinear correlation. The proposed technique is able to differentiate true class OPTs from false class. Future work includes creating a more compact system, different authentication algorithms, and OPTs consisting of more complex materials.

3.7 References

(1) Mackey, T. K.; Liang, B. A.; York, P.; Kubic, T. Counterfeit Drug Penetration into Global Legitimate Medicine Supply Chains: A Global Assessment. *Am. J. Trop. Med. Hyg.* **2015**, *92* (Suppl 6), 59–67.

(2) World Health Organization. A Study on the Public Health and Socioeconomic Impact of Substandard and Falsified Medical Products; Geneva, 2017.

(3) Guin, U.; DiMase, D.; Tehranipoor, M. Counterfeit Integrated Circuits: Detection, Avoidance, and the Challenges Ahead. *J. Electron. Test.* **2014**, *30* (1), 9–23.

(4) Counterfeit Parts: Increasing Awareness and Developing Countermeasures, 2011. Aerospace Industries Association Web Site. https://www.aia-aerospace.org/report/counterfeit-parts-increasing-awareness-and-developing-countermeasures/ (accessed May 15, 2018).

(5) Chardonnal, D. Global impacts of counterfeiting and piracy to reach US$4.2 trillion by 2022, 2017. International Chamber of Commerce Web Site. https://iccwbo.org/media-wall/news-speeches/global-impacts-counterfeiting-piracy-reach-us4-2-trillion-2022/ (accessed May 15, 2018).

(6) Global Counterfeit Money Detection Market to Value $5.3 Billion by 2025 - Industry Forecast & Analysis - Research and Markets, 2017. Business Wire Web Site. https://www.businesswire.com/news/home/20170323005654/en/Global-Counterfeit-Money-Detection-Market-5.3-Billion (accessed May 15, 2018).

(7) Tuyls, P.; Batina, L. RFID-Tags for Anti-Counterfeiting. *Lect. Notes Comput. Sci.* **2006**, *3860*, 115–131.

(8) Markman, A.; Javidi, B.; Tehranipoor, M. Photon-Counting Security Tagging and Verification Using Optically Encoded QR Codes. *IEEE Photonics J.* **2014**, *6* (1), 1–9.

(9) Carnicer, A.; Arteaga, O.; Suñé-Negre, J. M.; Javidi, B. Authentication of Gold Nanoparticle Encoded Pharmaceutical Tablets Using Polarimetric Signatures. *Opt. Lett.* **2016**, *41* (19), 4507–4510.

(10) Devadas, S.; Suh, E.; Paral, S.; Sowell, R.; Ziola, T.; Khandelwal, V. Design and Implementation of PUF-Based "Unclonable" RFID ICs for Anti-Counterfeiting and Security Applications. In *2008 IEEE International Conference on RFID*; IEEE: Las Vegas, NV, 2008; pp 58–64.

(11) Romero, H. P.; Remley, K. A.; Williams, D. F.; Wang, C. M. Electromagnetic Measurements for Counterfeit Detection of Radio Frequency Identification Cards. *IEEE Trans. Microw. Theory Tech.* **2009**, *57* (5), 1383–1387.

(12) Carnicer, A.; Arteaga, O.; Pascual, E.; Canillas, A.; Vallmitjana, S.; Javidi, B.; Bertran, E. Optical Security Verification by Synthesizing Thin Films with Unique Polarimetric Signatures. *Opt. Lett.* **2015**, *40* (22), 5399–5402.

(13) Carnicer, A.; Hassanfiroozi, A.; Latorre-Carmona, P.; Huang, Y.-P.; Javidi, B. Security Authentication Using Phase-Encoded Nanoparticle Structures and Polarized Light. *Opt. Lett.* **2015**, *40* (2), 135–138.

(14) Markman, A.; Carnicer, A.; Javidi, B. Security Authentication with a Three-Dimensional Optical Phase Code Using Random Forest Classifier. *J. Opt. Soc. Am. A* **2016**, *33* (6), 1160–1165.

(15) Kelly, K. L.; Coronado, E.; Zhao, L. L.; Schatz, G. C. The Optical Properties of Metal Nanoparticles: The Influence of Size, Shape, and Dielectric Environment. *J. Phys. Chem. B* **2003**, *107* (3), 668–677.

(16) Flory, F.; Escoubas, L.; Berginc, G. Optical Properties of Nanostructured Materials: A Review. *J. Nanophotonics* **2011**, *5* (1), 052502.

(17) Djurišić, A. B.; Leung, Y. H. Optical Properties of ZnO Nanostructures. *Small* **2006**, *2* (8–9), 944–961.

(18) Zak, A. K.; Abrishami, M. E.; Majid, W. H. A.; Yousefi, R.; Hosseini, S. M. Effects of Annealing Temperature on Some Structural and Optical Properties of ZnO Nanoparticles Prepared by a Modified Sol–Gel Combustion Method. *Ceram. Int.* **2011**, *37* (1), 393–398.

(19) Kahouli, M.; Barhoumi, A.; Bouzid, A.; Al-Hajry, A.; Guermazi, S. Structural and Optical Properties of ZnO Nanoparticles Prepared by Direct Precipitation Method. *Superlattices Microstruct.* **2015**, *85*, 7–23.

(20) You, M.; Lin, M.; Wang, S.; Wang, X.; Zhang, G.; Hong, Y.; Dong, Y.; Jin, G.; Xu, F. Three-Dimensional Quick Response Code Based on Inkjet Printing of Upconversion Fluorescent Nanoparticles for Drug Anti-Counterfeiting. *Nanoscale* **2016**, *8* (19), 10096–10104.

(21) Edinger, M.; Bar-Shalom, D.; Sandler, N.; Rantanen, J.; Genina, N. QR Encoded Smart Oral Dosage Forms by Inkjet Printing. *Int. J. Pharm.* **2018**, *536* (1), 138–145.

(22) Goodman, J. W. *Statistical Optics*, Wiley Classics ed.; John Wiley & Sons, Inc.: Toronto, 2000.

(23) Wang, C.-T.; Huang, K.-Y.; Lin, D. T. W.; Liao, W.-C.; Lin, H.-W.; Hu, Y.-C. A Flexible Proximity Sensor Fully Fabricated by Inkjet Printing. *Sensors* **2010**, *10* (5), 5054–5062.

(24) Collett, E. *Field Guide to Polarization*; SPIE: Bellingham, WA, 2005.

(25) Born, M.; Wolf, E. Principles of Optics : Electromagnetic Theory of Propagation, Interference and Diffraction of Light, 7th ed.; Cambridge University Press: Cambridge, 1999.

(26) Yeh, C.-H.; Lee, G.; Lin, C.-Y. Robust Laser Speckle Authentication System through Data Mining Techniques. *IEEE Trans. Ind. Informatics* **2015**, *11* (2), 505–512.

(27) *Laser Speckle and Related Phenomena*, 2nd ed.; Dainty, J. C., Ed.; Springer-Verlag Berlin Heidelberg: Berlin, 1975.

(28) Demos, S. G.; Alfano, R. R. Optical Polarization Imaging. *Appl. Opt.* **1997**, *36* (1), 150–155.

(29) Javidi, B. Nonlinear Joint Power Spectrum Based Optical Correlation. *Appl. Opt.* **1989**, *28* (12), 2358–2367.

Chapter 4

Inkjet Printed Electrochemical Sensor from a Novel Bronze Material and Multi-well Catalytic Reactor with Sol-gel Manganese Oxide Structures

4.1 Abstract

In this chapter, two applications of inorganic materials are explored: In part one, an electrochemical sensor is designed with a novel bronze ink and in part two, a design for 3D printed multiplexed catalytic reactor is proposed. First, The bronze material is inkjet printed into an 8-electrode system that can facilitate fabrication of disposable electrochemical sensors. The 8-electrode design further enhances multiplexing capabilities by analyzing multiple analytes simultaneously. Future work will include characterization of the surface of electrodes and their electrochemical performance, and surface attachment of protein or antibodies for applications in biomarker detection. Secondly, a 3D printed catalytic reactor is designed to create wells similar to a 96-well plate, each of which can carry out electrocatalysis. The design incorporates a base plate, a counter electrode, a reference electrode, and inkjet printed manganese oxide. Future work includes printing and assembling the device and testing with common catalytic reactions, such as oxidation of alcohols.

Part I:

Inkjet Printed Electrochemical Sensor from a Novel Bronze Material

4.2 Introduction

A variety of conductive inks are applied to the fabrication of inkjet printed electronics, including conductive polymers, molten metal, metal precursors, and metal nanoparticles.[1–3] Non-ambient printing conditions and post-print sintering at high temperatures make molten metal or metal precursor inks inefficient for manufacturing flexible electronics.[2] Metal nanoparticles are often the best choice for conductive inks, due to room or low temperature printing and better conductivity than conductive polymers; however require some processing to form uniform, conductive lines.[2,4]

An array of flexible electronics has been manufactured with inkjet printing, from single layer connectors,[3,5,6] transistor and other components,[7] to full multi-layer fabrication of a solar cell or a device.[8–10] Advances in nanoparticle synthesis and printing methodology has reduced width of conductive ink tracks to < 25 μm, significantly allowing fabrication of smaller devices.[6,11] Gold particles, 2-5 nm sized, are printed in a toluene solution for conductive tracks as narrow as 17 μm with laser sintering.[11] Carbon nanotubes are also employed for conductive patterns in a water suspension and without post-print processing.[12] Narrow (~ 40 μm) silver conductive tracks are inkjet printed by van Osch et al[13] using 30 nm silver nanoparticles, with easier thermal sintering process. Our research group inkjet prints thiol gold nanoparticles 8-electrode arrays, that are successfully used as biosensors for detection of protein cancer biomarkers.[14,15]

Gas sensors have also been developed by inkjet deposition of the sensing element, the electrodes, or even the entire sensor.[16–18] Kukkola et al. fabricated tungsten based resistive and capacitive sensors for nitric oxide and hydrogen gas respectively by depositing the tungsten inks on silicon substrates with interdigitated platinum electrodes.[16] Fang et al improved the sensitivity of a carbon nanotube-modified Kapton resistive diethyl ethylphosphonate sensor by chemical processing of inkjet printed silver interdigitated electrodes.[19] The silver electrodes are partially replaced by porous gold layer on chemical treatment, producing a sensor with 5 times more sensitivity.

More recently, efforts are directed towards producing fully inkjet printed sensor surface.[20–24] In 2010, Wang et al designed a heat sensor by printing layer of sol-gel zinc oxide solution and of the top silver electrode on a flexible aluminum sheet as the bottom electrode.[20] The oscilloscope connected to the system registers a voltage output on introduction of proximal heat source, providing an inkjet printed disposable heat sensor. Since then, a sol-gel based tin oxide sensor, a copper oxide sensor for carbon monoxide, and a copper acetate sensor for H_2S are also developed entirely with inkjet printing.[22–24]

4.3 Experimental

4.3.1 Chemicals and Instruments

2-hydroxyethyl cellulose, ethylene glycol (EG, $(CH_2OH)_2$), ethanol (EtOH, CH_3OH), and Tween-20 are purchased from Sigma-Aldrich (St. Louis, MO, USA). 18 MΩ·cm purified water (H_2O) is used as needed, by passing house-distilled water through a Hydro Service and Supplies purification system (Durham, NC, USA). Precursor mixture and final bronze product

is provided Suib group, UConn.[25] Inkjet printing is performed with Dimatix DMP-2800 printer (Fujifilm Dimatix, CA, USA). Surface tension measurements are made with Pendant Drop Tensiometer OCA 20 (Future Digital Scientific Corp., NY, USA) and viscosity measurements with ARES-G2 (TA instruments, DE, USA).

4.3.2 Ink and Substrate Optimization

Two inks, of either the precursors or the final bronze product, are optimized in EG/EtOH or H_2O/EG solvent systems to achieve viscosity of 10-12 cP, surface tension of 28-33 dyne/cm, and concentration of 100 mg ml^{-1}. The bronze product ink is more suitable for printing and post-print processing, with final solvent composition at 1:2 H_2O:EG. To stabilize the colloidal solution, the bronze nanoparticles in H_2O/EG solution are sonicated for 4 hours after addition of 1% w/v 2-hydroxyethyl cellulose. The ink is filtered through 0.2 mm filter prior to inkjet printing.

4.3.3 Fabrication of Immunoarray Sensor

8-electrode arrays are printed with micro sensing area and contact pads as previous published and are sintered at 200 °C for 2 hours (Figure 4.1).[14] Briefly, a clean 22 cm x 28 cm Kapton sheet is placed in the Dimatix printer and platen vacuum is applied. Ink cartridge is filled with the bronze ink solution and waveform is customized till consistent ink droplets were formed. The pattern file is set to allow for printing multiple arrays in a single print, with varying spacing between arrays. The bronze nanoparticle ink is deposited onto the Kapton substrate as a single layer and the arrays were heated to 200 °C for 2 hrs until the films changed color.

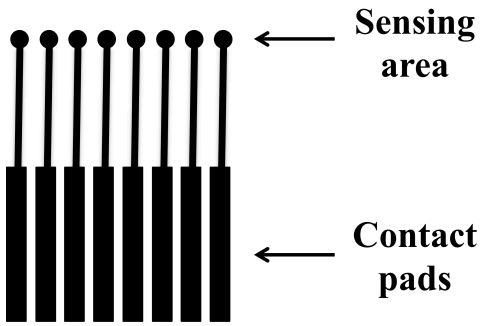

Figure 4.1: Pattern for 8-electrode electrochemical array.

4.4 Results and Discussion

Precursors inks are better stabilized in the ink solvent and printed on porcelain chips to assist with the required high temperature chemical reaction. Upon baking at 600 °C for 2 hrs, the correct final product is not formed: Unequal jetting ratio of the three precursors may be responsible for this outcome. Hence, bronze colloidal solution is used as the conductive ink in 1:2 H_2O:EG solution. The print however is not consistent and printing cartridges were continuously blocked. Scanning electron microscopy is performed on the ink from a blocked cartridge (Figure 4.2); showing highly crystalline cubic structures > 200 nm in size. As this size exceeds the printing capabilities of the Dimatix printer, further ink processing for size reduction and better colloidal formation is required. The ink is then prepared in 1:2 H_2O:EG solution with 1% w/v 2-hydroxylethyl cellulose and sonicated at room temperature for 4 hrs. The ink is filtered through 0.2 μm filter prior to printing. While better print quality is observed, the ink still separates within 1 hr of preparation, making more optimization necessary.

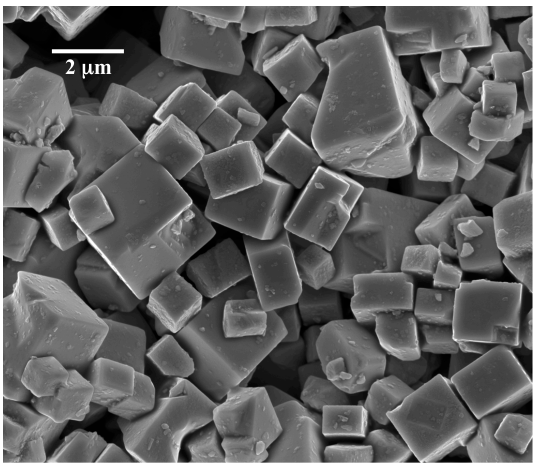

Figure 4.2: SEM of bronze product on printing without sonication. The size observed for the highly crystalline cubic structures is > 200 nm, thus being unsuitable for printing.

4.5 Conclusion

The bronze product proves to have better printing efficiency than the precursor mixture, although a stable colloidal solution of requisite size (< 200 nm) is yet to be consistently obtained. More ink optimization is required prior to printing electrodes. Once printed, electrodes will need to be characterized for surface area, morphology, electrochemically active area, conductance, etc. Further studies will decide a surface modification method for any applications as a biosensor.

Part II:

Multi-well Catalytic Reactor with Sol-gel Manganese Oxide Structures

4.6 Introduction

4.6.1 3D Printing Techniques

3D printing fabrication is achieved by layer-by-layer assembly of materials to form a three dimensional structures. Numerous free and licensed software are available for designing models, such as 123design, CAD, and computer-assisted splicing of these models into layers.[26] Existing 3D printing methodologies predominantly employ deposition such as in Fused Deposition Modeling (or FDM), and/or curing of materials, like Stereolithography (or SLA), either in pure form or with additives that improve functionality of such materials.[26,27] Combinations of the two methods are also commercially available in Inkjet 3D Printing (3DP), Selective Laser Sintering (SLS), and Direct-write/ 3D plotting type 3D printers.[26]

In Fused Deposition Modeling (FDM), a self-fusing, thermo-setting polymeric material, as a heated filament, is extruded in layers in FDM printers, much like the inkjet printers previously discussed. The most common filament materials are low-melting polymers, such as polycarbonate (PC), polylactic acid (PLA), acrylonitrile butadiene styrene (ABS). A low-cost option for 3D printing, this technique can print multiple filaments simultaneously provides capability of printing complex structures with required functionalities. While fast-paced, simple, and having good structural strength, resolution and inaccuracy in printing makes FDM cumbersome.

2D layers are built by curing a photopolymer, such as epoxy or acrylic resins in Stereolithography (SLA). As a UV laser tracks a pattern on the printing platform, the resin polymerizes to form the layer. Following this curing method, platform is layered with fresh resin used to print the next layer. SLA provides very high-resolution prints, which can be made transparent by post-print treatment. Several parameters, such as rate of scanning, intensity of the laser, exposure time, addition of curing agents can affect thickness of individual layers, resolution and printing speeds. The main drawbacks of this technique are cost, and lower speeds of printing.

Much like SLA, Inkjet 3D printing or 3DP is achieved by layer-by-layer curing. However, in 3DP, a powder is spread on printing platform, which is cured by inkjet deposition of a liquid binder to form the layer pattern. The cycle is repeated to yield the final model and the uncured powder is easily removed. Selection of powder and binder is key to achieving high quality prints. A fast printing method, 3DP can be performed at room temperature with versatile materials, although with low resolution.

Selective laser sintering (SLS) uses powder processing as in 3DP, however the binder is replaced with a laser beam for curing. High power lasers generate localized heat, fusing together powder particles. Most of the advantages of 3DP carry over to SLS, however the printing technique is limited to select thermosetting plastics. Only polycaprolactone (PCL) and polyamide (PA) have been successfully used for SLS printing. Additionally, parameters such as powder size, laser power, speed and spacing of scans control resolution.

3D plotting or direct-write employs a pressurized syringe to deposit viscous printing material in layers, as the syringe moves in X-Y-Z direction. Mixing two reactive materials prior to extrusion, heat, or UV light are typical curing methods. Quality of prints is affected by speed

of printing and material rheology. 3D plotting can be used with flexible materials, used in solution, paste, or hydrogel form. Temporary structure support may be needed to aid initial printing, before structural strength is achieved.

4.6.2 Printed Catalytic Systems

A few inkjet printing applications have been developed for fabrication of structures for improved catalytic efficiency. Busato et al[28] deposited palladium catalyst on polyimide films to assist fabrication of interdigitated copper electrodes. Picoleter volumes of platinum catalyst was inkjet printed as membrane electrode assemblies by Taylor et al.[29] A high throughput system for building catalytic libraries was designed by Liu and coworkers, which measure hydrogen evolution at different catalytic zones for compilation of activity data.[30] Micro-channel reactors with inkjet printed nanoparticle-based catalysts are also fabricated and successfully used in methane steam reforming reaction.[31]

3D printing has been incorporated into catalytic systems as mainly reactionware.[32–34] Symes et al[32] "printed in" catalyst layer into the 3D printed reactionware, by loading the printing polymer with a paste of palladium and carbon. They were successful in hydrogenating styrene at room temperature within 30 mins, while the reaction without the catalyst showed no product in 2 hrs. Kitson et al[34] improved this design by a customized microfluidic build up, with catalytic chambers for specific reactions in a 3-step reaction, using both montmorillonite K10 Lewis acid and palladium/carbon paste as catalyst. Other works have directly 3D printed the catalytic mixture into the shape optimized for reaction chamber, such as the "woodpile" structure from copper/aluminum oxide ink[35].

4.7 Experimental

4.7.1 Chemicals and Instruments

Toluene is purchased from Sigma-Aldrich (St. Louis, MO, USA). Inkjet printing is performed with Dimatix DMP-2800 printer (Fujifilm Dimatix, CA, USA). Surface tension measurements are made with Pendant Drop Tensiometer OCA 20 (Future Digital Scientific Corp., NY, USA) and viscosity measurements with ARES-G2 (TA instruments, DE, USA). Manganese oxide catalysts are provided by Suib group, UConn.

4.7.2 Inkjet Printing of Manganese Oxides

Manganese oxide catalysts, in particular, M-150, M-350, Mn_2O_3, are solubilized in toluene to achieve viscosity of 8-10 cP, surface tension of ~ 28 dyne/cm, and nanoparticle concentration of 100 mg ml^{-1}. The ink is filtered through 0.2 mm filter prior to inkjet printing. A simple rectangular block pattern is printed on Kapton sheet to test print quality and adhesion to Kapton. Both are found to be reliably consistent.

4.8 Design of Catalytic Reactor

The catalytic reactor designed will mimic a 96-well plate used for high-throughput UV/Vis analysis (Figure 4.3). 3D printing will be used to fabricate the bottom plate and the well edges for the 96-well plate. Sandwiched between the two 3D printed components will be the catalytic structure. The substrate for the inkjet printed catalyst patterns will be polyamide film or similar inert polymeric film. If electrocatalysis is to be performed, a counter and reference electrodes can be inkjet printed using commercially available silver and platinum ink

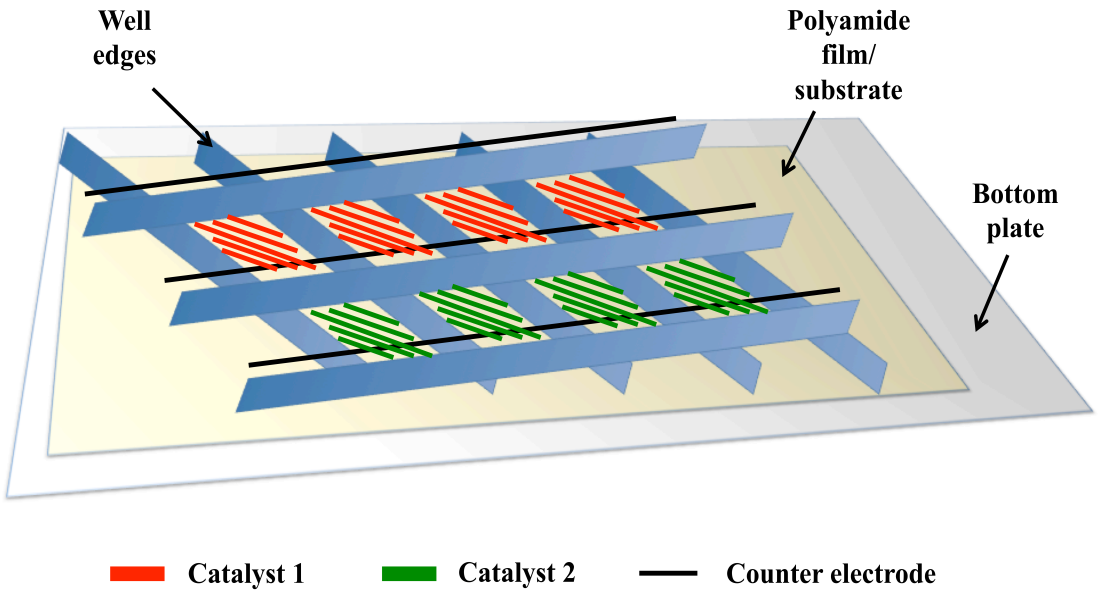

Figure 4.3: Schematic of a high-throughput multi-well catalytic reactor includes inkjet printed catalyst structures sandwiched and sealed between 3D printed bottom plate and well edges.

respectively, with appropriate contact pads for connections to an electrochemical workstation. No electrodes will be required if normal catalytic reaction is observed.

The catalytic structures within each well can be custom designed for an array of catalysts under study, with each row or column dedicated to a single catalyst or a single reaction, etc. Inkjet printing patterns can be developed to optimize surface morphology of such catalysts, by a combination of patterns as illustrated in Figure 4.4. Wells with low or high surface area for a single catalyst can be designed (see Figure 4.4A-C). Two or more catalysts can also be printed in combination, with low (Figure 4.4D) or high (Figure 4.4E) overlap between the two catalysts.

The added benefit of such a system is the ability to conduct both regular and electrochemical catalysis. The well-plate format can be designed to suit specifications for a UV/Vis plate reader and thus can allow monitoring of the reaction by change in UV/Vis absorbance of reactants or products. The plate can also then suit parameters for robotic arm systems used for ELISA automation - ensuring progress to fully automated system for building catalysis libraries for a range of compounds.

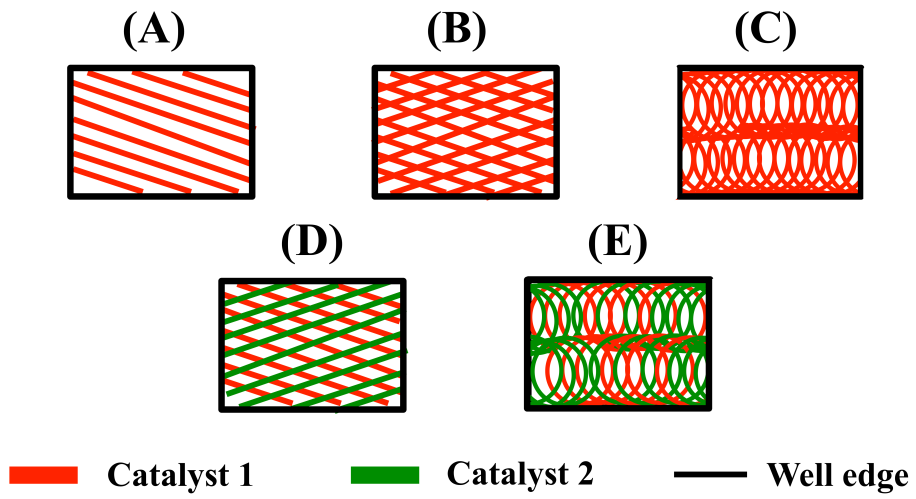

Figure 4.4: Catalytic patterns can be customized for each well: (A) single catalyst, low surface area, (B) single catalyst, medium surface area, (C) single catalyst, high surface area, (D) two catalysts, low overlap area, and (E) two catalysts, high overlap area.

4.9 Conclusions

An integrated inkjet and 3D printed device for high-throughput catalysis is designed, a proof of concept study is presented with manganese oxide sol-gel materials as catalysts. The future work will include printing and assembling this device, upon which simple catalytic reactions can be screened for a prototype study. The design, upon completion, can provide a unique reactor that allows microliter sized reactions and easy analysis by UV-Vis for building catalysis library for the inkjet printed catalytic systems.

4.10 References

(1) Rajan, K.; Bocchini, S.; Chiappone, A.; Roppolo, I.; Perrone, D.; Bejtka, K.; Ricciardi, C.; Pirri, C. F.; Chiolerio, A. Spin-Coated Silver Nanocomposite Resistive Switching Devices. *Microelectron. Eng.* **2017**, *168*, 27–31.

(2) Calvert, P. Inkjet Printing for Materials and Devices. *Chem. Mater.* **2001**, *13* (10), 3299–3305.

(3) Lee, H.-H.; Chou, K.-S.; Huang, K.-C. Inkjet Printing of Nanosized Silver Colloids. *Nanotechnology* **2005**, *16* (10), 2436–2441.

(4) Wünscher, S.; Abbel, R.; Perelaer, J.; Schubert, U. S. Progress of Alternative Sintering Approaches of Inkjet-Printed Metal Inks and Their Application for Manufacturing of Flexible Electronic Devices. *J. Mater. Chem. C* **2014**, *2* (48), 10232–10261.

(5) Perelaer, J.; Hendriks, C. E.; de Laat, A. W. M.; Schubert, U. S. One-Step Inkjet Printing of Conductive Silver Tracks on Polymer Substrates. *Nanotechnology* **2009**, *20* (16), 165303.

(6) Bieri, N. R.; Chung, J.; Haferl, S. E.; Poulikakos, D.; Grigoropoulos, C. P. Microstructuring by Printing and Laser Curing of Nanoparticle Solutions. *Appl. Phys. Lett.* **2003**, *82* (20), 3529–3531.

(7) Yan, H.; Chen, Z.; Zheng, Y.; Newman, C.; Quinn, J. R.; Dötz, F.; Kastler, M.; Facchetti, A. A High-Mobility Electron-Transporting Polymer for Printed Transistors. *Nature* **2009**, *457* (7230), 679–686.

(8) Ko, S. H.; Pan, H.; Grigoropoulos, C. P.; Luscombe, C. K.; Fréchet, J. M. J.; Poulikakos, D. All-Inkjet-Printed Flexible Electronics Fabrication on a Polymer Substrate by Low-

Temperature High-Resolution Selective Laser Sintering of Metal Nanoparticles. *Nanotechnology* **2007**, *18* (34), 345202.

(9) Hoth, C. N.; Schilinsky, P.; Choulis, S. A.; Brabec, C. J. Printing Highly Efficient Organic Solar Cells. *Nano Lett.* **2008**, *8* (9), 2806–2813.

(10) Singh, M.; Haverinen, H. M.; Dhagat, P.; Jabbour, G. E. Inkjet Printing-Process and Its Applications. *Adv. Mater.* **2010**, *22* (6), 673–685.

(11) Bieri, N. R.; Chung, J.; Poulikakos, D.; Grigoropoulos, C. P. Manufacturing of Nanoscale Thickness Gold Lines by Laser Curing of a Discretely Deposited Nanoparticle Suspension. *Superlattices Microstruct.* **2004**, *35* (3–6), 437–444.

(12) Kordás, K.; Mustonen, T.; Tóth, G.; Jantunen, H.; Lajunen, M.; Soldano, C.; Talapatra, S.; Kar, S.; Vajtai, R.; Ajayan, P. M. Inkjet Printing of Electrically Conductive Patterns of Carbon Nanotubes. *Small* **2006**, *2* (8–9), 1021–1025.

(13) van Osch, T. H. J.; Perelaer, J.; de Laat, A. W. M.; Schubert, U. S. Inkjet Printing of Narrow Conductive Tracks on Untreated Polymeric Substrates. *Adv. Mater.* **2008**, *20* (2), 343–345.

(14) Jensen, G. C.; Krause, C. E.; Sotzing, G. A.; Rusling, J. F. Inkjet-Printed Gold Nanoparticle Electrochemical Arrays on Plastic. Application to Immunodetection of a Cancer Biomarker Protein. *Phys. Chem. Chem. Phys.* **2011**, *13* (11), 4888–4894.

(15) Krause, C. E.; Otieno, B. A.; Latus, A.; Faria, R. C.; Patel, V.; Gutkind, J. S.; Rusling, J. F. Rapid Microfluidic Immunoassays of Cancer Biomarker Proteins Using Disposable Inkjet-Printed Gold Nanoparticle Arrays. *ChemistryOpen* **2013**, *2* (4), 141–145.

(16) Kukkola, J.; Jansson, E.; Popov, A.; Lappalainen, J.; Mäklin, J.; Halonen, N.; Tóth, G.; Shchukarev, A.; Mikkola, J.-P.; Jantunen, H.; et al. Novel Printed Nanostructured Gas Sensors. *Procedia Eng.* **2011**, *25*, 896–899.

(17) Sarfraz, J.; Fogde, A.; Ihalainen, P.; Peltonen, J. The Performance of Inkjet-Printed Copper Acetate Based Hydrogen Sulfide Gas Sensor on a Flexible Plastic Substrate - Varying Ink Composition and Print Density. *Appl. Surf. Sci.* **2018**, *445*, 89–96.

(18) Liu, Y.; Xu, X.; Chen, Y.; Zhang, Y.; Gao, X.; Xu, P.; Li, X.; Fang, J.; Wen, W. An Integrated Micro-Chip with Ru/Al2O3/ZnO as Sensing Material for SO2 Detection. *Sensors Actuators B Chem.* **2018**, *262*, 26–34.

(19) Fang, Y.; Akbari, M.; Hester, J. G. D.; Sydänheimo, L.; Ukkonen, L.; Tentzeris, M. M. Sensitivity Enhancement of Flexible Gas Sensors via Conversion of Inkjet-Printed Silver Electrodes into Porous Gold Counterparts. *Sci. Rep.* **2017**, *7* (1), 8988.

(20) Wang, C.-T.; Huang, K.-Y.; Lin, D. T. W.; Liao, W.-C.; Lin, H.-W.; Hu, Y.-C. A Flexible Proximity Sensor Fully Fabricated by Inkjet Printing. *Sensors* **2010**, *10* (5), 5054–5062.

(21) Marzęcki, M.; Jachowicz, R.; Tarapata, G. Multilayer Inkjet Printed Dew Point Hygrometer. *Sensors Actuators B Chem.* **2018**, *264*, 76–83.

(22) Rieu, M.; Camara, M.; Tournier, G.; Viricelle, J.-P.; Pijolat, C.; de Rooij, N. F.; Briand, D. Fully Inkjet Printed SnO2 Gas Sensor on Plastic Substrate. *Sensors Actuators B Chem.* **2016**, *236*, 1091–1097.

(23) Pashchanka, M.; Prasad, R. M.; Hoffmann, R. C.; Gurlo, A.; Schneider, J. J. Inkjet-Printed Nanoscaled CuO for Miniaturized Gas-Sensing Devices. *Eur. J. Inorg. Chem.* **2013**, *2013* (9), 1481–1487.

(24) Quddious, A.; Yang, S.; Khan, M. M.; Tahir, F. A.; Shamim, A.; Salama, K. N.; Cheema, H. M. Disposable, Paper-Based, Inkjet-Printed Humidity and H_2S Gas Sensor for Passive Sensing Applications. *Sensors* **2016**, *16* (12), 2073.

(25) Wasalathanthri, N. D. Green Catalytic Applications of Functional Nanomaterials and Design, Synthesis, and Structure - Property Relationships of Sodium Tungsten Bronze Thin Films, Doctoral Dissertation, University of Connecticut, 2017.

(26) Vaezi, M.; Seitz, H.; Yang, S. A Review on 3D Micro-Additive Manufacturing Technologies. *Int. J. Adv. Manuf. Technol.* **2013,** *67* (5–8), 1721–1754.

(27) Bishop, G. W.; Satterwhite-Warden, J. E.; Kadimisetty, K.; Rusling, J. F. 3D-Printed Bioanalytical Devices. *Nanotechnology* **2016**, *27* (28), 284002.

(28) Busato, S.; Belloli, A.; Ermanni, P. Inkjet Printing of Palladium Catalyst Patterns on Polyimide Film for Electroless Copper Plating. *Sensors Actuators B Chem.* **2007**, *123* (2), 840–846.

(29) Taylor, A. D.; Kim, E. Y.; Humes, V. P.; Kizuka, J.; Thompson, L. T. Inkjet Printing of Carbon Supported Platinum 3-D Catalyst Layers for Use in Fuel Cells. *J. Power Sources* **2007**, *171* (1), 101–106.

(30) Liu, X.; Shen, Y.; Yang, R.; Zou, S.; Ji, X.; Shi, L.; Zhang, Y.; Liu, D.; Xiao, L.; Zheng, X.; et al. Inkjet Printing Assisted Synthesis of Multicomponent Mesoporous Metal Oxides for Ultrafast Catalyst Exploration. *Nano Lett.* **2012**, *12* (11), 5733–5739.

(31) Lee, S.; Boeltken, T.; Mogalicherla, A. K.; Gerhards, U.; Pfeifer, P.; Dittmeyer, R. Inkjet Printing of Porous Nanoparticle-Based Catalyst Layers in Microchannel Reactors. *Appl. Catal. A Gen.* **2013**, *467*, 69–75.

(32) Symes, M. D.; Kitson, P. J.; Yan, J.; Richmond, C. J.; Cooper, G. J. T.; Bowman, R. W.; Vilbrandt, T.; Cronin, L. Integrated 3D-Printed Reactionware for Chemical Synthesis and Analysis. *Nat. Chem.* **2012**, *4* (5), 349–354.

(33) Kitson, P. J.; Rosnes, M. H.; Sans, V.; Dragone, V.; Cronin, L. Configurable 3D-Printed Millifluidic and Microfluidic 'Lab on a Chip' Reactionware Devices. *Lab Chip* **2012**, *12* (18), 3267–3271.

(34) Kitson, P. J.; Symes, M. D.; Dragone, V.; Cronin, L. Combining 3D Printing and Liquid Handling to Produce User-Friendly Reactionware for Chemical Synthesis and Purification. *Chem. Sci.* **2013**, *4* (8), 3099–3103.

(35) Tubío, C. R.; Azuaje, J.; Escalante, L.; Coelho, A.; Guitián, F.; Sotelo, E.; Gil, A. 3D Printing of a Heterogeneous Copper-Based Catalyst. *J. Catal.* **2016**, *334*, 110–115.